

Stimuli-Responsive Memristive Materials for Artificial Synapses and Neuromorphic Computing

Hongyu Bian, Yi Yiing Goh, Yuxia Liu, Haifeng Ling, Linghai Xie,* and Xiaogang Liu*

Neuromorphic computing holds promise for building next-generation intelligent systems in a more energy-efficient way than the conventional von Neumann computing architecture. Memristive hardware, which mimics biological neurons and synapses, offers high-speed operation and low power consumption, enabling energy- and area-efficient, brain-inspired computing. Here, recent advances in memristive materials and strategies that emulate synaptic functions for neuromorphic computing are highlighted. The working principles and characteristics of biological neurons and synapses, which can be mimicked by memristive devices, are presented. Besides device structures and operation with different external stimuli such as electric, magnetic, and optical fields, how memristive materials with a rich variety of underlying physical mechanisms can allow fast, reliable, and low-power neuromorphic applications is also discussed. Finally, device requirements are examined and a perspective on challenges in developing memristive materials for device engineering and computing science is given.

1. Introduction

Modern computing systems are organized based on von Neumann architectures by which data are constantly transferred between physically separated processing and memory blocks. The capacity for information processing and storage relies

on advances in the associated electronic devices, particularly silicon-based complementary metal–oxide–semiconductor (CMOS) transistors. With an exponential increase in unstructured data connecting to the internet, computing speed and energy efficiency become challenging due to the speed-mismatch-induced memory wall between memory units and processors, also known as the von Neumann bottleneck. Moreover, with the impending end of Moore's law^[1] and the breakdown in Dennard scaling,^[2] current transistor technology faces difficulties maintaining cell scaling below the 5 nm node. To address these issues, researchers have started exploring novel circuit-building blocks and computing paradigms, similar to the human brain structure and function, for the merits of processing-in-memory capacity and ultralow-power consumption

(Figure 1). The human brain consists of about 10^{11} neurons interconnected by 10^{15} synapses. When a neuron is excited, an action potential is produced and propagated. Action potential-encoded information is then transmitted through a network of synapses almost simultaneously to other neurons. Inspired by the human brain, neuromorphic computing aims to perform an energy-efficient synaptic operation by emulating neurons and synapses at three different levels: i) device level (artificial synapses and neurons); ii) circuitry level (device networks); iii) algorithm level (learning rules and training methods). Currently, artificial synaptic devices are primarily built on charge-based CMOS chips, such as dynamic random-access memory (DRAM) and static random-access memory (SRAM), which require multiple transistors to perform one synaptic function. Various prototypes of neuromorphic chips have been fabricated, including SpiNNaker, TrueNorth, Loihi, and BrainScaleS, among others.^[3] For SpiNNaker, 1 million cores (up to 1000 neurons per core) based on 130 nm CMOS were used.^[4] Meanwhile, the TrueNorth CMOS chip was made to integrate 1 million neurons and 256 million SRAM synapses.^[5] Loihi is a multicore chip built on a 14 nm fin field-effect transistor, which has 130 000 neurons and 130 million synapses with 1–9 bits.^[6] Other chips that display excellent performance include NeuroGrid, Tianjic, DYNAP-SE, and ODIN, as well as Braindrop that requires only 0.38 pJ per synaptic update.^[7–12] Furthermore, these CMOS components are volatile and suffer from major physical limitations, such as moderate scalability and inefficient synaptic operation.


Unlike conventional CMOS transistors, memristors represent an emerging class of bioinspired devices that directly

Dr. H. Bian, Y. Y. Goh, Dr. Y. Liu, Prof. X. Liu
 Department of Chemistry
 National University of Singapore
 Singapore 117543, Singapore
 E-mail: chmlx@nus.edu.sg

Y. Y. Goh
 NUS Graduate School for Integrative Sciences and Engineering
 National University of Singapore
 Singapore 119077, Singapore

Dr Y. Liu, Prof. X. Liu
 Center for Functional Materials
 National University of Singapore Suzhou Research Institute
 Suzhou 215123, China

Prof. H. Ling, Prof. L. Xie
 Key Laboratory for Organic Electronics and Information Displays
 and Institute of Advanced Materials (IAM)
 Jiangsu National Synergetic Innovation Center for Advanced Materials (SICAM)
 Nanjing University of Posts and Telecommunications
 Nanjing 210023, China
 E-mail: iamhxie@njupt.edu.cn

 The ORCID identification number(s) for the author(s) of this article can be found under <https://doi.org/10.1002/adma.202006469>.

DOI: 10.1002/adma.202006469

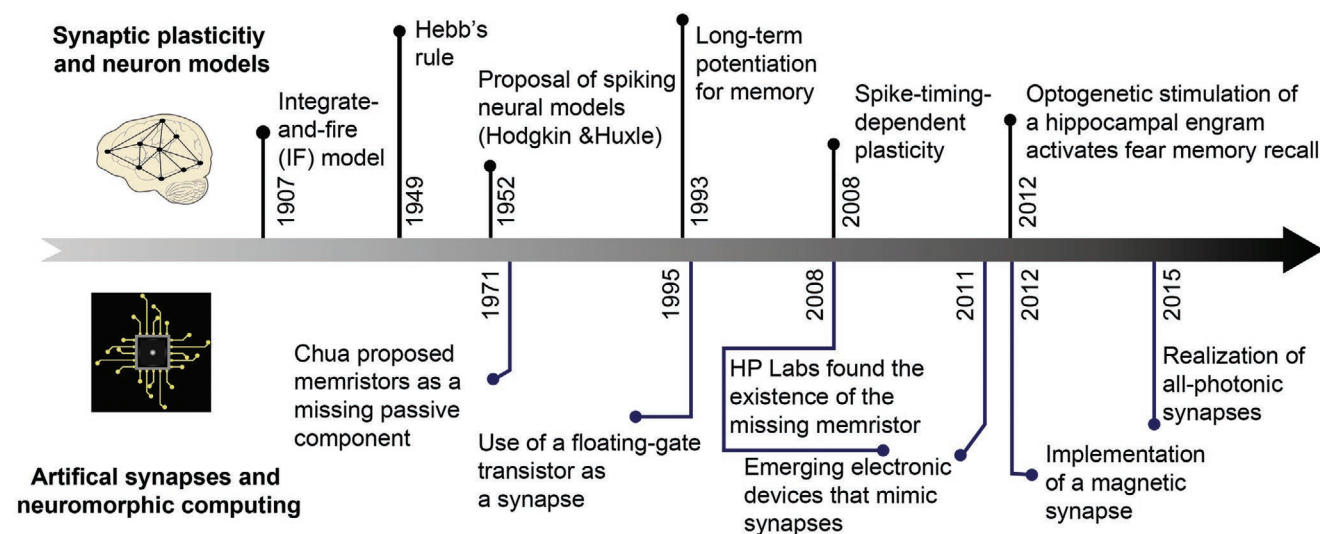


Figure 1. Milestones of research on synaptic plasticity and neuron models, as well as artificial synapses and neuromorphic computing.

simulate synaptic and neural functions.^[13–16] Memristors can be analog and nonvolatile, integrating memory and logic units in one nanoscale device. For memristive materials, tunable and continuous resistance states or optical properties can be induced by an external stimulus (e.g., an electric, magnetic or optical field), and information can be stored as different states. As such, memristive crossbar arrays use conductance to represent weights in physical artificial neural networks (ANNs), enabling the simulation of synaptic transmission and brain dynamics.

In recent years, a number of reviews have provided a comprehensive summary of various synaptic and neuronal phenomena mimicked by memristive devices.^[16,17] The operation of reported resistive-switching materials (RSMs) is mostly achieved through electrical or magnetic manipulation.^[18,19] On the other hand, optically induced phase-change materials (PCMs) have been developed for photonic synapse simulation and network processing,^[20–26] while many electrical devices can also work more efficiently through photonic stimulus.^[27,28] However, it is worth noting that to the best of our knowledge, all these memristive devices have not been categorized in a review on the basis of the applied stimulus. Several reviews have focused on two-terminal memristive structures,^[14,29] but memristive devices can also be classified into two-, three-, and multiple-terminal systems, depending on the device configuration.

This review aims at bridging the existing knowledge gap by highlighting material-based solutions in the context of different stimuli (electronic, magnetic, and photonic) and terminal systems. We firstly provide an overview of the action potential process, followed by a summary of brain behaviors. Subsequently, we discuss the main mechanisms underlying the synaptic transmission in various materials, explaining how an input induces a switching for each of these mechanisms. Next, we examine some characteristics of memristive materials, emphasizing the functions and performance of the devices, such as switching rate, switching ratio, power consumption, and endurance. Finally, we discuss the remaining challenges and conclude by providing a perspective on future directions for advancing materials, mechanisms, and algorithm design. In

particular, we describe emerging frontiers in photonics-based memristors, in which much of the potential of memristors remains to be harnessed.

2. Synaptic Functions

Functional junctions between neurons are called synapses, which allow individual neurons to communicate via electrical or chemical signals among themselves or to non-neuronal cells.^[30] Chemical synapses are predominant synapses in the nervous systems. Impulses pass via diffusion of neurotransmitters that allow neurons to form circuits within the central nervous system and with target effector cells (**Figure 2a**). At a chemical synapse, a presynaptic neuron releases neurotransmitter into a synaptic cleft connecting to a postsynaptic neuron that receives the impulse. Chemical synapses can be classified as excitatory or inhibitory synapses, depending on the type of neurotransmitters released. In neuroscience, synaptic plasticity is defined as the synapses' ability to strengthen or weaken over time in response to increased or decreased activity. Since memories are generally regarded to be stored by the exceedingly complex neuronal networks, synaptic plasticity plays a vital role in controlling memory through synaptic connection.

2.1. Homosynaptic Plasticity

Homosynaptic plasticity (dubbed as Hebbian plasticity) is a type of localized synaptic plasticity that typically activates targeted postsynaptic neurons upon specific presynaptic neuronal stimulation.^[31] It characterizes the associative nature of synaptic changes, mediating the formation and refinement of neuronal connectivity, as well as establishing a physical foundation for neuronal computations. Homosynaptic plasticity encompasses several forms, including short-term plasticity (STP), long-term plasticity (LTP) (long-term potentiation/depression), and spike-timing dependent plasticity (STDP).

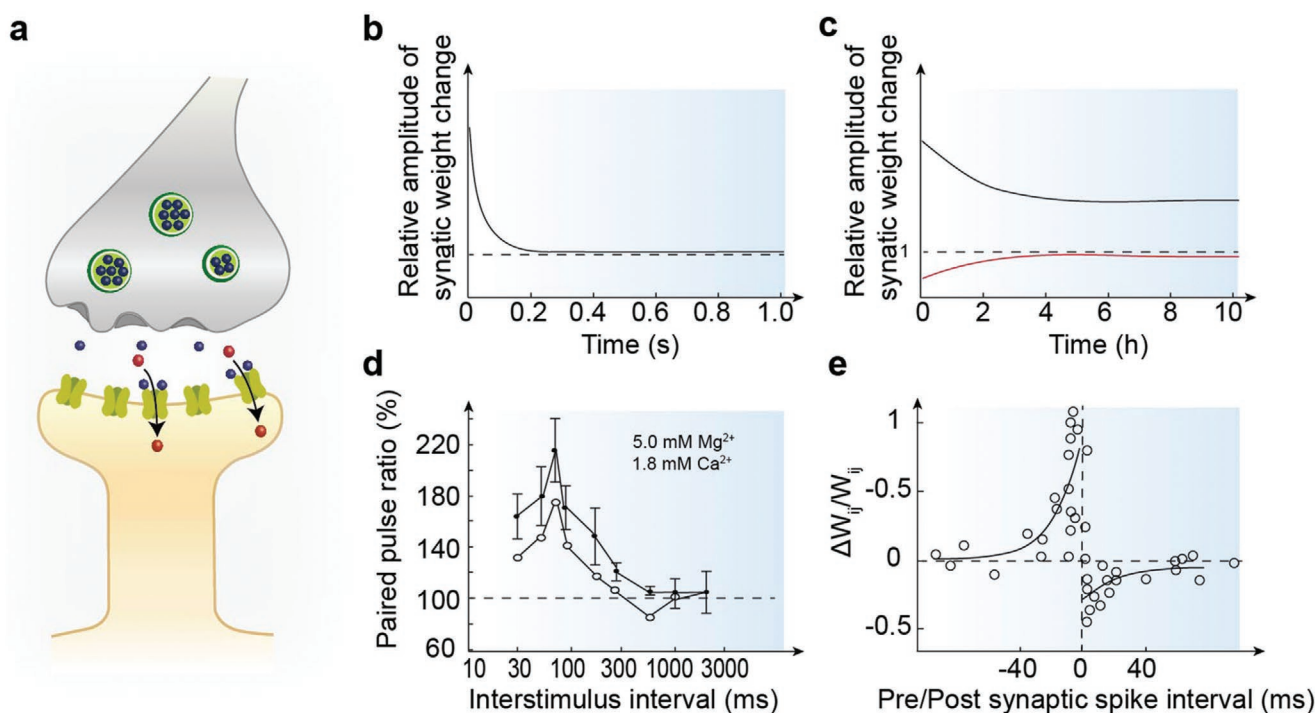


Figure 2. Chemical synapses and various forms of plasticity. a) A chemical synapse controlling the release of neurotransmitter molecules from synaptic vesicles into the synaptic cleft. b–e) Different types of synaptic plasticity. b) STP, indicated by an ephemeral change of synaptic weight. c) LTP, including long-term potentiation (LTPot) with increased synaptic weight (black line) and LTD with decreased synaptic weight (red line). d) PPF induced by short interstimulus intervals. e) STDP indicated by the spike-timing window of STDP to induce potentiation or depression. d) Reproduced with permission.^[37] Copyright 1996, The Physiological Society. e) Reproduced with permission.^[38] Copyright 1998, Society for Neuroscience.

2.1.1. STP and LTP

STP reflects the dynamic activity of a synapse, typically on a timescale of tens of milliseconds to a few minutes (Figure 2b). STP participates in short-term adaptations to transient changes in behaviors or short-lasting forms of memory.^[32] In contrast, LTP is characterized by long-lasting modifications of synaptic strength (Figure 2c).^[33] Long-term depression (LTD) and long-term potentiation (LTPot) are two forms of LTP, representing either persistent decrease or increase in synaptic strength.^[32] *N*-methyl-D-aspartate (NMDA)-dependent LTD and LTPot generally require binding of glutamate, glycine, or D-serine for NMDA receptor activation.^[30] Conventionally, LTPot and LTD can be induced by prolonged high- or low-frequency stimulation, respectively, by which synaptic efficacy can be modified in a bidirectional manner.^[34,35] The short- and long-term threshold characteristics of synaptic adoption, modulation, and modifications depend mainly on the functional dynamics of the synapse.^[33]

2.1.2. Paired-Pulse Facilitation (PPF) and Paired-Pulse Depression (PPD)

In STP categories, when a short time interval separates two stimuli, the second stimulus can either boost or suppress the response, leading to PPF or PPD, respectively.^[36] Consequently, upon arrival of the second stimulus, an increased or decreased

residue in the remaining presynaptic Ca^{2+} concentration of the first stimulus may increase or decrease the number of neurotransmitter molecules in the synaptic cleft.^[37,38] During PPF, the second spike can significantly increase the synaptic current, especially if it immediately follows the first spike (Figure 2d). Conversely, the second spike will decrease the corresponding current when a paired-pulse stimulation is applied for PPD. Though producing different outcomes for synaptic current, both PPF and PPD are affected by the interval between the two spikes. The increasing synaptic current ratio is inversely proportional to the time interval. The PPF and PPD are critical in decoding temporal information of visual and auditory signals because they reflect the most recent spike occurrence and thus transform temporal information into spatial data. In visual systems, STP (PPF and PPD) can endow different retinogeniculate synapses with dynamically controlled properties via a presynaptic train of action potentials, enriching the responsiveness at the temporal scale.^[39] Additionally, PPF generally occurs in synapses with a low probability of neurotransmitter release,^[40] while synapses with a high release probability show PPD.^[41,42] In doing so, the systems achieve some degrees of compensability and adaptability. In short-term memory (STM), device states are affected by previous programming pulses within a time range. The device state effect is most intense at the onset of the pulse, but becomes weaker over time due to device decay to its initial state.^[43] The final effect depends on the behavior of calcium accumulation or release in the device under external stimulation. Neurons with activated or suppressed synapses

enhance their ability to distinguish a sequence of events in reverse order.^[44] More works of temporal information of visual and auditory signals were reported elsewhere.^[45–47]

2.1.3. STDP

In addition to frequency, the order and temporal interval of stimuli between presynaptic and postsynaptic spikes can determine the features of LTPot and LTD. This form of activity-dependent LTPot/LTD is known as STDP.^[48] STDP describes variations in synaptic weight, which is regulated not only by the interval between presynaptic and postsynaptic spikes but also by the interspike intervals of individual neuron (Figure 2e). A typical example is Hebbian STDP, which exhibits Hebbian associated plasticity in a time-dependent manner. Specifically, LTPot is induced when presynaptic and postsynaptic spikes are separated by a short time interval (≈ 10 ms), whereas a reverse spiking order results in LTD. However, the synaptic weight remains unchanged when the time interval between the two spikes is too long.^[49] Besides Hebbian STDP, there are three other types of STDP: anti-Hebbian STDP, symmetrical STDP, and visual STDP learning rule.^[37,50]

2.1.4. Learning-Experience-Dependent Plasticity

Emerging evidence indicates the existence of experience-dependent plasticity, which is the creation, modulation, and organization of neuron connections, mainly based on past experiences. For instance, in the course of such plasticity, a dendritic specialized for axodendritic synapses could be associated with either synapse formation (sprouting) or synapse elimination (retraction). Learning experience-dependent plasticity that acts on impulses based on past-learned events can modify synaptic weights as well.^[51] Moreover, Ebbinghaus described the learning–forgetting law, in which the stimulus strength is reduced with an increasing number of stimuli due to memory repository. Such synaptic plasticity enables neuronal networks to self-adapt.^[52]

2.2. Heterosynaptic Plasticity

Unlike the input-specific homosynaptic plasticity occurring at active synapses, the heterosynaptic plasticity can be induced as a supplementary form of plasticity on inactive synapses.^[53] Compared with the function of homosynaptic plasticity associated with learning, the non-Hebbian-type heterosynaptic plasticity mainly plays a stabilizing role in preventing synaptic adoption and neuronal firing from getting out-of-balance induced by positive feedback in the Hebbian-type learning. This necessitates the adjustment of both associative and nonassociative learning by heterosynaptic plasticity. Typically, habituation and sensitization are two fundamentally different forms of nonassociative learning. Habituation refers to a decrease in the nonreinforced innate response after repeated or prolonged applications of a stimulus. Sensitization describes the ability of a strong stimulus to produce an overall increase in its response.

While homosynaptic plasticity is usually simulated using two-terminal devices, realization of heterosynaptic plasticity require three-terminal or multi-terminal memristive systems.

2.3. Biological Neuron Models

Generally, a neuron is composed of three distinctive parts: soma, dendrites, and axon. Neurons can be unipolar, bipolar, or multipolar, depending on their morphology (Figure 3a).^[16] The cell body, or soma, is the spherical part of the neuron that contains the nucleus. Dendrites are branch-like extensions with tiny protrusions of protoplasm from the soma that retrieve signals from elsewhere. Axons or nerve fibers extend from the soma and carry impulses from the soma to other neurons or muscles and glandular cells. A neuron typically comprises many dendrites and just one axon. One can distinguish axons from dendrites based on their shape and size or the presence of Nissl bodies, the equivalent of rough endoplasmic reticulum, present only in somas and dendrites. There are three main forms of synapses: axonal–dendritic, axonal–axonal, and axonal–somatic. Two parts from two different nerves form one synapse. The axon of one neuron is the presynaptic structure that carries input impulses. An axon, soma, or dendrites from another neuron can serve as the postsynaptic structure to receive the impulses. The synaptic cleft between the two segments is the gap, across which neurotransmitters diffuse, carrying either excitatory or inhibitory synaptic inputs. Upon an excitatory input, most neurons are depolarized, triggering an action potential. In contrast, upon an inhibitory input, neurons hyperpolarize without evoking any action potentials. A neuron with numerous synapses can receive both excitatory and inhibitory inputs simultaneously. In practice, three models are used to describe neural functions: the integrate-and-fire (IF) model, the leaky-integrate-and-fire (LIF) model, and the Hodgkin–Huxley (HH) model.^[54,55]

In 1907, Lapicque proposed the IF model, based on an electric circuit with parallel capacitors and resistors to represent membrane capacitance and leakage resistance.^[56] When stimulation was applied to presynaptic neurons, postsynaptic excitatory or inhibitory currents were elicited due to local changes in the membrane potential. The current also increased or decreased with the strength of dendrite-connected synapses. Excitatory current can be temporally and spatially integrated, inducing a graded potential. An action potential forms when the graded potential reaches a specific threshold (Figure 3b).

The time-dependent current is derived from

$$I(t) = C_m \frac{dV_m(t)}{dt} \quad (1)$$

which is obtained by taking the derivative of time from the law of capacitance, where C_m represents the membrane capacitance, and V_m represents the membrane potential. Upon applying an input current, a corresponding membrane voltage will increase over time till a constant threshold V_{th} is reached, wherein a delta function spike occurs, and the voltage returns to its resting potential, thereafter the model continues running. Therefore, there is an unlimited linear increase in the model's

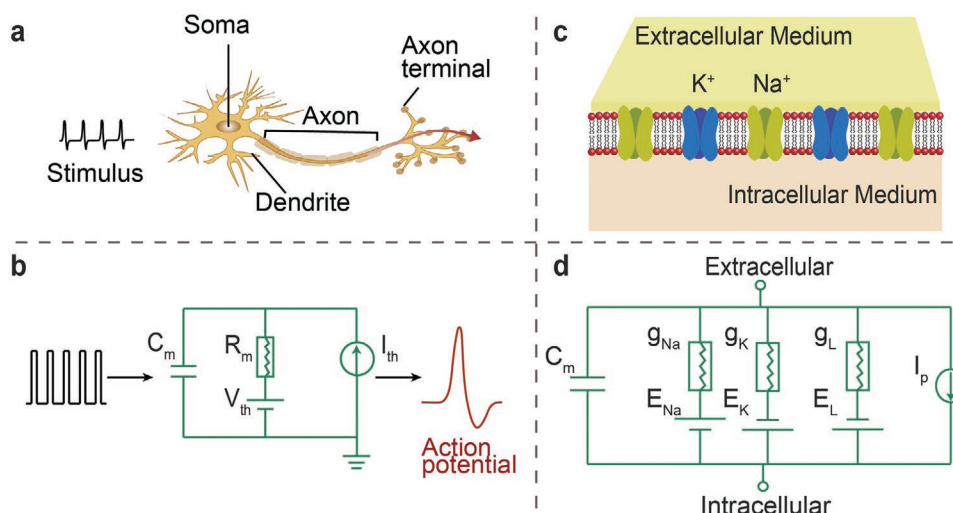


Figure 3. Bioinspired neuron models. a) Schematic of an action potential fired by a biological neuron. b) Integrate-and-fire neuron model. C_m , membrane capacitance; R_m , membrane resistance; V_{th} , membrane potential; I_{th} , injected current. c) Schematic of a neuronal membrane. d) Hodgkin-Huxley neuron model, g_{Na} : conductance of Na^+ channel; g_K : conductance of K^+ channel; g_L : leak conductance; and the associated equilibrium potential for each conductance is represented by a labeled battery. C_m and I_p represent the membrane capacitance and injection current, respectively. d) Adapted with permission.^[58] Copyright 1952, The Physiological Society.

firing frequency with an increase in input current. R_m is considered as the membrane resistance in this model because it cannot be the perfect insulator that was hypothesized previously

$$I_{th} = \frac{V_{th}}{R_m} \quad (2)$$

The input current (I_{th}) thus needs to exceed a certain threshold before the cell generates action potential. Otherwise, any change in potential would leak out. The observed firing frequency, therefore, converges at large input currents, different from the earlier leak-free model with the refractory period.^[57] However, this characteristic is not consistent with the actual behavior of neurons. In fact, in biological neuronal models, a localized graded potential shows short-term dynamics, resulting in a subthreshold membrane boost that leaks out rapidly. Therefore, the LIF neuron model was proposed by adding a rule that regulates spikes once the membrane potential surpasses a threshold, which mimics ion diffusion occurring through the membrane when the cell is in disequilibrium. According to the LIF neuron model, any subthreshold membrane boost leaks with time, allowing time-dependent memory to be implemented in neurons.

One limitation of IF and LIF models is their inability to implement time-dependent memory. The HH model simulates the dynamic relationship between the ionic current flow across the cell membrane of the neuron and the cell membrane potential.^[58] A neuronal membrane acts as a barrier between the neuronal cytoplasm and the external environment (Figure 3c), across which a complex and dynamic ion exchange process occurs. Simulation of changes in spike-induced ion channel conduction using the HH neuron model is comparable to a circuit (Figure 3d).^[59] Similar to the IF model, membrane depolarization is caused by dendritic inputs. In general, a response is generated when a stimulus changes the cell

membrane polarity from -70 to above -55 mV, causing voltage-gated Na^+ channels to open and allowing Na^+ ions to enter the cell. Once the Na^+ channels open, the neuron depolarizes to a membrane potential of about $+40$ mV. At this voltage, Na^+ channels close, and voltage-gated K^+ channels open, allowing K^+ ions to rapidly diffuse out of the cell. This will return the inside membrane potential to be negative, closing voltage-gated K^+ channels and leading to hyperpolarization. At this stage, the membrane polarity briefly goes beyond -70 mV, which is called the refractory period. Finally, the Na^+ and K^+ ATP pumps restore the resting potential balance by pumping two K^+ into and three Na^+ out of the cell. The newly generated action potential can move down the axons and propagate through synapses to other neurons. During hyperpolarization, or the repolarization phase, which is the pre-activation phase of neurons, the membrane potential stabilizes at its resting potential (-70 mV). One factor that hinders the application of the HH model in ANNs, in contrast to other neuron models such as IF and LIF, is its complexity as a nonlinear system, along with the fact that it is analytically unsolvable. However, new prospects for artificial synapses and neurons may emerge through advances in memristive devices.^[60] Therefore, the following sections introduce the main concepts and the switching mechanisms behind memristive devices.

3. Operation Mechanism of Memristive Materials

Memristive devices are the critical functional components of neuromorphic computing systems. Memristive materials can be classified according to their mechanisms (electronics-, ionics-, or photonics-based), and device structures (two-terminal memristor, three-, or multi-terminal transistor), as well as the type of the externally applied field (electric, magnetic, or optical). These device types are discussed in subsequent sections.

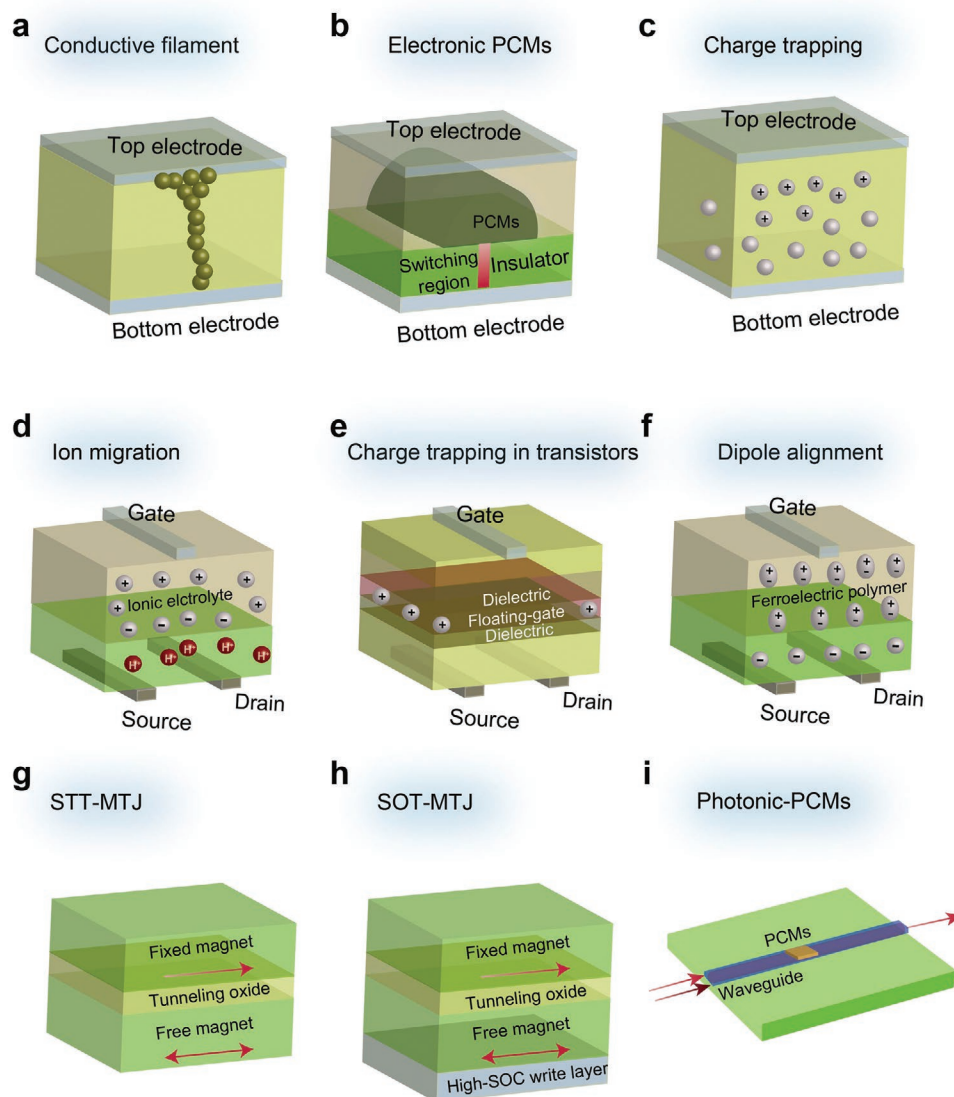


Figure 4. Schematics of various mechanisms underlying memristive devices: a–i) Conductive filament, electronic PCMs, charge trapping, ion migration, charge trapping in floating-gate transistors, dipole alignment, STT–MTJ, SOT–MTJ, and PCMs as optical memory systems.

3.1. Electric-Field-Operated Memristive Devices

In 1971, Chua predicted that there would be a fourth two-terminal circuit element called memristor.^[61] The resistance states of the memristor depends on the history of the current or voltage experienced. In 2008, HP labs reported the discovery of memristors in TiO_x -based two-terminal resistive switching devices, which experimentally established a link between these electronic elements and biosynapses and neurons.^[62] Researchers developed different kinds of materials to create artificial synapses and neurons. They fall into two categories, namely, memristors and neuromorphic transistors. For memristors, conductive filaments, phase changes and charge trapping are the three main operation mechanisms (Figure 4a–c), whereas electrolyte-gated transistors, floating-gated field-effect transistors and ferroelectric field-effect transistors are three typical types of neuromorphic transistors.

The working mechanisms of resistive switching devices are shown in Figure 4d–f.

3.1.1. Conductive Filament Mechanism

Redox reactions and ion migration induce switching when electric voltage is applied to a memristor. In transition-metal oxide-based RSMs, anions such as oxygen ions move from one electrode to the other when voltage is applied.^[63,64] Migration of anions usually leads to lower resistance when a suboxide phase is formed. Conductive channels are formed in the switching materials. Anion-based filamentary switching is known as the valence change mechanism (VCM). The device switches to a low-resistance state (LRS), depending on the growth of filaments. When a reverse electric field is applied, the conductive channels are ruptured, and the device reverts

to its high-resistance state (HRS). This phenomenon was first observed in an undoped SrTiO_3 crystal using conductive-tip atomic force microscopy.^[65] Conduction channels were also revealed in a $\text{Pt/TiO}_2/\text{Pt}$ structure with TEM.^[66] In addition, X-ray absorption spectroscopy and electron-energy-loss spectroscopy were used for studying the composition of nanofilaments in several oxide compounds.^[66–69] As in VCM cells, the formation or dissolution of conductive filaments results in a change in cation-based filamentary devices composed of active metals, such as Ag and Cu. As a result, an electrochemical metallization mechanism is responsible for this kind of memristor.

Moreover, conductive filaments can be formed via two growth modes based on their redox rate and ion mobility. Low redox rates inactivate the metal electrode, where high redox rates have the opposite effect. For example, oxides and nitrides show low redox rate and ion mobility, whereas sulfides, iodides, selenides, tellurides and ternary chalcogenides exhibit large redox rates and ion mobilities.^[70] Conductive channels of $\text{Ag/As}_2\text{S}_3/\text{Ag/Ag}$ device were first observed in 1975.^[71] Recently, an $\text{Au/SiO}_x/\text{Ag/Au}$ device was used as a prototype to study the dynamic switching processes.^[72] An Ag bridge formed between the two electrodes when the voltage was applied via in situ TEM, due to a bipolar-electrode effect. The Ag cluster relaxed after removing the bias voltage owing to the minimized interfacial energy between the Ag nanoparticles. For the Cu dynamic filament, reactive molecular dynamics have been used as a computational model.^[73] In addition, valence-change redox devices such as TaO_x can show cation transport.^[74]

3.1.2. Phase-Change Mechanism

The process of phase change in chalcogenide glass materials forms the basis of phase-change RSMs. These materials exhibit low or high electrical resistance, depending upon the crystal phase of the materials.^[75–77] Usually, Joule heating above the melting point and passive thermal dissipation convert the crystalline phase to an amorphous phase (Figure 4b). Electrical resistance is defined as 0 or 1 for data storing because of a large resistance gap between amorphous and crystalline states.^[78] Structure disorder, carrier concentration, and bonding mechanisms differ between the two states.^[79–85] Switching speed and retention time are two main characteristics of nonvolatile memory. In PCMs, it takes 50 to 1000 ns to change the material from amorphous to crystalline.^[86,87] Materials that crystallize more rapidly are needed. Growth-dominated and nucleation-dominated materials are two such types. For growth-dominated materials, a single crystalline phase is usually created between amorphous and crystallized phases, such as Ag- and In-doped SbTe ($\text{Ag}_4\text{In}_3\text{Sb}_{67}\text{Te}_{26}$, AIST). On the other hand, nucleation-dominated PCMs are recrystallized through the stochastic formation of critical nuclei. Growth and nucleation are fast in nucleation-dominated, phase-change RSMs, (e.g., $\text{Ge}_2\text{Sb}_2\text{Te}_5$), which grow to a polycrystalline phase along different grain orientations.^[86] Temperature is the main factor controlling the speed of crystal growth due to the temperature dependence of the driving force and interfacial energy.^[87]

3.1.3. Charge Trapping Mechanism in Memristors

Defect-induced charge trapping and detrapping at the electrode/RSMs interfaces or in the bulk of the RSMs can induce resistive switching in defect-rich oxides and hybrid systems.^[88–91] The switching phenomenon is related to space charge-limited current (SCLC) conduction, similar to that observed in $\text{Al/SiO}_2/\text{Au}$ diodes by Simmons and Verderber.^[92] For in defect-rich oxides, holes or electrons from electrodes can be confined to interfacial traps. A charge build-up due to carrier accumulation modulates the Schottky barrier in defect-rich oxides.^[93] The dominant analog switching mechanism is deemed to be interfacial trapping, characterized by a clear hysteresis.^[94] One representative example is the $\text{Au/WO}_3/\text{FTO}$ device, where the existence of W-5d states near the Fermi level can be considered as electron traps at the electrode/ WO_3 interface.^[94] Upon applying an external negative/positive electric field, the electrons could be trapped/detrapped at the surface states, leading to the increase/decrease in the Schottky barrier potential and subsequently the HRS-to-IRS switching. By comparison, abrupt switching is usually obtained in the hybrid RSMs comprising a wide-bandgap polymer matrix and nanostructured materials.^[95,96] Owing to the difference in orbital energy level, metal nanoparticles (e.g., Au NPs,^[97] quantum dots,^[98] black phosphorus,^[99] and graphene^[100]) and small semiconducting molecules (e.g., C_{60} ^[101] and 6-phenyl-C61 butyric acid methyl ester (PCBM)^[102]) can act as trapping centers in the blended system. The application of an electric field induces a sufficient amount of electrons/holes to be filled at the trapping sites. With increasing voltage, the injected carriers rapidly increase, nearly filling the traps. Fowler–Nordheim (FN) tunneling may occur between adjacent trapping centers, switching the device from the initial HRS to LRS.^[103] An opposite voltage bias extracts the trapped carriers, switching the device back to the HRS. In the HRS, the charge transport behavior follows classical trap-controlled SCLC, which comprises three regions: an initially Ohmic region ($I \propto V$), a Child's law region ($I \propto V^2$), and the steeply rising region of current ($I \propto V^n$, $n > 2$).^[104] Specifically, nanoparticle-incorporated hybrid memristors usually exhibit bipolar switching,^[105] tristable switching,^[100] or negative differential resistance.^[106,107]

3.1.4. Mechanisms in Neuromorphic Transistors

Hardware implementation of synaptic functionalities using transistors by Mead and co-workers can be traced back to the 1990s.^[108] Several CMOS transistors are required to build one synapse because of their volatile working principle. However, there are significant challenges associated with design complexity and low energy efficiency in large-scale integration. In contrast, neuromorphic transistor refers to a three-terminal, thin-film transistor that exhibits a certain degree of non-volatility. It combines the architecture superiority of control terminal (gate) and transduction terminals (source–drain), and the resistance tunability of memristive devices.^[109] As a result, it is possible to precisely record analog weight updates, such as the gradual resistive changes, in a tightly coupled fashion. Typical neuromorphic transistors include electrolyte-gated transistors (EGTs), floating-gated field-effect transistors (FETs), and

ferroelectric field-effect transistors (FeFETs). Their mechanisms are introduced below.

Ion Migration in Electrolyte-Gated Transistors: EGTs employ electrolytes as the gate dielectric and utilize coupled ionic–electronic features to modulate the channel conductivity of the device.^[110] Memristive devices usually utilize two main types of EGTs, which depends on the electrolyte ions permeability of the semiconductor channel.^[111] An electrolyte-gated field-effect transistor is impermeable to ions, and the gate voltage is formed at the electric double layer between the channel and the electrolyte, modulating the channel current (Figure 4d).^[112] An electrochemical transistor (ECT) is ion-permeable and modulated by electrochemical doping/dedoping processes after injecting ionic species into the redox-active channel material. Compared to ECTs, EGTs hold greater potential for neuromorphic implementation, with advantages of ultralow-voltage operation,^[113] global regulation,^[114] lateral coupling ability, and multiple-terminal configuration.^[115] The kHz operation speed of EGTs is limited by ion drift and diffusion.

Charge Trapping in Floating-Gated Field-Effect Transistors: Floating-gated FETs incorporate chargeable dielectrics as charge storage mediums, including discrete metal nanoparticles,^[116] 2D materials,^[117] inorganic semiconducting nanostructured materials,^[118] continuous polymer electrets, and small molecules.^[119–121] Charge trapping occurs at floating-gates or semiconductor/dielectric interface (Figure 4e). Upon applying a gate voltage to the gate electrode, electrons/holes are injected into the floating-gates via direct tunneling or FN tunneling. These trapped charges modulate the carrier distribution and the channel conductance. A blocking, tunneling dielectric layer enables nonvolatile storage of the trapped charges. Applying a gate voltage with reverse polarity, tunneling, or recombination with the injected opposite charges releases the trapped charges back to the channel. However, the tunneling process usually requires a large voltage (>10 V) and slow programming (>1 ms), limiting the programming efficiency.

Dipole Alignment in Ferroelectric Field-Effect Transistors: FeFETs can be used to make oriented-dipole memory by spontaneous polarization switching of ferroelectric materials upon electrical input (Figure 4f).^[122–131] The carrier concentration of FeFETs could be precisely controlled by the gate voltage, enabling multilevel FeFET channel conductance for neuromorphic computing.^[132] In contrast to floating-gated FETs, FeFETs display faster operation speed (ns range), lower operation voltage (<6 V), higher endurance, and less variance in the weight update curve.^[133] However, FeFETs require thick ferroelectric films (200–500 nm) to achieve long retention time and large memory windows.^[134]

3.1.5. Theoretical Modeling of Memristors

Mathematical modeling can improve the understanding of the memristor's function, while providing design principles for future memristive materials. By defining the relationship between magnetic flux and the amount of charge based on Chua's model,^[61] Strukov et al. reported the first memristor using a Pt/TiO_{2-x}/Pt device and modeled the nonlinear ion drift of oxygen vacancies.^[62] Despite the achievement, fundamental

electrodynamics limitations remain. HP Labs then proposed to include the nonlinear dependency between the voltage and the internal state derivative into the nonlinear ion drift model.^[135] Other models have been reported to improve accuracy at work, such as the exponential model,^[136] the Stanford model,^[137,138] and the filament dissolution model.^[139,140] Most of these models were based on oxides (e.g., HfO_x, TiO_x, TaO_x) with variable parameters, such as the distance between conductive filaments, the temperature, the ion concentration, the diffusivity, and the activation energy.^[137–140] Theoretical models such as synaptic models and diffusive models for synaptic behavior evaluation have also been established in recent years.^[72,141] The diffusive model suggests that materials (e.g., MgO_x:Ag, SiO_xNy:Ag, and HfO_x:Ag) can have a substantial relaxation time because diffusion of metal ions eventually forms conduction channels.^[142]

3.2. Magnetic-Field-Operated Memristive Devices

Besides electrical memristors, certain magnetic devices have demonstrated the ability to vary their resistance with a change in the magnetic field. Instead of electron or ion transport, the resistance of such spintronic memristors depends on the change in magnetoresistance state of the device. Wang et al. reported their theoretical investigations of magnetic tunnel junctions (MTJ) and other magnetic memory designs, demonstrating memristive behavior using probing frequencies higher than the magnetization dynamic time scale.^[143] Their observations, coupled with later experimental evidence of spintronic memristors, spurred further research into mimicking brain processes using spintronic devices. These devices could be categorized in two regards: first, the mechanism in which the local magnetization is manipulated and second, the mechanism behind the switching-induced resistance change.

3.2.1. Spin Transfer Torque (STT) and Spin–Orbit Torque (SOT)

STT MTJ uses the STT effect to induce a magnetic state change in the free layer (Figure 4g). Upon electric current introduction through the MTJ, the magnetic orientation of the fixed layer spin-polarizes the electrons that pass through it. These electrons then pass through the free magnetic layer, transferring their spin angular momentum and changing the free layer's magnetic orientation to that of the fixed layer.^[144] Thereafter, when an electric current of the opposite direction is applied, the minority of electrons in the fixed layer, which has a spin polarization opposite to that in both layers, is reflected toward the free layer, switching its orientation antiparallel to the fixed layer. Another method of changing the magnetic state is by utilizing the SOT effect. Through addition of a high spin–orbit coupling material, for example, a heavy metal layer (Figure 4h), the magnetization state of the adjacent material can be manipulated.^[145] Unlike in STT, the current passes through the lower resistance heavy metal layer and not through the higher resistance ferromagnetic layers, thus utilizing less energy. Srinivasan et al. applied an MTJ–heavy metal heterostructure to a crossbar architecture of stochastic synapse and neuron.^[146] They achieved three orders of magnitude lower energy consumption

than the CMOS-based designs. Similarly, by adding a heavy metal layer adjacent to an MTJ domain wall magnet to form an MTJ-metal heterostructure, Sharad et al. managed to increase the domain wall velocity of their spin neuron under the same current density due to the Spin Hall effect (SHE).^[147] This also meant that the contemporary spin neuron design could achieve a fixed switching time using a lower current density. Therefore, they demonstrated superior energy efficiency and switching time using the spin neurons compared to the CMOS-based counterpart.

3.2.2. Magnetization Switching (MS) and Domain Wall Motion (DWM)

After STT- or SOT-induced switching occurs, the resulting resistance change in the MTJ is achieved via two main mechanisms, MS and DWM. MTJs that undergo magnetization switching exist in two states: a high-resistance, anti-parallel (AP) magnetization state, where the magnetization directions of the two layers are opposite, and a low-resistance parallel (P) state, in which the magnetization of the two layers is perfectly aligned. Therefore, based on the direction of the current applied, an MTJ exists as either the P or AP state, corresponding to high- or low-conductance, respectively. However, a fundamental weakness in MS devices is the lack of intermediate stable states. On the other hand, devices that utilize domain wall motion can have multiple stable intermediate states within one device.^[148] Wang et al. demonstrated memristive phenomena in both thin-film elements and spin valves with domain wall motions.^[143] However, such phenomena have also been demonstrated in MTJs, and many artificial synapses and neurons developed have been based on MTJ devices.^[149–152] These MTJs, like those used for magnetization switching, are also composed of two ferromagnetic layers, sandwiching an oxide tunneling layer. The main difference is the length of the free layer, which is longer than the other two layers, with the two ends of the layers having opposite spin polarizations. The domain wall is the space that separates the parts of the free layer with opposite spin polarization. As spin-polarized current flows through the device, the domain wall can move in either direction, depending on the direction of the current. The free layer with notches acts as points of local energy minimum also called pinning sites. When the external stimulus is removed, the domain wall stabilizes at one of these pinning sites, and the resistance depends on the domain wall position in the free layer.

3.3. Optical Field-Operated Memristive Devices

Optical field-operated memristive devices can be divided into two classes, optoelectronic and all-photonic synaptic devices. Optoelectronic memristive devices typically operate through photovoltaic effect-mediated Schottky barrier, photovoltaic effect-induced formation/annihilation of conductive filaments, photogating effect, and photoinduced chemical reaction, or conformation change.^[153] In contrast, photonic data storage significantly improves the performance of existing computing

architectures through latency reduction in electrical memories and the potential elimination of optoelectronic conversions.^[154,155] This is achieved via optical pulse-driven phase transitions in PCMs, which form the basis of all-photonic memory. It is integrated with waveguides on the chip, opening the possibility of photonic memory applications (Figure 4i). The transmission of light changes when excited by optical pulses of varying amplitudes, widths, frequencies, and time intervals, which simulates different types of memory. PCM-based Photonic memories contain both volatile and nonvolatile types. Before 2015, photonic memory had been volatile until Ríos et al. reported a multilevel nonvolatile photonic memory based on PCMs.^[20,156–160] They then obtained eight weight levels in a single device using optical near-field effects, featuring single-shot readout and low switching energies (13.4 pJ) at a speed of 1 GHz. These devices provide a new pathway to overcoming the von Neumann bottleneck, and they also offer a unique view of all-photonic memory and computing.

4. Memristive Materials

There are different classes of memristive materials that can simulate synaptic functions, with some representative materials listed in Table 1. The two big categories are inorganic and organic materials, each having their strengths and weaknesses, as described below.

4.1. Materials for Electronic Synapses and Neurons

4.1.1. Inorganic Materials

Inorganic material-based devices with high stability, short switching time, and high endurance are essential materials for memristive devices. In the inorganic material family, metal oxide semiconductors, 2D materials, graphene, and PCMs are the primary members (Figure 5).^[14,26] Metal oxide semiconductors are usually used as a medium layer between two metal electrodes to provide memristive properties. 2D material-based devices are highly promising for applications as memristors and memtransistors because of their fascinating physical and chemical properties. For example, owing to its unique electronic properties, graphene can provide many functions in memristive devices, such as the bottom electrode, the dielectric layer, and the ion-blocking layer. Moreover, PCMs provide new opportunities for power-efficient memristive devices because they can achieve nanosecond switching.

Metal Oxide Materials: Metal oxide semiconductors with highly recognized switching properties are core components of two-terminal memristors.^[161,162] Among these materials, HfO_x-based devices have shown superior switching speed and endurance, while retaining data reliably.^[163] Yu et al. fabricated HfO_x/AlO_x-based resistive switching memory, which attained sub-picojoule power consumption per operation in two-terminal, solid-state electronic synapses for the first time.^[164] By tuning the pulse amplitude, a linear variation in resistance was obtained within each time slot, enabling increased operational efficiency of the device. Other advantages of oxide materials

Table 1. Memristive materials for synaptic functions.

Type	Materials	Synaptic plasticity	Mechanism	Power consumption/ operation conditions	Terminal number	Retention time	Endurance [cycles]	Switching ratio	Ref.
Inorganic materials for electronic mem- ristive devices	HfO _x /AlO _x	STDP	Filamentary (VCM)	6 pJ per operation	2	–	10 ⁵	>10 ⁵	[164]
	InGaZnO	Learning experience- dependent	Oxygen ion migration	5 V	2	10 ⁵ s	–	–	[165]
	SiGe	Potential and Depression	Ag filament	≈4 μW	–	48 h (85 °C)	10 ⁶	10 ⁴	[270]
	SiO _x N _y :Ag	PPF, PPD, SRDP and STDP	Ag filament	0.75 V	2	1.2 s	10 ⁶	10 ⁶	[72]
	Ta ₂ O _{5-x} /TaO _y	LTP; STDP	oxygen vacancy migration	≈1 V	2	500 ns	>100	–	[173]
	MoO _x /MoS ₂ and WO _x /WS ₂	STP, LTP	Ion vacancy migration	10 nW	2	10 ⁴ s	>10 ⁴	10 ⁶	[182]
	MoS ₂	LTP, LTD, STDP, heteroplasticity	Ionic transport	0.143 mW μm ⁻²	Multiple	25 h	475	10 ²	[191]
	Au/MoS ₂	Heteroplasticity	Ion migration	≈0.5 μW	3	7 × 10 ³ s	>10 ³	10 ⁵	[196]
	Black phosphorus	LTP (LTPot/LTD), STDP	Charge trapping	20 V	Multiple	Hundreds of seconds	–	–	[210]
	Ge ₂ Sb ₂ Te ₅	IF	Phase change	5 pJ or 120 μW	2	–	10 ⁹	–	[217]
Organic materials for electronic mem- ristive devices	PEDOT:PSS	STP, LTP and PPF, PPD	Ion migration	10 pJ 10 ⁻³ μm ²	3	25 h	–	–	[123]
	PDPP	STP and LTP	Ion migration	10–100 fJ per operation	3	–	–	10 ⁸	[229]
	BTPA-F/EV(ClO ₄)	SRDP, STDP, PPF,PTP	Redox reaction	1 V	2	>300 s	10 ²	–	[231]
Materials for mag- netic memristive devices	FM/MgO/FM	LIF	STT induced MS/ DWM	18 fJ per operation	3	–	–	–	[243]
	FM/MgO/FM	PHP	SOT induced MS/ DWM	311 nW (neuron) 1.9–7.7 nW (synapse)	3	–	–	2.5	[232]
Materials for pho- tonic memristive devices	ZnO _{1-x} /AlO _y	STP, LTP, PPF	Charge trapping	0.072 mW cm ⁻² (UV light)	2	10 ³ s	10 ³	≈10 ⁴	[252]
	Gallium lanthanum oxysulphide	EPSP, IPSP, LTP, LTD, STDP	Phase change	58–150 mW (532 nm)	–	≈60 s	–	–	[253]
	ITO/Nb:SrTiO ₃	PPF	Charge trapping	10–30 mW cm ⁻² (blue light)	2	> 100 s	30	–	[254]
	In ₂ O ₃ /ZnO	STP, LTP, PPF	Charge trapping	≈0.2 nJ	2	>20 s	–	–	[255]

STP, short-term synaptic plasticity with broad timescales; LTP, long-term synaptic plasticity with broad timescales; LTPot, long-term potential; PPF, paired-pulse facilitation; PPD, paired-pulse depression; STDP, spiking time-dependent plasticity; SRDP, spike-rate-dependent plasticity; PHP, probabilistic Hebbian plasticity; EPSP/IPSP, excitatory/inhibitory postsynaptic potential; IF, integrate-and-fire; LIF, leaky-integrate-and-fire; DWM, domain wall motion; FM, ferromagnetic materials; MS, magnetization switching; MTJ, magnetic tunnel junction; STT, spin transfer torque; SOT, spin-orbit torque; VCM, valence change mechanism; PEDOT:PSS, poly(3,4-ethylenedioxythiophene):poly(styrene sulfonate); PDPP, diketopyrrolopyrrole-terthiophene donor-acceptor polymer; BTPA-F, triphenylamine-containing polymer; EV(ClO₄), ethyl viologen diperchlorate. “–” means that no related information.

include satisfactory switching ranges (>3 orders of magnitude), large endurance cycles (≈10⁵), low operation voltage (<3 V), and fast switching speed (≈10 ns).

Wang et al. reported an amorphous α-InGaZnO (IGZO) memristor (Pt/α-IGZO/Pt)-based artificial synapses where ion diffusion is reduced by an oxygen concentration gradient.^[165] Conductance increased upon applying a positive bias to IGZO, causing oxygen ions to move toward the top electrode. Then,

the conductance of the device was reduced by using a negative voltage because oxygen ions moved back to the bottom electrode. In addition, STDP and spike-rate-dependent plasticity (SRDP) were obtained by tuning pulse width and amplitude. Moreover, various learning and experience properties have been achieved in the IGZO device. On the other hand, when IGZO is used as a channel layer in three-terminal transistors where InZnO is used as source and drain, low spike-power

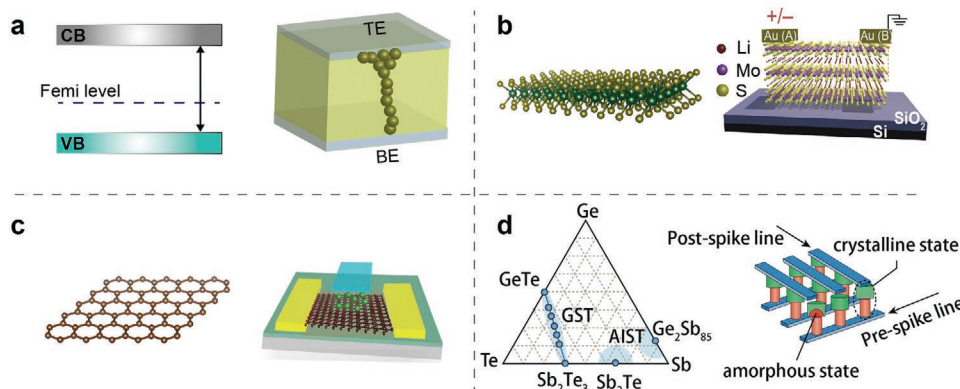


Figure 5. a–d) Representative inorganic materials and corresponding memristive device structures: a) metal oxide semiconductor; b) 2D materials; c) graphene; d) phase-change materials. Right part of (b): Adapted with permission.^[196] Copyright 2019, The Authors, published by Springer Nature. Right part of (c): Reproduced with permission.^[201] Copyright 2015, American Chemical Society. Left part of (d): Adapted with permission.^[26] Copyright 2019, Springer Nature. Right part of (d): Reproduced with permission.^[75] Copyright 2012, American Chemical Society.

consumption of ≈ 0.23 pJ and EPSC were achieved. A heterostructured synaptic memristor comprising an oxygen-rich IGZO layer and an oxygen-deficient HfO₂ film has also been fabricated.^[166] PPF was obtained where the current was increased by the second pulse instead of the first pulse. Furthermore, when an input pulse was applied more frequently, the forgetting rate of the device decreased, which is referred to as SRDP. Like the mechanism of the two-terminal device, the conductance is affected by the oxygen concentration at the interface of the IGZO layer. This mechanism could also explain SRDP, STP, and LTPot behaviors in the IGZO memristor.

Other binary transition metal oxides can also be used in anionic devices to demonstrate the high controllability and reproducibility between HRS and LRS.^[167] Niu et al. fabricated a TiN/Ti/HfO₂/CoSi₂-based memristor with a silicon nanotip, where conductive filaments were confined due to the limited amount of oxidized Ti and CoSi₂.^[105] No significant variations in the resistances of LRS and HRS were observed because oxygen vacancies were aligned along the same conductive filament path. The properties of electronic synapses were changed due to the size and number of conductive filaments. Another type of HfO₂-based resistive memory devices demonstrated that output spikes can be generated when input accumulation exceeds the critical value. In addition, weakly conductive filaments induced by a few oxygen vacancies could be simulated by a Poole–Frenkel analytical model.^[168] Furthermore, Wang et al. modulated the compliance current to change the conductive filaments' physical properties in a Pt/FeO_x/Pt structure. With increasing compliance current, the shape of conductive filaments became wider without the I – V curve overlap.^[169] Meanwhile, the retention performance is enhanced with increasing compliance current. Al/Al₂O₃/Nb_xO_y/Au double-barrier memristors were fabricated by Hansen et al., in which an interfacial reaction resulted in a change of resistance. Amorphous Al₂O₃ and Nb_xO_y function as a tunnel barrier and an ionic conductor, respectively.^[170] Confinement of oxygen vacancies in Nb_xO_y and Al₂O₃ layer creates a gradual switching. Moreover, HH neuron functions can be realized in NbO₂ Mott memristor devices.^[171] The architecture and basic I – V curves of the devices are shown in **Figure 6**. The voltage response under different threshold

voltage inputs showed that only a superthreshold induced an action potential. Under different spiking inputs, experimental and simulated voltage behaviors exhibited corresponding voltage inputs, mimicking other spiking profiles.

Also, Wang et al. demonstrated conductive filament tuning by adding a SiO₂ layer at the TiN/TaO_x interface, which acts as an ion diffusion limiting layer.^[172] Due to the dense SiO₂ microstructure layer, low energy consumption was also realized. The Pt/TiN/SiO₂/TaO_x/Pt structure was then fabricated in a crossbar structure, resulting in many oxygen vacancies in the TiO_x layer for conductive filaments and the TiN layer stored oxygen. Moreover, an increasing linear trend was observed in potentiation and depression curves because oxygen vacancies were attracted to the SiO₂ layer, causing oxygen ion drift from the TaO_x to the SiO₂ layer. The optimal switching with a high on/off ratio and a low nonlinearity was obtained using 1 nm SiO₂ layer. Biological synapse behavior such as STDP could also be realized in this device. Kim et al. simulated Ca²⁺ dynamics with Pd/Ta₂O_{5-x}/TaO_y/Pd oxide heterojunction memristors.^[173] Meanwhile, other phenomena such as behaviors of STDP, potentiation, and depression could be achieved in secondary-state variables without pulse programming.

IF artificial neurons can be constructed by including SiO₂ in the switching layer. A Ag/SiO₂/Au device was connected to a resistor, followed by a parallel attachment to a capacitor.^[174] In this circuitry, four critical neuron functions, termed all-or-none spiking, threshold-driven spiking, refractory period and strength-modulated frequency response, were demonstrated. Vanadium oxide (VO₂) can also be used as an artificial neuron. Lin et al. developed an artificial neuron that possesses IF and postfiring refractory period characteristics under low voltage (0.8 V).^[175] Moreover, Yi et al. demonstrated 23 types of biological neuronal behaviors using scalable VO₂ active memristors.^[176]

WO_{3-x}-based memristors exhibited excellent retention and switching ratios ($\approx 10^5$).^[177] Bienenstock–Cooper–Munro learning rules were investigated in Pt/WO_{3-x}/W second memristors, demonstrating a typical threshold-sliding effect, depending on learning history.^[178] Moreover, Huang et al. developed quasi-Hodgkin–Huxley neurons with LIF functions

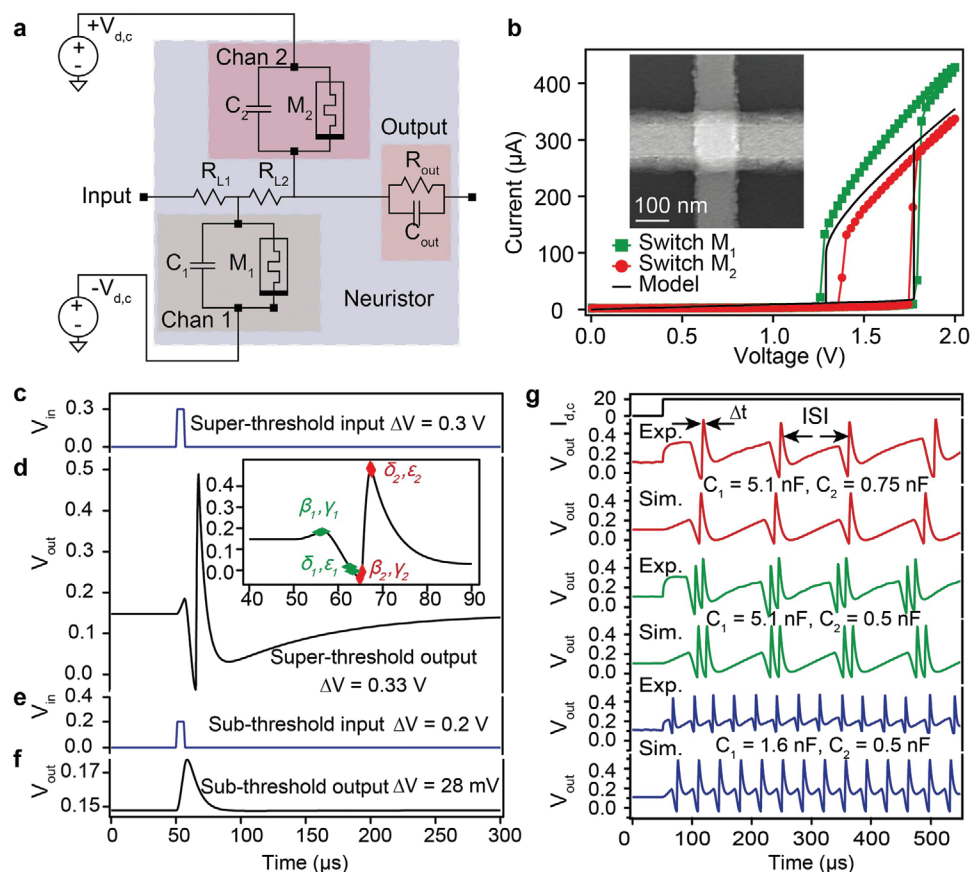


Figure 6. HH axon realized in NbO₂ Mott memristors. a) Schematic of the circuit diagram. b) Experimental and simulated *I*–*V* curves of the device. c–f) Voltage responses under pulsed excitations at different thresholds. g) Experimental and simulated voltage behaviors under different spiking inputs. a–g) Reproduced with permission.^[177] Copyright 2013, Springer Nature.

using W/WO₃/poly(3,4-ethylenedioxythiophene):polystyrene sulfonate/Pt devices. Proton migration contributes to resistive switching by which the efficiency and accuracy of neuromorphic computing is improved upon hyperpotentiation, leading to the first demonstration of a quasi-HH neuron with LIF function.^[179]

2D Materials: In recent years, 2D nanomaterials have emerged for synapse simulation and neuromorphic computing.^[180,181] Transition metal dichalcogenides (TMDCs) MX₂ (M = Mo, W; X = S, Se) are typical materials for memristors and nonvolatile transistors. For sandwiched structures, different conductors (e.g., Ag, Au, Cu, and graphene electrodes) are used as the top and bottom electrodes. For example, MoO_x/MoS₂ and WO_x/WS₂ heterostructures between two silver electrodes showed modulated electrical resistance from 10² to 10⁸ Ω and low operation voltages of 0.1–0.2 V (Figure 7).^[182] A gradient of ion vacancy concentration was created through the device at different depths. STP, LTPot, and binary switching were demonstrated through charge trapping and detrapping near the Ag/MoO_x interface. For all Au electrodes, ultrathin vertical TMDC-sandwiched memristors showed low ON-state resistance (<10 Ω) at a high frequency of 50 GHz and a high switching ratio (>10⁴) due to a point-defect mechanism.^[183,184]

Moreover, an operating temperature (340 °C) higher than the conventional metal oxide memristors (200 °C) has been

achieved by sandwiching few-layer MoS₂ memristors between graphene layers.^[185] Through in situ scanning transmission electron microscopy, a high density of sulfur vacancies was observed in these memristors in the ON-state, and oxygen ions are filled in the sulfur vacancies in the OFF-state. Conversely, due to Cu ion diffusion, bilayer MoS₂ memristors sandwiched between Cu and Au electrodes achieved low operation voltages (≈0.2 V) and also demonstrated STDP in 2D memristors for the first time by altering the pulse patterns.^[186] To realize large-area, flexible and printable neuromorphic circuits, research has been conducted on solution-processed 2D materials. For example, vertical memristors and memcapacitors based on solution-processed 2H and 1T' MoS₂ films can work at low global fields of ≈10 kV cm⁻¹.^[187,188]

In principle, memristors are two-terminal devices with varying resistance, which cannot satisfy the need of multi-terminal simulation for higher-order synaptic plasticity. Hence, combining memristors and transistors in the form of memtransistors may solve the problem. Unlike traditional thin-film transistors, memtransistors offer both drain- and gate-tunable nonvolatile memory functions. These were first realized using silicon and metal oxide synaptic transistors.^[189] For 2D materials, channel gate-tunable memristive switching was observed in substoichiometric monolayer MoS₂ devices with individual grain boundaries.^[190] Subsequently, multi-terminal

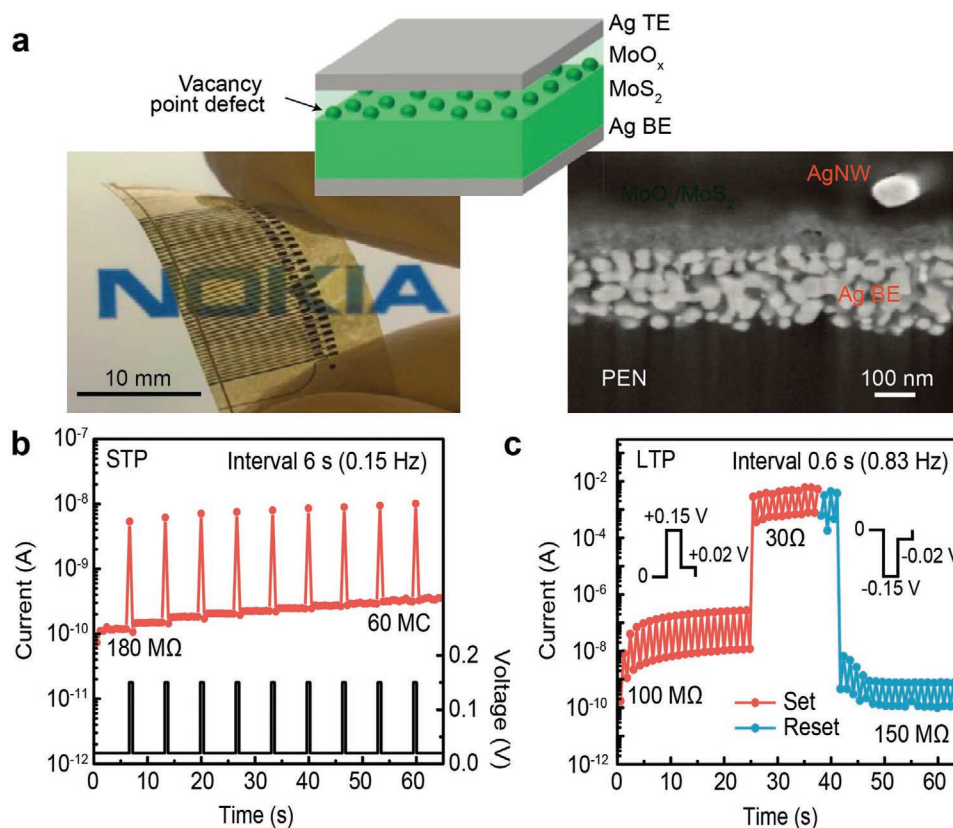


Figure 7. STP and LTP properties of 2D MoS₂-based artificial synapses. a) Structure and optical image of an Ag/MoO_x/MoS₂/Ag device. b) STP and c) LTP behaviors under different pulse intervals. a–c) Reproduced with permission.^[182] Copyright 2015, Springer Nature.

memtransistors of polycrystalline MoS₂ were fabricated,^[191,192] in which the open architecture of the 2D channel further enabled multi-terminal heterosynaptic plasticity (Figure 8).^[191] MoS₂ defects were moved under a bias voltage, driving resistive switching through variation of the Schottky barrier height. This mechanism was revealed through in situ scanning probe microscopy, cryogenic charge transport measurements, and device modeling. LTPot and LTD were mimicked by repeating 1 ms of positive- and negative-bias pulses. Furthermore, STDP was observed by positive and negative paired pulses with a time interval, analogous to the response times of biological synapses.^[193,194] Wang et al. extended research on this three-terminal device, achieving a tenfold decrease in operating voltage through smaller grain boundary sizes and ultrathin dielectrics.^[195]

Recently, another example of simulating heterosynaptic plasticity was developed in the 2H-1T' phase transition of MoS₂ memtransistors (Figure 9).^[196] The *I*–*V* curve changed from nonlinear and asymmetric to linear and symmetric after lithiation due to the interfacial formation of the metallic 1T' phase and the Ohmic contacts. Meanwhile, good device controllability with low variability has been achieved compared to conventional memristors involving defect doping and filament formation.^[197,198] In biological systems, heterosynaptic plasticity represents synaptic competition and cooperation. This usually occurs during intense postsynaptic activities caused by a connected, activated presynaptic neuron that triggers diffusion of synaptic-related proteins in the postsynaptic neuron. Synaptic

competition can be mimicked by two neighboring devices sharing a single electrode G in-plane. In this structure, regions of electrodes (A and B) and the interfacial area (G) represent presynaptic and postsynaptic dendrites, respectively. The initial process corresponds to Li⁺ ion accumulation in the region under electrode G. Then, negative pulses are sequentially applied to terminals A and B, resulting in a greater accumulation of Li⁺ ions and more pronounced variance in conductance in the first device than the other one. It simulates the synaptic competition behavior of biological systems because the activity of other synapses within the same dendrite is reduced when a synapse undergoes potentiation. In addition, synaptic cooperation has been realized in this device. Li⁺ ion-induced memristive effects offer multiple advantages, such as better controllability, lower power consumption, and localized ionic coupling in synaptic devices of a network. 2D materials based devices have also been developed for sound localization and audiomorphic computing due to their local thermal effects and weak electrostatic screening.^[199,200]

Graphene: Graphene is a 2D material comprising a single layer of carbon arranged in a honeycomb lattice, which can also be used in artificial synapses. It can serve as a bottom electrode, a dielectric layer, and also as an ion-blocking layer.^[201–206] For instance, an artificial synapse with multilevel regulatable plasticity was first realized in ambipolar, twisted-bilayer, graphene-based synaptic transistors. Excitatory, inhibitory, and STDP properties were obtained in this single device

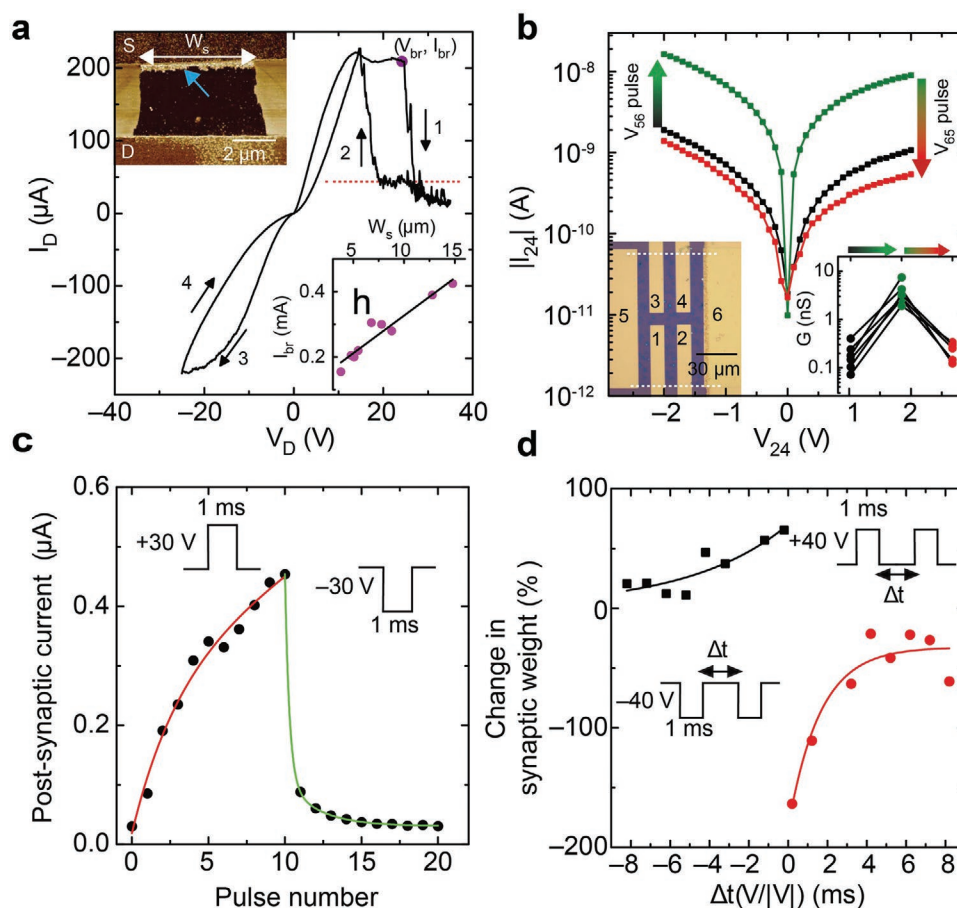


Figure 8. Heterosynaptic plasticity in multi-terminal polycrystalline MoS₂ devices. a) I_D - V_D curve of a monolayer MoS₂ domain. b) I_{24} - V_{24} curve before and after applying voltage between terminals 2 and 4. c) LTPot and LTD properties with 30 and -30 V pulses. d) PPF properties displayed under 40 and -40 V pulses. a-d) Reproduced with permission.^[19] Copyright 2018, Springer Nature.

by changing the bottom gate voltage. Moreover, flexible neuromorphic devices based on graphene oxide electrolyte films have shown both spatial and temporal modes. Graphene oxide can also act as a solid-state ionic conductor in transistors with a combination of indium zinc oxide semiconductors, enabling controlled ion transport.^[207] A high current ON/OFF ratio (10^6) and a low subthreshold slope (≈ 100 mV dec⁻¹) were obtained in this device. Similarly, in-plane diffusion of Li⁺ ions in graphene synapses allows low-power (<500 fJ per event), multistate memory (>250 states). In nanoscale, the power consumption of one switch was lowered to 4 aJ at 10 MHz.^[208] Lateral contacts involving graphene edges in memristors also enabled 3D architectures of memory and logic gates.^[209]

Other 2D materials can also serve as hosts for memristive devices. Tian et al. demonstrated a black phosphorus-based synaptic device by utilizing the in-plane, anisotropic electronic properties of the phosphorus.^[210] The charge transfer between the 2 nm native oxide of the black phosphorus and its channel enables LTPot/LTD and STDP as well as a simple, compact heterogeneous axon-multisynapse network. Both volatile and nonvolatile resistive switching conditions were achieved simultaneously in few-layer, hexagonal boron nitride (hBN), emulating STP, LTPot, and STDP synaptic behaviors. The researchers showed fast (≈ 200 μs), stable relaxation

over 500 cycles. They argued that the pulse voltage is a more important factor influencing potentiation than the pulse time/interval, with a 600 pW power consumption per transition in the volatile region. In addition, memristor-based hBN and electrochemically active metals (Cu or Ag) can support metal ion diffusion through point defects.^[200,211,212]

PCMs: PCM-based synapses with nanoscale dimensions and low energy consumption (\approx pJ) provide opportunities for power-efficient neuro-inspired computing. Different synaptic properties can be obtained by varying input pulse parameters, such as amplitude, length, and spacing. STDP was accomplished in a single PCM cell synapse.^[75] In addition, large-scale neural networks and spiking neural networks (SNNs) can reduce the power needed for visual pattern extraction and recognition.^[213–216] For example, by implementing a PCM-based hybrid hardware–software neural network, the classification of MNIST was completed with a 100-fold decrease in energy consumption.^[214] On the other hand, PCMs can simulate IF neurons through the low conductance of the amorphous state, which can be set as the neuronal membrane potential (Figure 10).^[217] Neuronal firing occurs when a highly recrystallized phase reaches a threshold conductance. A melting voltage pulse then resets the neuron. By changing the pulse amplitude, width, and frequency, the rate of phase-change neuronal firing can

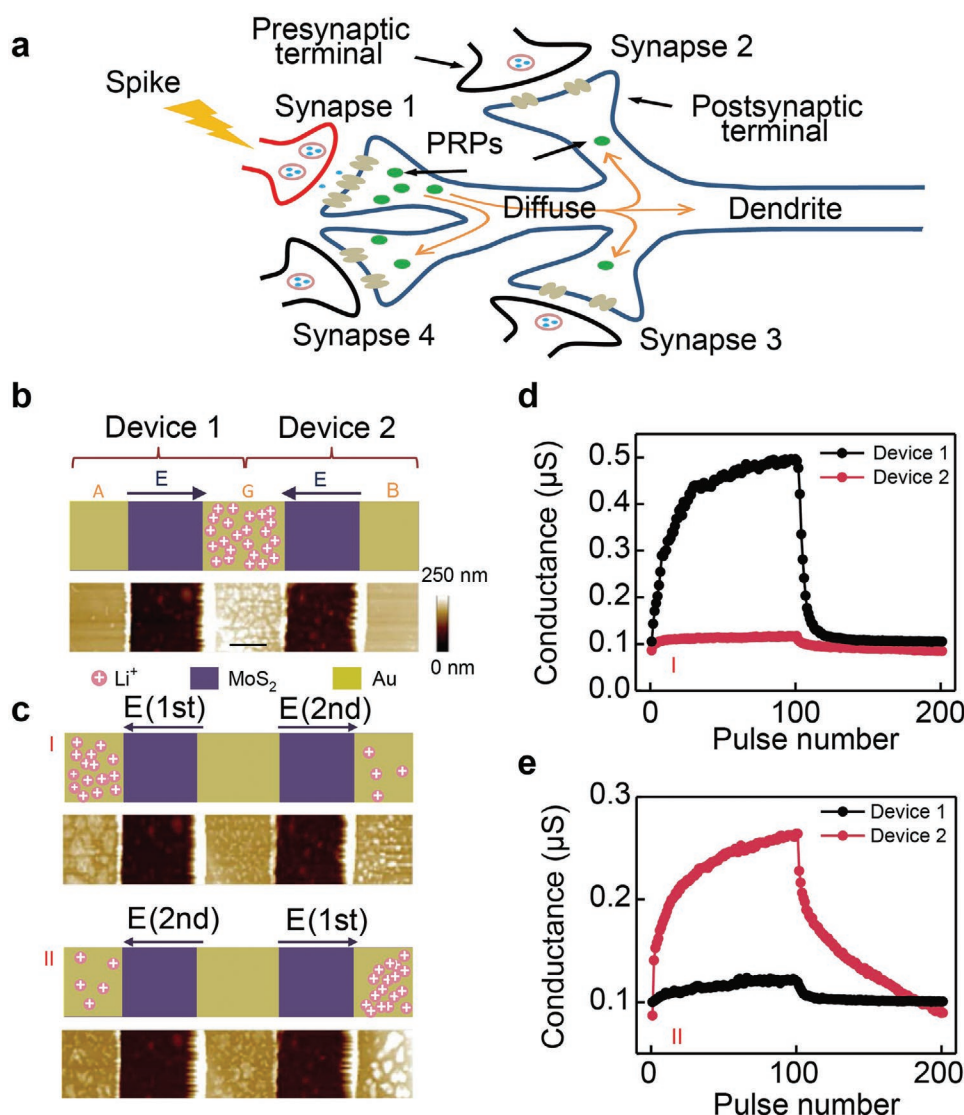


Figure 9. Experimental implementation of synaptic competition. a) Schematic graph of synaptic competition and heterosynaptic cooperation functionality. b–e) Experimental implementation of synaptic competition in Li_xMoS_2 devices using two adjacent devices. b–e) Reproduced with permission.^[196] Copyright 2019, The Authors, published by Springer Nature.

be modulated. Phase-change neurons are ideal for completing complex tasks, for example, detecting temporal correlation in parallel data streams with the help of plastic synapses.^[217] Furthermore, crystallization processes enable the stochasticity of PCM-based neurons, which can be modulated by varying amorphous topology and chemical bond strength. For example, the crystallization rate increases from ns to ms, and the neuron's firing rate changes orders of magnitude by adding Sc into Sb_2Te_3 . This is accomplished by suppressing stochasticity, yielding a higher nucleation rate, because strong Sc–Te bonds stabilize crystalline precursors under temperature variation.

Other Inorganic Materials for Electronic Memristive Devices: Ag nanoparticles: Ag nanoparticles can improve the performance of resistive switching memory by reducing power consumption. For example, dispersed Ag nanoparticles facilitate filament formation. $\text{TaN}/\text{Al}_2\text{O}_3/\text{ZnO}/\text{ITO}$ devices with dispersed Ag nanoparticles were reported as an artificial synapse, in which

HRS and LRS were obtained in I – V sweeps and potentiation/depression behaviors were observed.^[218] Notably, there is great potential for polymer–metal nanoparticle composites as memristors and artificial synapses due to their versatile functionality, flexibility, low cost, nontoxicity, and biocompatibility. Metal and different capping ligands determine resistive switching characteristics of organic–metal nanoparticles. For example, Zhou et al. fabricated an $\text{Au}@\text{Ag}$ core–shell nanoparticle composite by increasing charge trapping and migration relative to an individual component.^[219] Electrons are trapped by $\text{Au}@\text{Ag}$ nanoparticles when a positive voltage is applied, which corresponds to LRS after full trapping, whereas electron detrapping occurs upon application of a negative bias. A more effective filament forms because dispersed $\text{Au}@\text{Ag}$ nanoparticles act as separate nucleation centers that enhance nucleation of Ag atoms. The device also showed PPF, SRDP, and STDP synaptic behaviors (Figure 11a–c). Moreover, Ag nanoparticles can simulate the

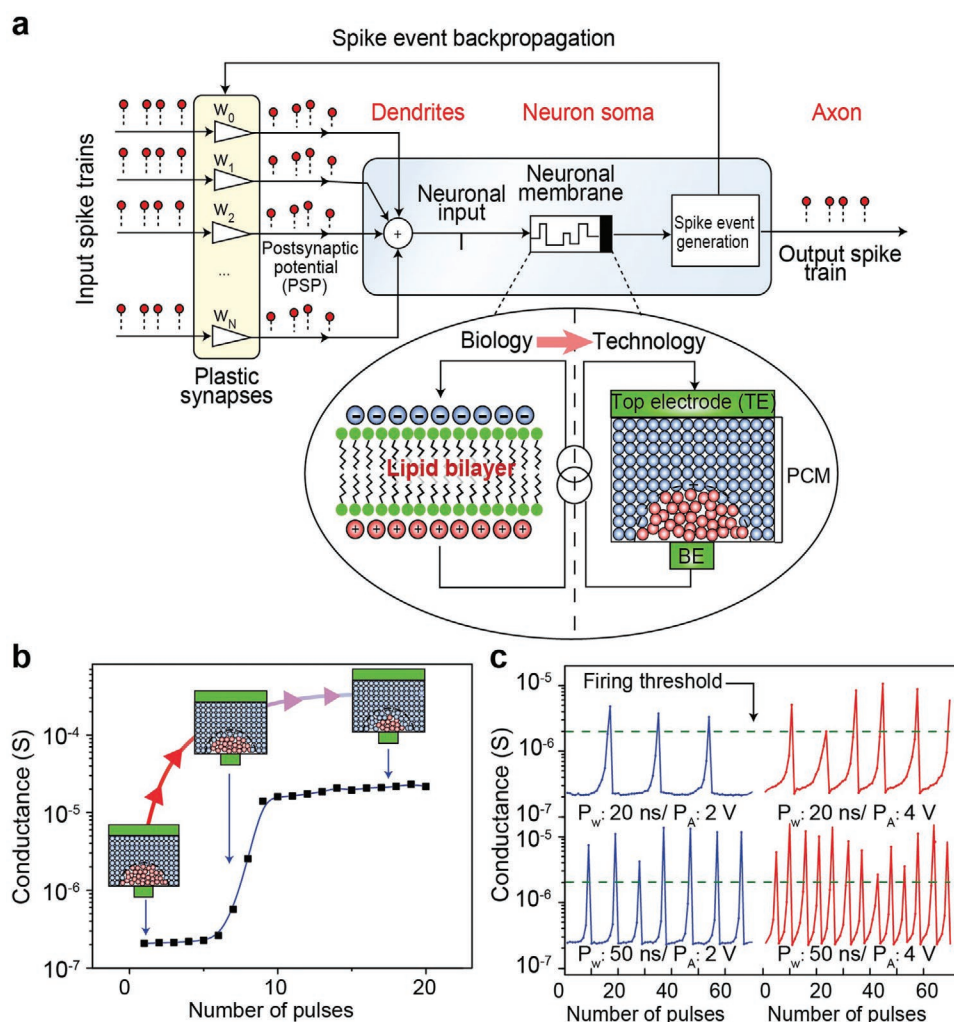


Figure 10. Properties of PCM-based neurons. a) Artificial neuron architecture based on a phase-change device. b) Conductance change with the number of pulses applied to the device. The neuron displayed firing after six pulses were applied. c) Integrate-and-fire dynamics under excitation with different pulse widths (P_w) and amplitudes (P_A). a–c) Reproduced with permission.^[127] Copyright 2016, Springer Nature.

dynamic process of Ca^{2+} in biosynapses (Figure 11d,e).^[72] A diffusive memristor was achieved when it was embedded in a SiO_x matrix. Learning behavior, PPF, and PPD were also observed in this device due to dynamic contraction and extension of Ag nanoparticles (Figure 11f,g).

Perovskite: Perovskite oxides such as SmNiO_3 (SNO), BiFeO_3 (BFO), SrTiO_3 , and SrRuO_3 can be utilized for memristors and memristor-based synapses, in which oxygen ions aggregate locally at the interface.^[220–224] STDP curve was observed in a Pt/BFO/Au structure by Mayr et al.^[225] Artificial synapses with SNO were also demonstrated in three-terminal transistors by modulating the density of oxygen vacancies in the SNO channel via electrochemical reactions through the ionic liquid (IL)–SNO interface.^[220] In contrast to two-terminal memristive devices, three-terminal electronic synapses offer combined stimulus transmission and learning processes. Potentiation and depression were generated by applying positive and negative voltage. In addition, symmetric and asymmetric STDP curves, as determined by the sequence of drain spikes and source spikes, were observed.

4.1.2. Organic Materials for Electronic Permissive Devices

Compared with inorganic synapses, organic synapses are promising components of neuromorphic circuits due to their low cost, flexibility, low energy consumption, and biocompatibility.^[126,226,227] However, some major drawbacks of these devices include high variability, long switching time, poor endurance, and poor retention capability. Recently, Burgt et al. demonstrated the potential of synaptic cells, based on Nafion and poly(3,4-ethylenedioxythiophene):polystyrene sulfonate (PEDOT:PSS), for neuromorphic computing (Figure 12).^[123] A nearly perfect linear function was obtained in this device. Low energy consumption (<10 pJ for $10^3 \mu\text{m}^2$ devices) and LTPot and LTD properties were achieved, accompanied by over 500 distinct states. STP and PPF properties were also obtained by controlling the time interval between two short pulses. Moreover, Pavlovian conditioning was realized in this device. Initially, only input neuron N_1 can activate output neuron N_3 , while neuron N_2 does not. Through permanently associating N_2 with N_1 by learning-induced synaptic weight modification of the device,

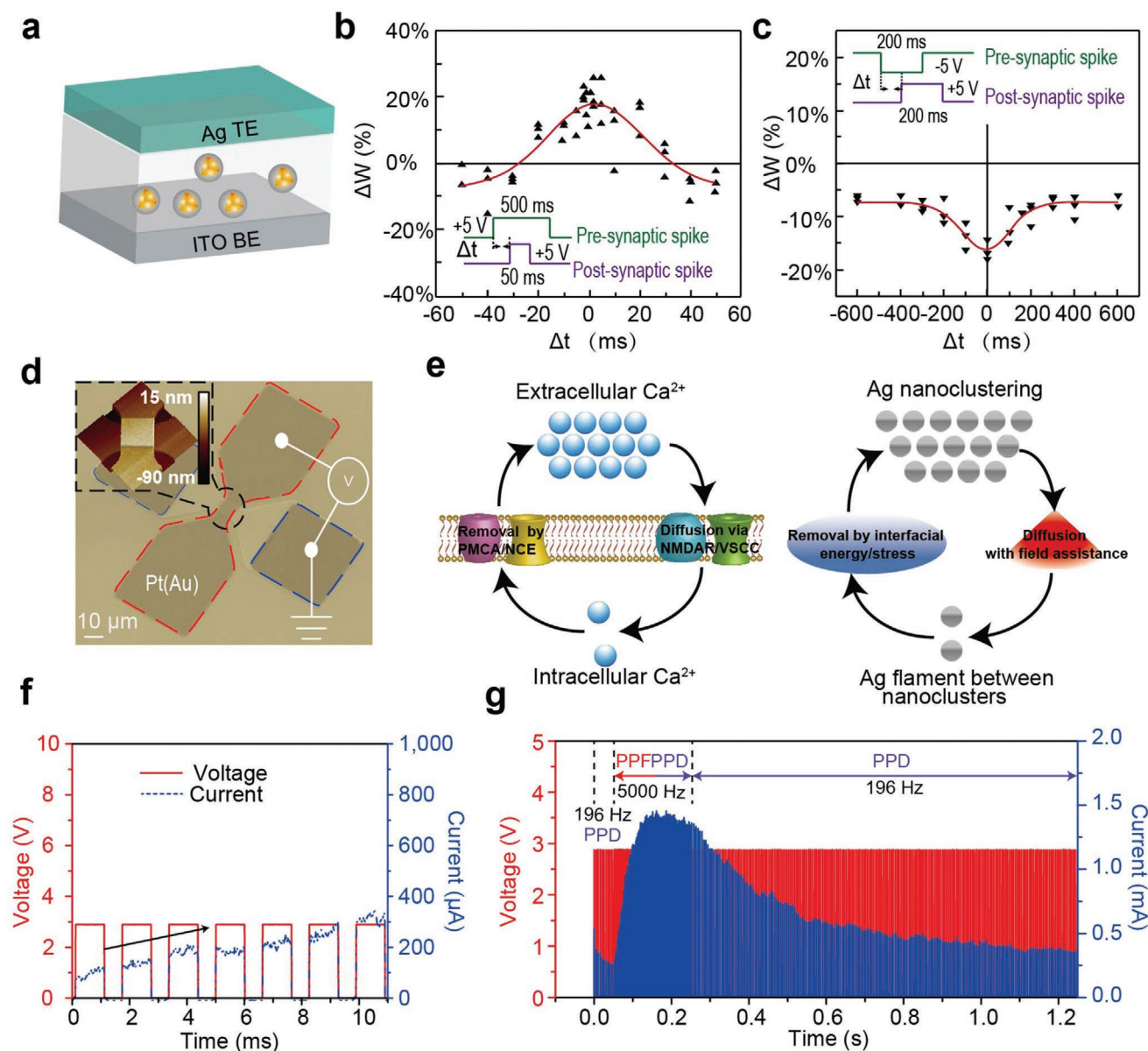


Figure 11. Structures and synaptic properties of Ag-based synapses. a) Schematic illustrations of Au@Ag nanoparticle-dispersed PVP synapses. STDP behaviors that follow symmetric b) Hebbian and c) anti-Hebbian learning rules by different programmed synaptic pre- and post-pulses. d) SEM imaging of memristive device structures consisting of two Pt or Au electrodes and a switching layer with embedded Ag nanoparticles. e) A Ca^{2+} and Ag dynamic process in biological and $\text{SiO}_x\text{N}_y\text{:Ag}$ synapses. f, g). Experimental demonstration of PPD and PPF in a $\text{SiO}_x\text{N}_y\text{:Ag}$ memristive device. a–c) Reproduced with permission.^[219] Copyright 2018, American Chemical Society. d–g) Reproduced with permission.^[72] Copyright 2017, Springer Nature.

input N_2 could elicit a response at N_3 , thus mimicking the associative memory of biological synapses.

Usually, organic transistors work at tens of kA cm^{-2} .^[228] However, a current density at the level of MA cm^{-2} is needed for highly integrated, high-performance electronics, which compromises the low-power operation in neuronal networks. Recently, diketopyrrolopyrrole–terthiophene donor–acceptor polymer (PDPP) was used to fabricate a vertical-structured organic transistor, displaying MA cm^{-2} switching with a 10^8 -switching ratio (Figure 13).^[229] Furthermore, the switching energy needed per event is in the sub-pJ scale, showing a perfect combination of high on-state conductivity (5000 S m^{-1}), large current tunable

ratios, and low operation energy (10–100 fJ). Synaptic properties such as STP and LTPot were also achieved using this device.

Several other organic material-based systems also exhibit good performance. For example, sputtering Au nanoparticles onto the surface of ITO/ $[\text{Ru}(\text{L})_3](\text{PF}_6)_2/\text{Au}$ devices showed superior performance, with lowered resistance on a small scale device of 60 nm^2 and an improved switching time of 30 ns.^[230] Energy consumption of 1.5 fJ per bit was achieved with unchanged endurance and stability. In this device, it exhibits high reproducibility (≈ 350 devices). In addition, an ethyl viologen diperchlorate $[\text{EV}(\text{ClO}_4)]/\text{triphenylamine-containing polymer (BTPA-F)}$ organic system was first demonstrated by Liu et al.

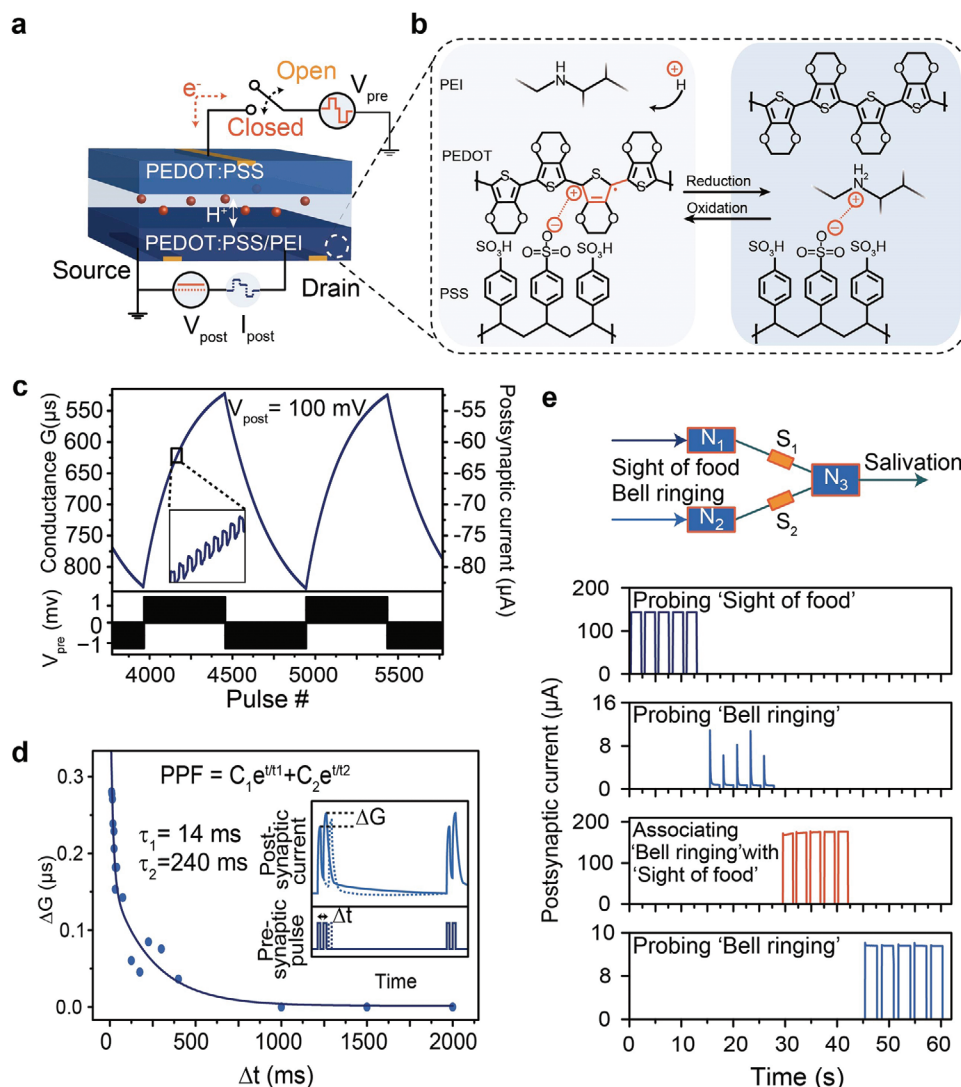


Figure 12. Neuromorphic behavior of the PEDOT:PSS device. a) Schematic of the device structure. b) Molecular reduction process of PEDOT:PSS. c) LTPot and LTD properties when the device is applied with voltage pulses. d) STP and PPF properties. e) Pavlovian learning circuits. a–e) Reproduced with permission.^[123] Copyright 2017, Springer Nature.

In addition to SRDP and STDP synaptic behaviors, STM to long-term memory (LTM) and learning–forgetting–relearning memory behaviors were mimicked in this device.^[231] Inspired by natural plants, chlorophyll/PDPP4T based photoresponsive organic FETs also showed EPSC, PPF, STM, and LTM behaviors.^[228] Meanwhile, the device exhibited good responsivity even after storage in air for 90 days.

4.2. Materials for Magnetic Memristive Devices

Magnetic memory has been prevalent for several decades; therefore, the maturity of magnetic device technology and manufacturing offers spintronic memristors advantages over other materials. In recent years, various synaptic and neuronal behaviors have been demonstrated through MTJ-based spintronic memristors.^[232–235] These MTJs are composed of two

ferromagnetic layers encompassing an oxide tunneling barrier that is most often, if not always MgO, due to its superior tunneling magnetoresistance ratio. One of the layers (pinned layer) has a fixed magnetic polarization, while the other layer (free layer) can be altered via external stimulation, such as incoming spin-polarized current. Various MgO-based MTJ devices have been proposed to mimic a variety of synaptic phenomena. For example, Park and co-workers connected multiple PtMn/CoFe/Ru/CoFeB/MgO/CoFeB MTJs in series to mimic the associative memory of the brain.^[236] They demonstrated that the association of individual electrical signals below the switching current threshold induced magnetization switching events, generating output signals. Roy et al., through theoretical simulations, demonstrated that MTJs can simulate volatile memory and LTPot, similar to biological synapses (Figure 14).^[237] By generating multiple low energy input pulses in a short period (2.5 ns), they showed an additive effect of these pulses to

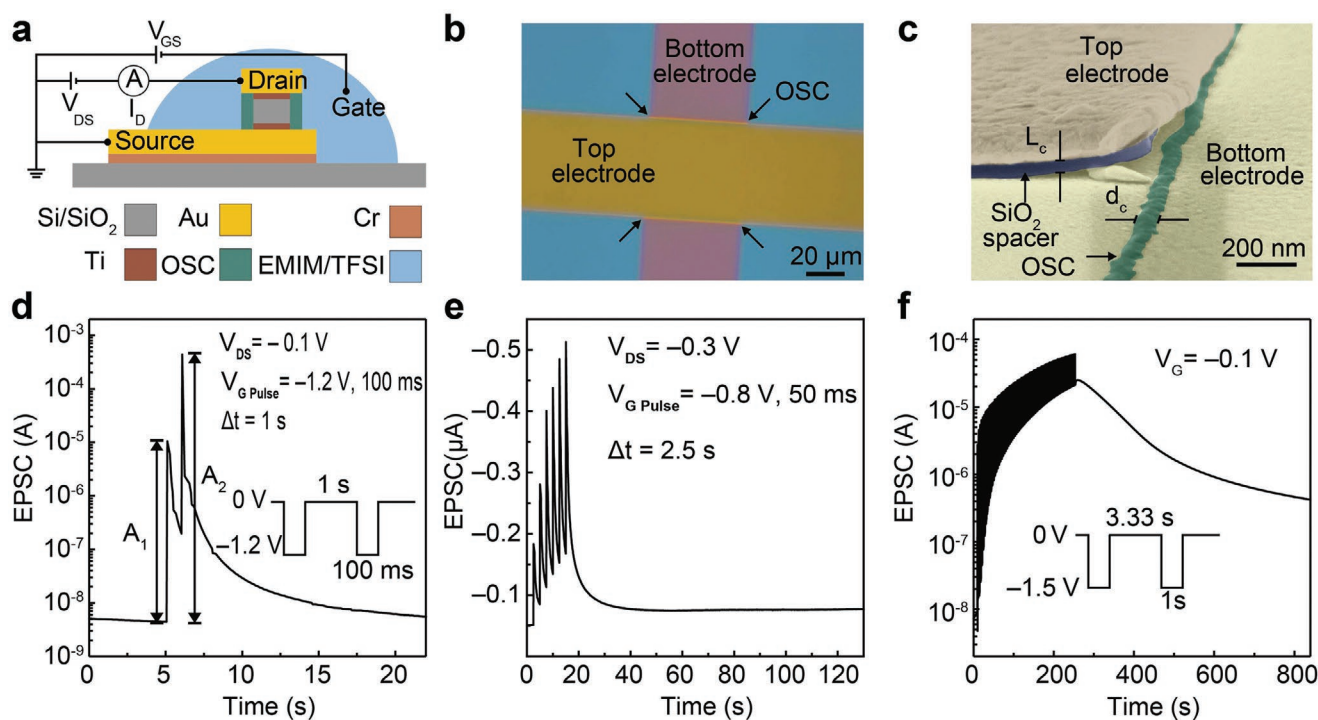


Figure 13. STP and LTPot of an electrolyte-gated PDPP VOFETs device. a–c) Structure of the transistor. b) Polarization microscopy image of a finished VOFET without an electrolyte gate. c) Colored cross-sectional SEM image of the device. d–f) EPSC triggered by presynaptic spikes with different spike intervals. a–f) Reproduced with permission.^[229] Copyright 2019, The Authors, published by Springer Nature.

induce magnetization switching. However, if the frequency of the pulse was too low, or stopped before switching occurred, the magnetization state reverted to its original state, demonstrating volatility. This theoretical calculation was then proven practically using two MTJ-heavy metal heterostructures to mimic stochastic synapses capable of LTPot. Recently, Zhang et al. developed a domain wall memristor based on Ta/CoFeB/MgO heterostructures.^[238] Through induction of domain wall movement in the CoFeB layer, both LTPot and LTD were demonstrated by modulating the number of negative pulses. Synaptic plasticity such as STDP was also demonstrated with both magnetization switching and domain wall-based MTJ devices.^[239] In addition, Cao et al. designed a multistate ferromagnet by intercoupling a binary ferromagnet with another in-plane ferromagnetic layer.^[240] Through SOT-driven domain wall motion, the device demonstrated other synaptic functionalities beyond STDP, such as excitatory and inhibitory postsynaptic potentials.

Beyond artificial synapses, researchers have been considering various MgO-based MTJ devices to mimic a variety of neuronal phenomena. However, one of the problems with synthetic spintronic neurons is their inability to model the volatility in biological neurons. Therefore, researchers have implemented various strategies to simulate leakage if the external input is stopped. In 2016, Roy and co-workers demonstrated the first application of leaky-integrated switching of an MTJ-heavy metal heterostructure to model stochastic spiking neurons.^[241] Apart from being a better model of biological neurons and synapses, this design decouples reading and writing current pathways, thus preventing read-write conflicts and improving the reliability of

the device. Two years later, Friedman's group developed the first LIF neuron with lateral inhibition using a domain wall MTJ coupled to a permanent ferromagnet beneath the domain wall track (Figure 15).^[242] Unlike a normal domain wall MTJ, the ferromagnet causes the domain wall to shift in the opposite direction as the current applied. Therefore, if the current is stopped, the domain wall would eventually move back to its original starting position, simulating neuron leaking (Figure 15b). To prevent firing at the same time in the array, neurons are carefully arranged such that those carrying a higher current inhibit adjacent ones with lower current due to magnetostatic coupling, thus inducing a further reduction in their domain wall velocity (Figure 15c). Another LIF neuron design proposed by Agrawal and Roy does not need an additional ferromagnet for leaking.^[243] Instead, leaking is caused by shape anisotropy because the shorter pinned layer is placed at one end of the longer CoFeB-free layer. When the domain wall shifts away from the equilibrium position due to a current input, there is a change in the azimuthal angle of the domain wall, causing the domain wall to drift back to the equilibrium position. In the same year, Friedman's group also came up with an artificial LIF neuron using shape anisotropy.^[244] With a trapezoidal free layer, the domain wall naturally drifts toward the lower energy narrower edge, simulating leaking. Creative designs by these research groups in recent years allow controlled simulation of LIF neurons and in-depth study of neuronal phenomena.

Switching beyond the traditional MTJ design has also been demonstrated. Sui and co-workers recently simulated the network of a synapse using cellulose@Fe₃O₄ nanoparticles.^[245] Capitalizing on the superparamagnetic properties of iron oxide

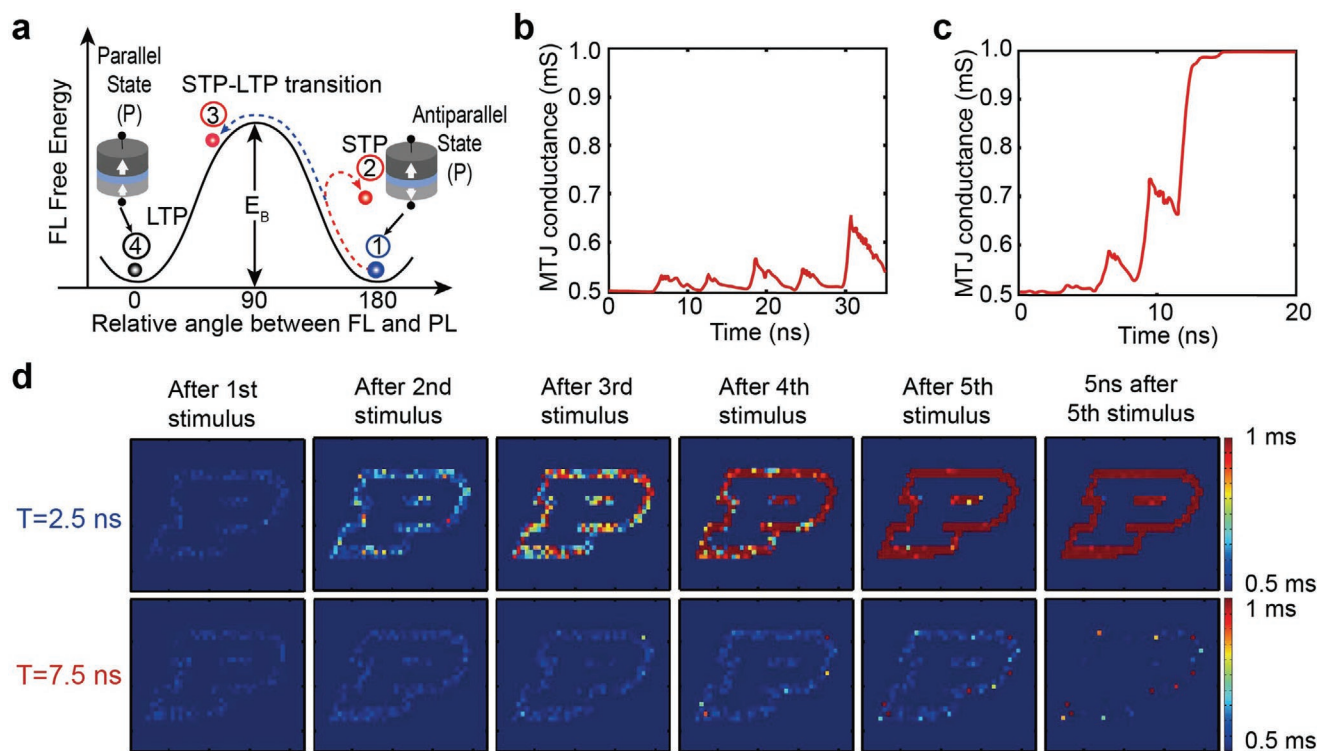


Figure 14. STP–LTP behavior in an MTJ-based device. a) The energy landscape of the free layer (FL). Upon receiving an input stimulus, the MTJ transitions from its initial low-conductance AP state to the high-conductance P state. This transition depends on the time interval between each input, demonstrating STP–LTP behavior. b) STP behavior exhibited by an MTJ synapse with an input stimulus of 100 μA for 1 ns and a time interval of 6 ns between pulses. c) Transition to the LTP behavior exhibited by a MTJ synapse when the time interval between pulses is reduced to 3 ns. d) Short-term memory (STM) and long-term memory (LTM) transitions exhibited in a 34×43 MTJ memory array. Five sets of pulses (100 μA , 1 ns) are applied to each “on” pixel. With a time interval, $T = 2.5$ ns, the array transitions to LTM progressively with each stimulus, while “forgetting” the input pattern when T is increased to 7.5 ns. a–c) Reproduced with permission.^[237] Copyright 2016, American Physical Society.

nanoparticles that depend on electron transfer between Fe^{2+} and Fe^{3+} in the crystal structure, they managed to develop a magnetic synapse network with small hysteresis loops and low coercivity. Meanwhile, magnetic neurons and synapses based on alternative mechanisms have also been demonstrated. To utilize these mechanisms, device designs that comprise different materials have been used. One such example utilized magnetic skyrmions. A skyrmion-based neuron that could mimic LIF neuron function in a single device was realized by using a Co/Pt-based nanotrack.^[246] Moreover, a voltage-controlled skyrmion memristor for synapse arrays with ultralow energy consumption of 5 aJ was developed through addition of a ferroelectric lead magnesium niobate–lead titanate crystal to a MTJ.^[247] Besides MTJs, Josephson junctions can be used to mimic synapses. Rippard and co-workers recently demonstrated that magnetic Mn nanoclusters in a silicon layer between two superconducting Nb electrodes changed magnetic states at extremely low energies (<1 aJ).^[248] Mishra et al. developed a three-terminal Pt/Co/GdO_x artificial synapse based on magnetization of Co, where an applied electric field migrates oxygen ions into or out of the Co layer, depending on its direction, thus affecting Co layer magnetization and its corresponding anomalous Hall resistance.^[249] Based on this mechanism, the authors developed a synapse design that generated positive and negative synaptic weights.

4.3. Materials for Photonic Memristive Devices

Furthermore, data storage and processing have been achieved with unparalleled bandwidth and speed, low-power consumption, and multidata storage based on photonic memristive devices and neuromorphic computing.^[250–255] Two-terminal devices based on oxide heterojunction memristors were developed to simulate multiple synaptic plasticities under photoirradiation. The ZnO_{1-x}/AlO_y heterojunction fabricated by Hu et al. exhibited STP, LTP, PPF, and neuromorphic activation/depression due to the trapping/detrapping of the AlO_y layer.^[252] In addition, Gao et al. demonstrated a simple indium tin oxide/Nb-doped SrTiO₃ structure, which displayed PPF, STM, LTM, and learning-experience behaviors in response to optical stimuli over the entire visible region.^[254] Kumar et al. demonstrated another all-oxide-based photonic synapse with high transparency, which exhibited STP, LTP, and PPF under ultraviolet illumination.^[255]

2D material-based photonic synapses can also be achieved through two-terminal and three-terminal structures. For example, an efficient neuromorphic visual system was achieved with simple, two-terminal, optoelectronic resistive random access memory (ORRAM)-based devices that demonstrate non-volatile optical resistive switching and light-modulated synaptic behaviors.^[256] The Pd/MoO_x/ITO sandwich structure has the two-terminal ORRAM design (Figure 16a). STP under high

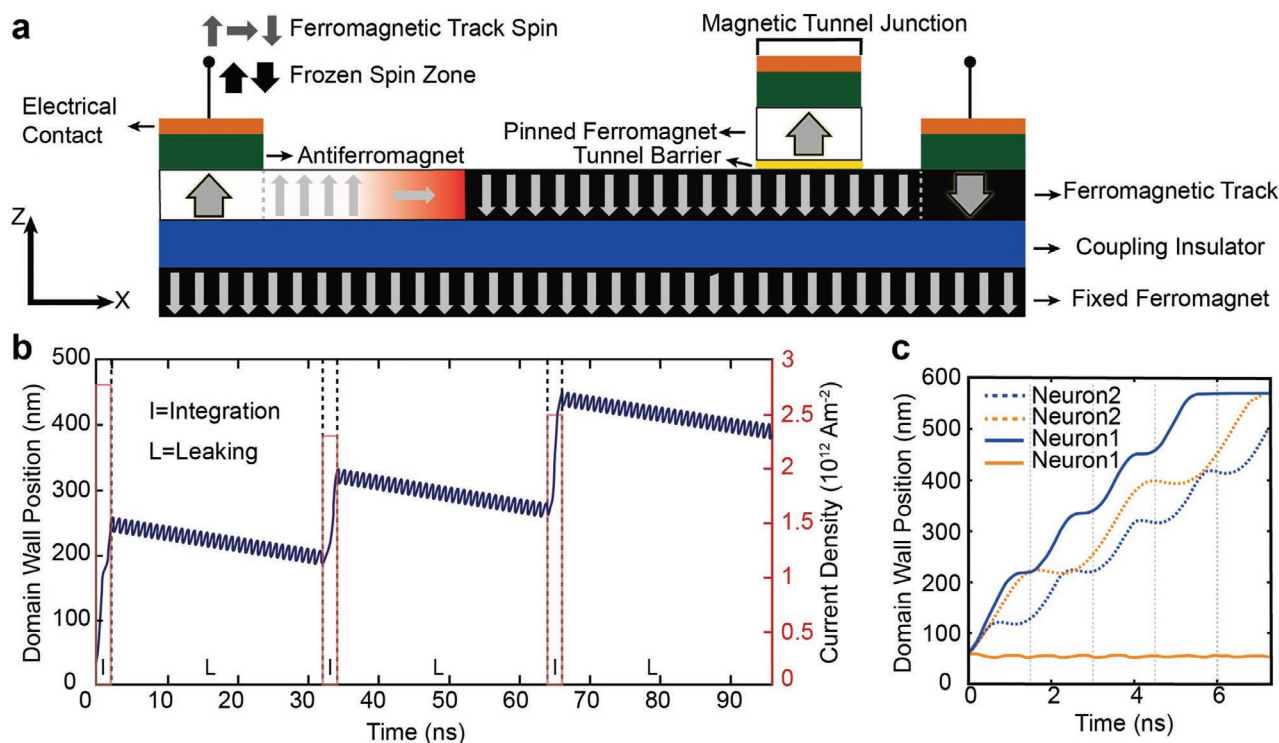


Figure 15. DW-MTJ neuron. a) Schematic illustration of the DW-MTJ neuron. Leaking is induced via a fixed ferromagnet that provides a constant magnetic field, while integration is induced when enough current passes through the two electrical contacts. b) Exhibition of leaking and integration functionalities of the DW-MTJ neuron. When three consecutive current pulses of varying magnitude (2.75 , 2.3 , and 2.5×10^{12} A m $^{-2}$) were applied for 2 ns, integration was demonstrated. On the other hand, between each pair of pulses are an interval of 30 ns without applied current, in which the magnetic field of the fixed ferromagnet induces an opposite DW motion, simulating leaking. c) Demonstration of lateral inhibition between two neighboring neurons. Current pulses of 2×10^{12} (solid orange line) and 0 A m $^{-2}$ (solid blue line) were applied to neuron 1. Current pulses of 1.5×10^{12} A m $^{-2}$ was applied to neuron 2. a–c) Reproduced with permission.^[242] Copyright 2018, AIP.

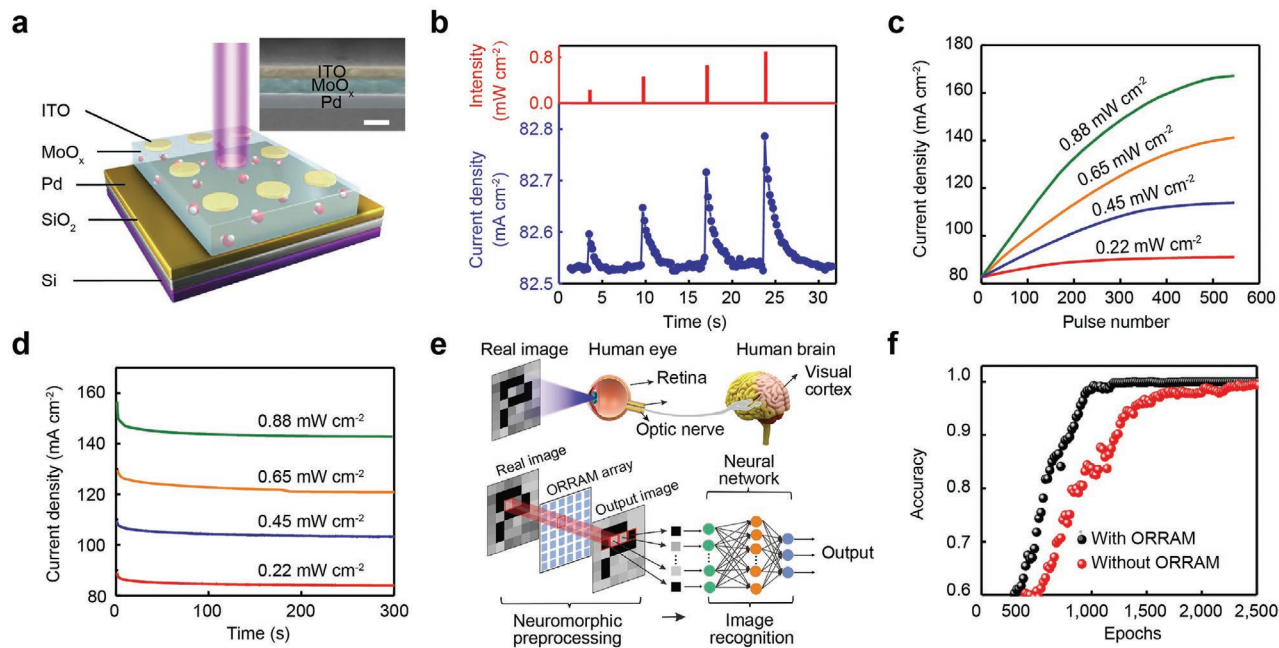


Figure 16. Properties of two-terminal optoelectronic synaptic devices. a) Schematic structure of the MoO $_x$ optoelectronic device. b) Light-intensity tunable STP. c) LTPot with the pulse number up to 500. d) The transition from STP to LTPot at different light intensities. e) Schematics of the human visual system and an artificial neuromorphic visual system comprising an optoelectronic device and an artificial neural network. f) Improvement of image recognition rate with optoelectronic memristive device preprocessing. a–f) Reproduced with permission.^[256] Copyright 2019, The Authors, published by Springer Nature.

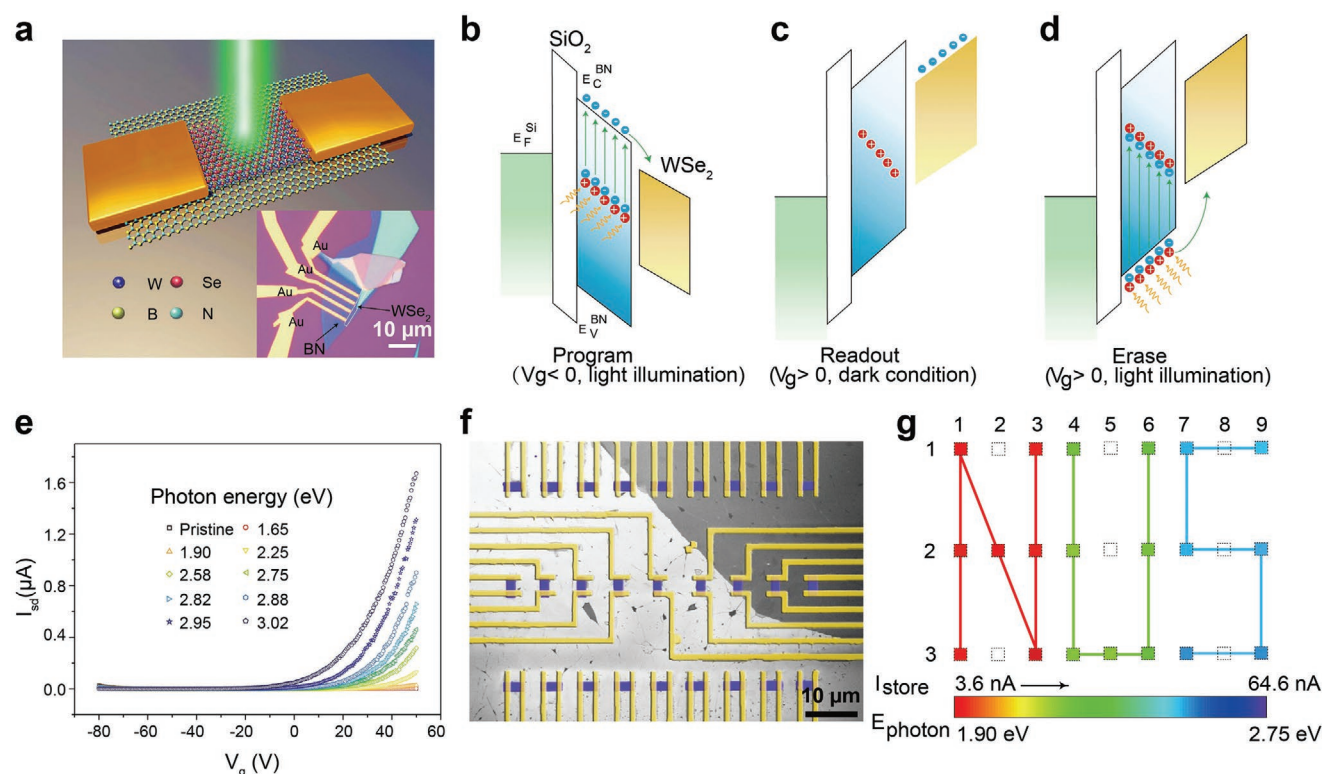


Figure 17. Properties of multibit optoelectronic devices based on field-effect-transistor (FET) devices. a) Design of a WSe₂/BN heterostructure-based optoelectronic memristive device. b–d) Schematic mechanism of the FET under programming (b), readout (c), and erasing (d) processes. e) Transfer curves at different photon energies. f) SEM image of 3 × 9 WSe₂/BN arrays. g) Current response of the array under irradiation at three different photon energies (638, 515, and 473 nm). a–f) Reproduced under the terms of the CC-BY Creative Commons Attribution 4.0 International license (<https://creativecommons.org/licenses/by/4.0>).^[257] Copyright 2018, The Authors, published by Springer Nature.

light density stimulation showed significant spike currents and extended relaxation times (Figure 16b). STP was transmitted to LTPot through repeated-pulse stimulation (500 identical pulses), during which the current increased steadily with increasing pulse number (Figure 16c). Retention profiles after 300 pulses were recorded for 300 s. Increasing pulse number resulted in systematic increases in photogenerated carriers (Figure 16d). The human visual system could be mimicked by combining ORRAM devices and an artificial neural network for image preprocessing and recognition (Figure 16e). Significant improvements in image recognition rate were achieved with ORRAM-based image preprocessing than without reprocessing, suggesting the critical role of ORRAM devices (Figure 16f). In addition, a hybrid MoS₂/perylene-3,4,9,10-tetracarboxylic dianhydride heterojunction synaptic transistor was fabricated by applying electrical and optical stimuli. Various basic plasticity functions of biological synapse were obtained, including IPSC, EPSC, PPD, PPF, SRDP, dynamic filtering, and long-term modulation of weight change.^[251]

Meanwhile, multicolor sensing beyond single wavelengths is highly demanded, which can also be achieved using three-terminal transistor optoelectronic memory devices. A heterostructure based on hybrid WSe₂/BN has rendered optoelectronic memory that can identify across multiple wavelengths (Figure 17a).^[257] The dynamic behavior of this optoelectronic memory included programming, readout, and erasing processes (Figure 17b–d). These processes are

controlled by modulating applied positive or negative gate (V_g) and the presence of light illumination. Upon photon excitation, the electric field drives electrons in the BN conduction band into the WSe₂, with localization of positive charges in the middle of the BN bandgap. After programming, the current at the positive gate (V_g > 0) is read without light irradiation. Then, erasing is carried out with both light illumination and a positive gate on WSe₂/BN devices. In this process, ionized positive defects in the BN are filled with electrons in the valence band upon photostimulation. The as-generated holes in the BN are driven by the external electric field toward WSe₂. The switching speed of WSe₂/BN memory was highlighted via completion of charge erasing within only 2 s. Moreover, a large switching ratio ($\approx 1.7 \times 10^4$) was achieved in this device. When the WSe₂/BN device was irradiated by light in the wavelength range from 750 nm (1.65 eV) to 410 nm (3.02 eV), the ON current in the electron-domination regime increased slowly after each programming process (Figure 17e). Meanwhile, highly distinct storage states were obtained at different irradiation wavelengths, highlighting the multiwavelength responsibility of the WSe₂/BN optoelectronic memory. A 3 × 9 array with a 27-pixel matrix based on WSe₂/BN image sensors was demonstrated for imaging letters by exposing them to different wavelengths of light at selected pixels (Figure 17f). Three different pixel groups showed three distinct storage states (5, 12, and 31 nA), which allow the device to be used as a color image sensor without a filter.

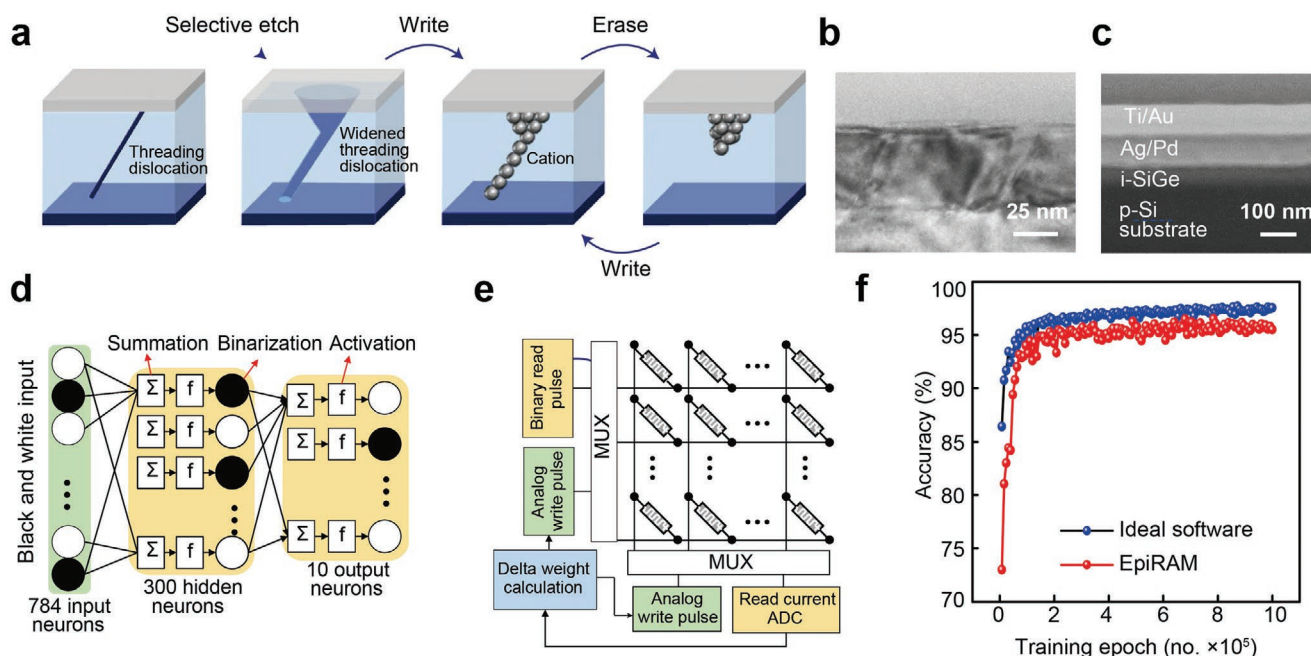


Figure 18. Supervised learning through SiGe dislocation-based devices. a) Schematic of the switching of SiGe epiRAM. b) Cross-sectional transmission electron microscopy imaging of 60 nm SiGe grown on a Si substrate. c) Cross-sectional scanning electron microscopy imaging of an epiRAM-based device. d) Schematic of a synapse composed of epiRAM-based crossbar arrays and circuits. e) Comparison of recognition accuracy between an ideal device and an epiRAM-based device. a–e) Reproduced with permission.^[270] Copyright 2018, The Authors, published by Springer Nature.

PCMs can also be used to build all-photonic synapses. All-photonic artificial synapses and neuromorphic systems are appealing because the charge-based wiring can be circumvented to enhance neuromorphic computing. PCMs provide an opportunity to achieve purely photonic memory due to their ability to undergo phase change between amorphous and crystalline states. Bhaskaran's group constructed on-chip memory devices comprising gallium lanthanum oxysulfide fibers. These devices operated at 13.4 pJ per switching with multilevel and multibit capabilities.^[20] Cheng et al. demonstrated STDP based on a photonic synapse with on-chip waveguide structures.^[24]

5. Networks for Neuromorphic Computing

Many artificial networks have been designed to achieve realistic neuromorphic computing, including ANNs and SNNs. In ANNs, the output remains static and mathematical optimization determines synaptic weight.^[168,174,175,258] On the other hand, SNNs are related to the history of neural activity, similar to the human brain's learning process.^[259–264] Generally, devices are designed using supervised, unsupervised, and reinforcement learning algorithms to simulate the human brain's neural network for image recognition, speech recognition, and robotics.^[21,265–269]

For supervised learning, input data are labeled while output data are desired results. SiGe single crystals epitaxially grown on Si-based resistors were used to conduct supervised learning ANN.^[270] Dislocation of SiGe for Ag filament growth in a confined 1D channel (Figure 18a–c) enabled long retention (45 h at 85 °C), large switching ratios ($\approx 10^4$), and long endurance

(10^6 cycles). In addition, a three-layer neural network with 28×28 pre-neurons, 300 hidden neurons, and 10 output neurons were utilized to simulate image recognition (Figure 18d,e). A synapse layer with epiRAM crossbar arrays and the peripheral circuit were shown in Figure 18f. An average learning accuracy of 95.1% was obtained by testing 10 000 images, comparable to the ideal device (97%).

The unlabeled input data of unsupervised learning make output data unpredictable. Ag nanoparticle-based diffusive memristors can serve as LIF neurons, in which the integration time could be tuned through silver migration alone or through interactions with circuit capacitance. The integration of these neurons and nonvolatile memristive synapses can be used as ANNs. An example of integrated chips comprising one-transistor–one-memristor (1T1R) synaptic arrays and diffusive memristor neurons was shown in Figure 19.^[271]

Reinforcement learning is represented by a device that achieves a learning target through maximum rewards in a given environment. In situ learning in a multilayer neural network implemented in a 128×64 Ta/HfO₂/Pt memristor array was realized with high efficiency (Figure 20).^[272] The network correctly classified 91.71% of 10 000 test images after training with 80 000 samples. Further simulations suggest that an improvement over 97% can be achieved using a larger (e.g., 1024×512) memristor array. The results imply that the accuracy of analog memristor neural networks approaches that of state-of-the-art digital CMOS systems, holding potential for further improvements in speed-energy efficiency.

Compared to ANNs, the information in SNNs is encoded within the time interval between binary spikes. Chen et al. constructed an SNN with a high switching ratio for image

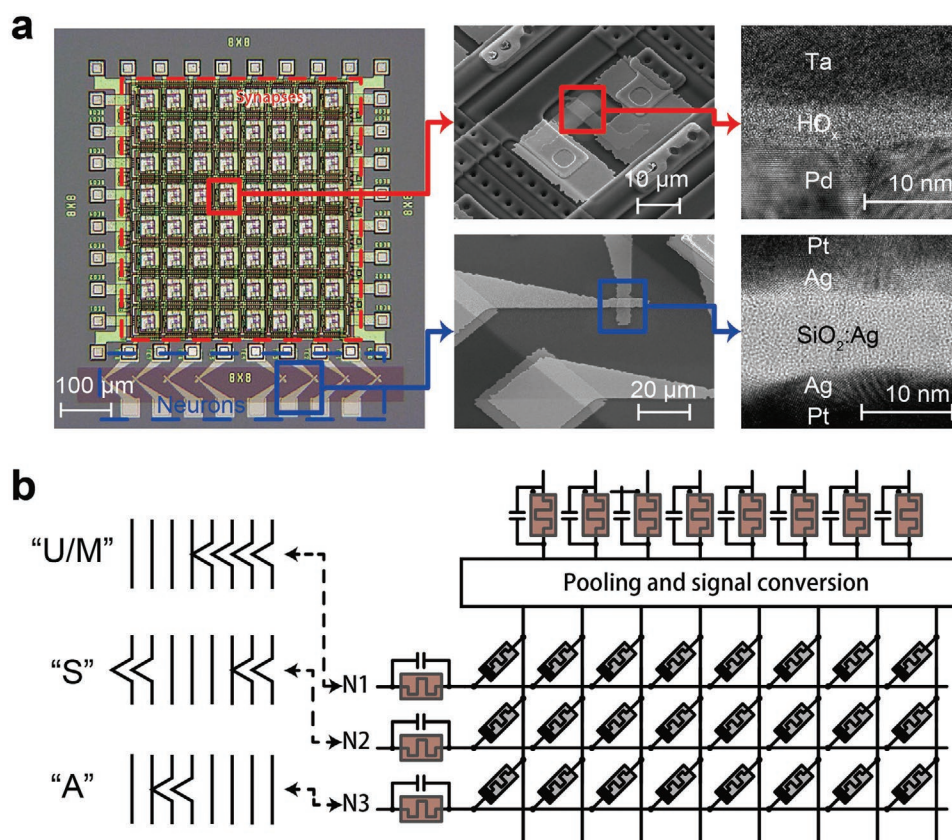


Figure 19. Unsupervised learning based on Pd/HfO_x/Ta drift and Pt/Ag/SiO_x/Ag/Ag/Pt diffusive memristors. a) Optical images of the neural network consisting of an 8 × 8 ITIR memristive synapse crossbar that interfaces with eight diffusive memristors as artificial neurons. b) Schematic of the 8 × 3 network with inputs based on the neurons' outputs shown in (a). a,b) Reproduced with permission.^[271] Copyright 2018, The Authors, published by Springer Nature.

recognition based on wafer-scale memristive crossbar arrays comprising h-BN 2D materials (Figure 21).^[273] The devices exhibited an ultralow energy consumption (20 f) per set), making them appealing as spiking neuromorphic hardware. In 2020, Li et al. demonstrated a new type of neural network comprising synapses, artificial dendrites, and soma (Figure 22).^[274] Compared with the system without the dendrites, the power consumption was reduced over 30 times, with improved recognition accuracy. Moreover, filtering and integrating functions were also realized using these devices.

6. Outlook

In the past decade, memristive devices of diverse materials have demonstrated the ability to mimic various biological synapses and neuronal behaviors, as summarized in this review. These devices exhibit a vast potential to simulate actions in biological neural networks and to better understand mechanisms of learning and memory. A number of significant hurdles remain to be overcome before this emerging technology brings many exciting advances in neuromorphic computing and artificial intelligence.^[275–278] The current challenge associated with memristors across dissimilar materials is the inability to fully mimic biological synapses. Most of the devices reported thus far can only demonstrate some functions of neurons and

synapses. To achieve a large-scale neural network that could mimic biological ones with increased accuracy, huge gaps of knowledge need to be eliminated in areas such as neurobiology, novel materials, device design, neural network optimization, and software algorithms.

Before discussing the deficiencies in our understanding of memristors, one major factor preventing the simulation of higher-order neural network behaviors is our lack of understanding of biological neural networks. Though much progress has been made on understanding how the human brain performs complex cognitive tasks, there is no doubt that further understanding of how the brain functions is needed. One example was demonstrated by Ma's group, who designed a memristive autapse connected to a neuron model that can mimic the autaptic current mediated by α -amino-3-hydroxy-5-methyl-4-isoxazole-propionic acid receptors for spiking and bursting modulation.^[279] This advance was made possible only due to the neurological phenomenon recently reported for biological cellular autapses.^[280]

An artificial neural network that closely mimics biological SNNs is one possible means to unlock the human brain's processing power. To achieve this, memristive devices mimicking synapses and neurons need to achieve the functions of their biological counterparts. One such potential device is the diffusive memristor that can simulate the temporal dynamics of biological synapses.^[72] However, the ability to tune artificial

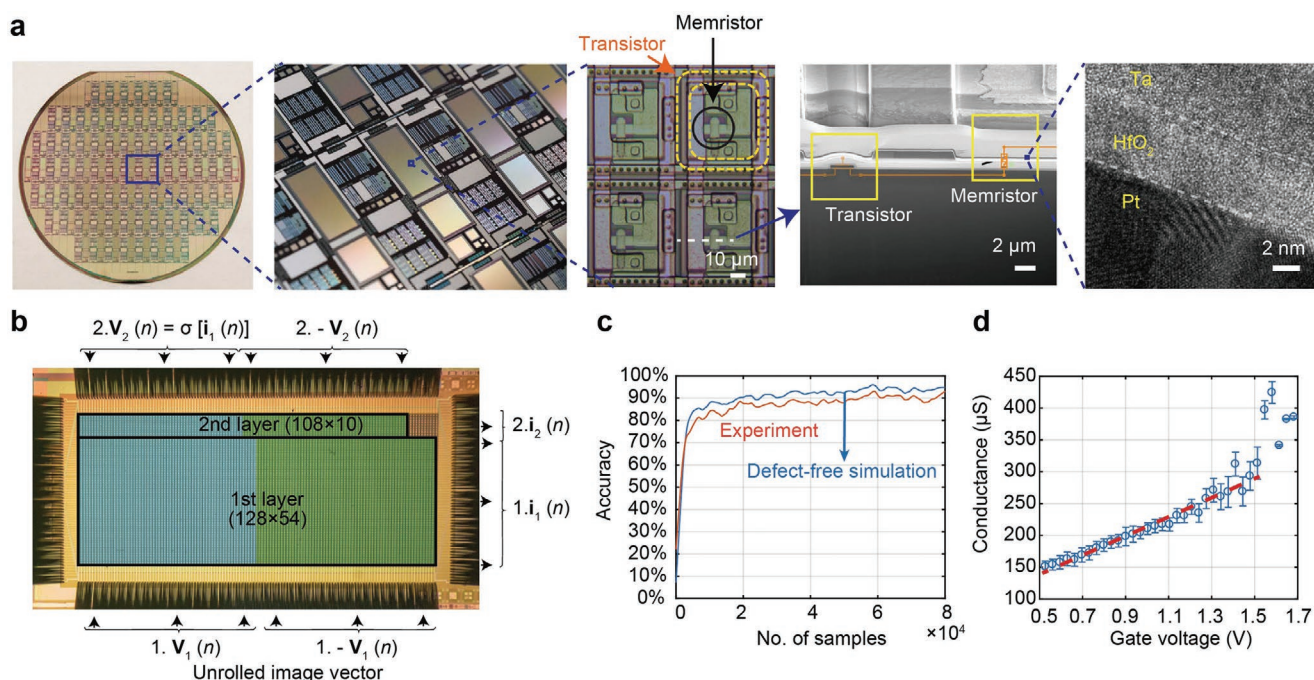


Figure 20. Memristive platform comprising 1T1R arrays for reinforcement learning. a) Photos of a HfO₂-based memristive device. b) Photo showing the integrated 128 × 64 array, as partitioned into two layers. c) Training-dependent minibatch accuracy. d) The $I_{\text{gate}}-V$ curves extracted from data collected during training. a–d) Reproduced under the terms of the CC-BY Creative Commons Attribution 4.0 International license (<https://creativecommons.org/licenses/by/4.0>).^[272] Copyright 2018, The Authors, published by Springer Nature.

devices in order to mimic their biological counterparts relies heavily on our fundamental understanding of their switching mechanisms. Despite the progress, switching mechanisms

for redox and PCMs continue to elude us due to their fast atomic rearrangement at the nanoscale. We need advanced in situ techniques to decode these atomic rearrangements,

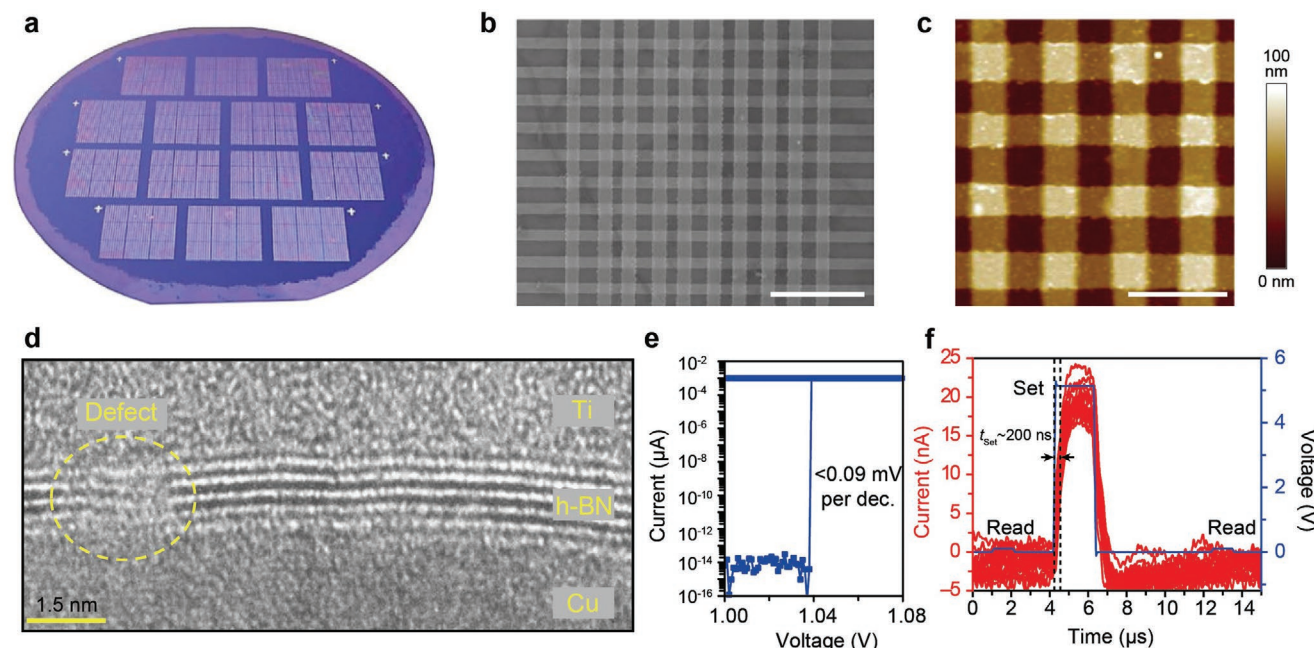


Figure 21. Spiking neural networks based on h-BN devices. a) Optical image of a 2-in. wafer with Au/h-BN/Au memristive crossbar arrays. b) Scanning electron microscopy imaging of a crossbar array containing 750 nm × 750 nm Ag/h-BN/Ag memristors. Scale bar: 4.5 μm . c) Atomic force microscopy imaging of the Ag/h-BN/Ag memristors. Scale bar: 2 μm . d) Cross-sectional transmission electron microscopy imaging of the h-BN. e) Threshold-type RS characteristic measured in an Ag/h-BN/Ag memristor. f) Statistical calculation of t_{SET} . a–f) Reproduced with permission.^[273] Copyright 2020, The Authors, published by Springer Nature.

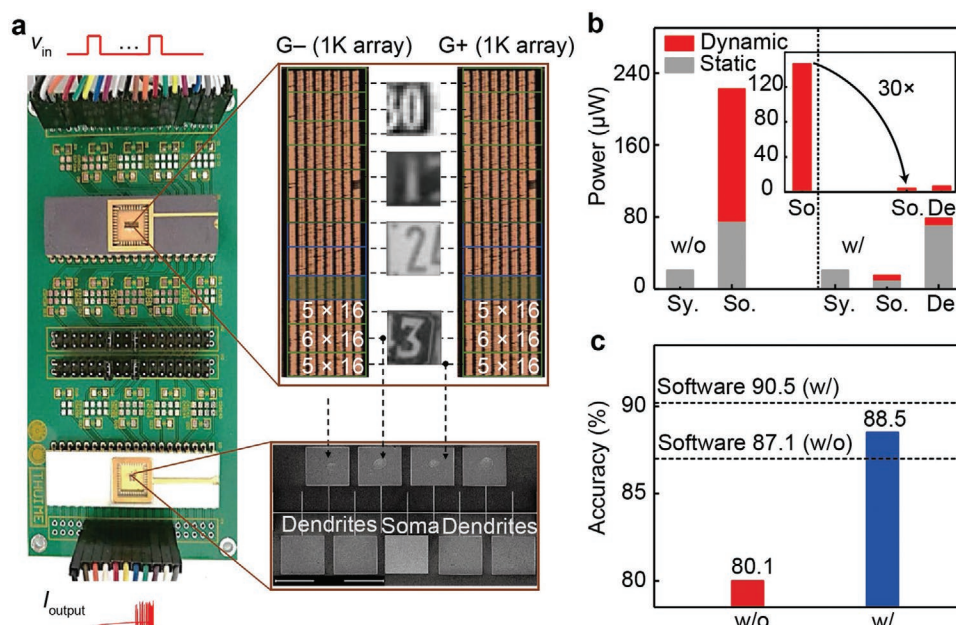


Figure 22. Single-layer neural networks with dendrites. a) Photograph of the crossbar arrays with soma, dendrites, and synapses. b) Comparison of the switching power with and without dendrites. c) Comparison of recognition accuracies with this neural network and the software baselines. a–c) Reproduced with permission.^[274] Copyright 2020, The Authors, published by Springer Nature.

such as atomic force microscopy, scanning tunneling microscopy, and electrostatic force microscopy. In addition, further improvements of specific device parameters are also needed for the successful realization of a neural network. For example, although memristors can achieve lower energy consumption than traditional silicon-based transistors, their energy consumption remains significantly higher than that of the human brain, which only uses about 10 to 20 W to perform a wide range of complicated cognitive tasks.^[281] Depending on the device switching mechanism, switching energy could be decreased by reducing energy barriers for switching, such as reducing device volume in phase-change devices or using topological insulators for spintronic systems^[282,283] However, reduction of energy consumption must be balanced well with device stability and switching speed, which would be negatively affected by lower energy barriers and driving power. Other device parameters that need to be improved include the reproducibility, stability, and reliability. To form a neural network composed of memristive neurons and synapses at the scale of human brain, high device fabrication reproducibility needs to be achieved. Cycle-to-cycle variations in individual device parameters would lead to reduced efficiency and accuracy of the entire neural network. Moreover, individual devices would be required to undergo huge numbers of read–write cycles. Therefore, the stability of devices used in the network should be maintained to prevent failures due to structural fatigue.^[284,285] Improvements in device endurance to repeated read–write cycles could be achieved using novel material compositions and device designs that reduce mechanical stress and diffusion. For neuromorphic computing, it is essential that memristive devices possess a large dynamic conductance range (G_{\max}/G_{\min}) to enable multiple accessible conductance states. Lastly, as we scale the neural network larger, the inherent

nonlinearity and asymmetry due to programming or sneak-path currents in crossbar-based applications results in increased energy and time expenditure in training due to loss in training accuracy. To tackle this problem, various novel device structures were developed such as pairing the memristors with transistors or capacitors,^[123,214,286,287] the introduction of dopants or modulation layers,^[288,289] and the use of programming^[46,290] to constantly correct for the nonlinearity and asymmetry.

While the above challenges are common among electronic memristors, memristive technologies that utilize different stimuli, such as magnetic fields or photons, also possess challenges. In this review, we summarized how spintronic memristor-based ANNs could be used in various applications. However, when compared to other memristors, MTJs have smaller resistance changes, especially in domain wall memristors with multiple intermediate states.^[291] This character makes the output reading relatively more difficult and especially vulnerable to thermal fluctuations when in the nanoscale. Therefore, research on novel spintronic materials or device designs that results in significant linear resistance change would enable more efficient MTJs. One such novel design was developed by Chen et al., who used an antiferromagnet to sandwich a ferromagnetic nanowire in an attempt to achieve viscous magnetization dynamics.^[292] Various synaptic behaviors such as STDP could be modeled by correlating the viscous dynamics and memristive behaviors. Another design by Sasaki's group utilized a three-terminal Co/Pd multilayer DW MTJ with inherent linear and symmetric conductance response upon applied pulses.^[293] By using optical lithography and Ar ion milling, they managed to achieve an element with 200 steps, allowing a broad, linear dynamic range of conductance to be modulated over 200 pulses. Furthermore, spintronic memristors provide solutions for realizing interconnectivity between

thousands of artificial synapses to a single neuron, mimicking the average biological synapse per neuron ratio.^[294] Multiple studies have demonstrated the ability of spintronic devices and systems to stack in a 3D manner for various applications.^[295,296] With further research in novel device materials and miniature device sizes, the development of a highly integrated 3D spintronics-based neural network system that could maintain high levels of interconnectivity through efficient communication in all three dimensions could potentially be realized.

Photonic memristors offer promising platforms as artificial synapses, especially with the advancement of optogenetics in recent years.^[297] However, higher-order plasticity has not been experimentally realized in all-photonic memory, even though various groups have demonstrated PCM-based synaptic plasticity with varying degrees of success. Fulfillment of higher-order plasticity has been challenging due to the lack of a detailed mechanistic understanding of resistive switching in associated devices. In addition, PCM-based neuro-inspired computing and in-memory computing still require improvements in various areas, including reduced stochasticity, less drift, faster speed, lower power consumption, and longer endurance. Further improvements in the performance of PCM synaptic devices require significant research efforts on device physics and comprehension of material properties in complex environments. Particular studies of photovoltaic and photogate effects on resistive switching would afford better control over device performance. In addition, most of the materials used in photonic memristors have broadband absorption in the UV region. However, photonic memristors generally exhibit weak sensitivity to the infrared region. To bridge this gap, organic dyes or lanthanide-doped nanoparticles with tunable absorption in the NIR-II region could be considered. Furthermore, the sharp absorption peaks of lanthanide ions can provide memristive responses with excellent wavelength selectivity. Moreover, mechanistic understanding, coupled with novel material design, may pave the way to further develop an all-photonic neural network.

In closing, considerable breakthroughs on multiple fronts such as biology, engineering, materials science, and computational science are still be needed to achieve an artificial neural network that can adequately mimic physical memory. Although the development of memristors is at its infancy, they provide alternative non-von Neumann solutions for neuromorphic computing because of their ease of tunability and flexible choices of external stimuli and working mechanisms. If the above difficulties can be addressed, we will be one step closer to mimicking the human brain for further advances in neuromorphic computing.

Acknowledgements

The Ministry of Education, Singapore (MOE2017-T2-2-110), Agency for Science, Technology and Research (A*STAR) under its AME program (Grant NO. A1883c0011 and A1983c0038), National Research Foundation, the Prime Minister's Office of Singapore under its NRF Investigatorship Programme (Award No. NRF-NRFI05-2019-0003), the King Abdullah University of Science and Technology (KAUST) Office of Sponsored Research (OSR) under Award No. OSR-2018-CRG7-3736, the National Natural Science Foundation of China (21771135, 21871071, 21774061, 61905121), and the Natural Science Foundation of Jiangsu Province, China (No. BK201907344) are acknowledged.

Conflict of Interest

The authors declare no conflict of interest.

Keywords

artificial synapses, memristive materials, neurons, synaptic plasticity

Received: September 22, 2020

Revised: December 3, 2020

Published online: April 9, 2021

- [1] G. E. Moore, *Proc. IEEE* **1998**, *86*, 82.
- [2] R. H. Dennard, F. H. Gaensslen, Y. U. Hwa-Nien, V. Leo Rideout, E. Bassous, A. R. Leblanc, *Proc. IEEE* **1999**, *87*, 668.
- [3] B. Rajendran, A. Sebastian, M. Schmuker, N. Srinivasa, E. Eleftheriou, *IEEE Signal Process. Mag.* **2019**, *36*, 97.
- [4] S. B. Furber, F. Galluppi, S. Temple, L. A. Plana, *Proc. IEEE* **2014**, *102*, 652.
- [5] P. A. Merolla, J. V. Arthur, R. Alvarez-Icaza, A. S. Cassidy, J. Sawada, F. Akopyan, B. L. Jackson, N. Imam, C. Guo, Y. Nakamura, B. Brezzo, I. Vo, S. K. Esser, R. Appuswamy, B. Taba, A. Amir, M. D. Flickner, W. P. Risk, R. Manohar, D. S. Modha, *Science* **2014**, *345*, 668.
- [6] M. Davies, N. Srinivasa, T.-H. Lin, G. Chinya, Y. Cao, S. H. Choday, G. Dimou, P. Joshi, N. Imam, S. Jain, *IEEE Micro* **2018**, *38*, 82.
- [7] J. Pei, L. Deng, S. Song, M. Zhao, Y. Zhang, S. Wu, G. Wang, Z. Zou, Z. Wu, W. He, *Nature* **2019**, *572*, 106.
- [8] K. Meier, in *2015 IEEE Int. Electron Devices Meeting (IEDM)*, IEEE, Piscataway, NJ, USA **2015**, <https://doi.org/10.1109/IEDM.2015.7409627>.
- [9] S. Moradi, N. Qiao, F. Stefanini, G. Indiveri, *IEEE Trans. Biomed. Circuits Syst.* **2017**, *12*, 106.
- [10] C. Frenkel, M. Lefebvre, J.-D. Legat, D. Bol, *IEEE Trans. Biomed. Circuits Syst.* **2018**, *13*, 145.
- [11] B. V. Benjamin, P. Gao, E. McQuinn, S. Choudhary, A. R. Chandrasekaran, J.-M. Bussat, R. Alvarez-Icaza, J. V. Arthur, P. A. Merolla, K. Boahen, *Proc. IEEE* **2014**, *102*, 699.
- [12] A. Neckar, S. Fok, B. V. Benjamin, T. C. Stewart, N. N. Oza, A. R. Voelker, C. Elias-Smith, R. Manohar, K. Boahen, *Proc. IEEE* **2018**, *107*, 144.
- [13] V. T. Pham, I. Groen, S. Manipatruni, W. Y. Choi, D. E. Nikonov, E. Sagasta, C. C. Lin, T. A. Gosavi, A. Marty, L. E. Hueso, I. A. Young, F. Casanova, *Nat. Electron.* **2020**, *3*, 309.
- [14] Z. Wang, H. Wu, G. W. Burr, C. S. Hwang, K. L. Wang, Q. Xia, J. J. Yang, *Nat. Rev. Mater.* **2020**, *5*, 173.
- [15] V. K. Sangwan, M. C. Hersam, *Nat. Nanotechnol.* **2020**, *15*, 517.
- [16] A. Sebastian, M. Le Gallo, R. Khaddam-Aljameh, E. Eleftheriou, *Nat. Nanotechnol.* **2020**, *15*, 529.
- [17] R. Yang, H. M. Huang, X. Guo, *Adv. Electron. Mater.* **2019**, *5*, 1900287.
- [18] K. Roy, A. Jaiswal, P. Panda, *Nature* **2019**, *575*, 607.
- [19] J. Grollier, D. Querlioz, K. Y. Camsari, K. Everschor-Sitte, S. Fukami, M. D. Stiles, *Nat. Electron.* **2020**, *3*, 360.
- [20] C. Rios, M. Stegmaier, P. Hosseini, D. Wang, T. Scherer, C. D. Wright, H. Bhaskaran, W. H. P. Pernice, *Nat. Photonics* **2015**, *9*, 725.
- [21] I. Chakraborty, G. Saha, A. Sengupta, K. Roy, *Sci. Rep.* **2018**, *8*, 12980.
- [22] C. Rios, N. Youngblood, Z. Cheng, M. Le Gallo, W. H. P. Pernice, C. D. Wright, A. Sebastian, H. Bhaskaran, *Sci. Adv.* **2019**, *5*, eaau5759.
- [23] W. H. P. Pernice, H. Bhaskaran, *Appl. Phys. Lett.* **2012**, *101*, 171101.

- [24] Z. Cheng, C. Ríos, W. H. P. Pernice, C. David Wright, H. Bhaskaran, *Sci. Adv.* **2017**, 3, e1700160.
- [25] M. Wuttig, H. Bhaskaran, T. Taubner, *Nat. Photonics* **2017**, 11, 465.
- [26] W. Zhang, R. Mazzarello, M. Wuttig, E. Ma, *Nat. Rev. Mater.* **2019**, 4, 150.
- [27] Y. Zhai, J. Q. Yang, Y. Zhou, J. Y. Mao, Y. Ren, V. A. L. Roy, S. T. Han, *Mater. Horiz.* **2018**, 5, 641.
- [28] Z. Wang, S. Zhang, L. Zhou, J. Mao, S. Han, Y. Ren, Q. Yang, Y. Wang, Y. Zhai, Y. Zhou, *Phys. Status Solidi RRL* **2019**, 13, 180064421.
- [29] S. Choi, J. Yang, G. Wang, *Adv. Mater.* **2020**, 32, 2004659.
- [30] I. K. Wood, *Neuroscience: Exploring the Brain*, Jones & Bartlett Learning, LLC, Boston, MA, USA **1996**.
- [31] M. Chistiakova, N. M. Bannon, M. Bazhenov, M. Volgushev, *Neuroscience* **2014**, 20, 483.
- [32] S. J. Martin, P. D. Grimwood, R. G. M. Morris, *Annu. Rev. Neurosci.* **2000**, 23, 649.
- [33] W. B. Matthews, *Br. Med. J.* **1976**, 2, 1202.
- [34] A. Kirkwood, M. F. Bear, *J. Neurosci.* **1994**, 14, 3404.
- [35] R. M. Mulkey, R. C. Malenka, *Neuron* **1992**, 9, 967.
- [36] P. P. Atluri, W. G. Regehr, *J. Neurosci.* **1996**, 16, 5661.
- [37] D. Debanne, N. C. Guérineau, B. H. Gähwiler, S. M. Thompson, *J. Physiol.* **1996**, 491, 163.
- [38] G. Q. Bi, M. M. Poo, *J. Neurosci.* **1998**, 18, 10464.
- [39] D. M. Blitz, K. A. Foster, W. G. Regehr, *Nat. Rev. Neurosci.* **2004**, 5, 630.
- [40] S. Choi, D. M. Lovinger, *Proc. Natl. Acad. Sci. USA* **1997**, 94, 2665.
- [41] R. S. Zucker, W. G. Regehr, *Annu. Rev. Physiol.* **2002**, 64, 355.
- [42] A. M. Thomson, *Trends Neurosci.* **2000**, 23, 305.
- [43] C. Du, F. Cai, M. A. Zidan, W. Ma, S. H. Lee, W. D. Lu, *Nat. Commun.* **2017**, 8, 2204.
- [44] R. Berdan, T. Prodromakis, A. Khat, I. Salaoru, C. Toumazou, F. Perez-Diaz, E. Vasilaki, in *2013 IEEE Int. Symp. on Circuits and Systems (ISCAS)*, IEEE, Piscataway, NJ, USA **2013**, pp. 425–428; <https://doi.org/10.1109/ISCAS.2013.6571871>.
- [45] J. Moon, W. Ma, J. H. Shin, F. Cai, C. Du, S. H. Lee, W. D. Lu, *Nat. Electron.* **2019**, 2, 480.
- [46] C. Li, M. Hu, Y. Li, H. Jiang, N. Ge, E. Montgomery, J. Zhang, W. Song, N. Dávila, C. E. Graves, Z. Li, J. P. Strachan, P. Lin, Z. Wang, M. Barnell, Q. Wu, R. S. Williams, J. J. Yang, Q. Xia, *Nat. Electron.* **2018**, 1, 52.
- [47] X. Ji, X. Zhao, M. C. Tan, R. Zhao, *Adv. Intell. Syst.* **2020**, 2, 1900118.
- [48] S. Song, K. D. Miller, L. F. Abbott, *Nat. Neurosci.* **2000**, 3, 919.
- [49] Y. Dan, M. M. Poo, *Physiol. Rev.* **2006**, 86, 1033.
- [50] T. Serrano-Gotarredona, T. Masquelier, T. Prodromakis, G. Indiveri, B. Linares-Barranco, *Front. Neurosci.* **2013**, 7, 2.
- [51] D. A. Sousa, *How the Brain Learns (4th ed.)*, Corwin Press, Thousand Oaks, CA, USA **2011**.
- [52] W. C. Abraham, *Nat. Rev. Neurosci.* **2008**, 9, 387.
- [53] M. Chistiakova, N. M. Bannon, M. Bazhenov, M. Volgushev, *Physiol. Behav.* **2016**, 176, 139.
- [54] W. Gerstner, R. Naud, *Science* **2009**, 326, 379.
- [55] E. N. Miranda, *Acta Biotheor.* **1997**, 45, 171.
- [56] L. F. Abbott, *Brain Res. Bull.* **1999**, 50, 303.
- [57] R. Llinas, C. A. Terzuolo, *J. Neurophysiol.* **1965**, 28, 413.
- [58] A. L. Hodgkin, A. F. Huxley, *J. Physiol.* **1952**, 117, 500.
- [59] N. R. Carlson, *Psychology: The Science Behavior*, Pearson, London, UK **2008**.
- [60] Y. Lian, S. Theodoridis, G. Yuan, S. Pavan, *IEEE Trans. Circuits Syst. I Regul. Pap.* **2014**, 61, 1301.
- [61] L. Chua, *IEEE Trans. Circuit Theory* **1971**, 18, 507.
- [62] D. B. Strukov, G. S. Snider, D. R. Stewart, R. S. Williams, *Nature* **2008**, 453, 80.
- [63] J. Y. Ye, Y. Q. Li, J. Gao, H. Y. Peng, S. X. Wu, T. Wu, *Appl. Phys. Lett.* **2010**, 97, 132108.
- [64] S. Wu, X. Luo, S. Turner, H. Peng, W. Lin, J. Ding, A. David, B. Wang, G. Van Tendeloo, J. Wang, T. Wu, *Phys. Rev. X* **2014**, 3, 41027.
- [65] K. Szot, W. Speier, G. Bihlmayer, R. Waser, *Nat. Mater.* **2006**, 5, 312.
- [66] J. P. Strachan, M. D. Pickett, J. J. Yang, S. Aloni, A. L. David Kilcoyne, G. Medeiros-Ribeiro, R. S. Williams, *Adv. Mater.* **2010**, 22, 3573.
- [67] C. Baeumer, C. Schmitz, A. Marchewka, D. N. Mueller, R. Valenta, J. Hackl, N. Raab, S. P. Rogers, M. I. Khan, S. Nemsak, *Nat. Commun.* **2016**, 7, 12398.
- [68] S. Kumar, C. E. Graves, J. P. Strachan, E. M. Grafals, A. L. D. Kilcoyne, T. Tyliczszak, J. N. Weker, Y. Nishi, R. S. Williams, *Adv. Mater.* **2016**, 28, 2772.
- [69] G.-S. Park, Y. B. Kim, S. Y. Park, X. S. Li, S. Heo, M.-J. Lee, M. Chang, J. H. Kwon, M. Kim, U.-I. Chung, *Nat. Commun.* **2013**, 4, 2382.
- [70] Y. Yang, P. Gao, L. Li, X. Pan, S. Tappertzhofen, S. Choi, R. Waser, I. Valov, W. D. Lu, *Nat. Commun.* **2014**, 5, 4232.
- [71] Y. Hirose, H. Hirose, *J. Appl. Phys.* **1976**, 47, 2767.
- [72] Z. Wang, S. Joshi, S. E. Savel'ev, H. Jiang, R. Midya, P. Lin, M. Hu, N. Ge, J. P. Strachan, Z. Li, Q. Wu, M. Barnell, G. L. Li, H. L. Xin, R. S. Williams, Q. Xia, J. J. Yang, *Nat. Mater.* **2017**, 16, 101.
- [73] N. Onofrio, D. Guzman, A. Strachan, *Nat. Mater.* **2015**, 14, 440.
- [74] A. Wedig, M. Luebben, D.-Y. Cho, M. Moors, K. Skaja, V. Rana, T. Hasegawa, K. K. Adeplali, B. Yildiz, R. Waser, *Nat. Nanotechnol.* **2016**, 11, 67.
- [75] D. Kuzum, R. G. D. Jeyasingh, B. Lee, H.-S. P. Wong, *Nano Lett.* **2012**, 12, 2179.
- [76] M. Wuttig, N. Yamada, *Nat. Mater.* **2007**, 6, 824.
- [77] H.-S. P. Wong, S. Raoux, S. Kim, J. Liang, J. P. Reifenberg, B. Rajendran, M. Asheghi, K. E. Goodson, *Proc. IEEE* **2010**, 98, 2201.
- [78] S. R. Ovshinsky, *Phys. Rev. Lett.* **1968**, 21, 1450.
- [79] J.-J. Wang, Y.-Z. Xu, R. Mazzarello, M. Wuttig, W. Zhang, *Materials* **2017**, 10, 862.
- [80] K. Shportko, S. Kremers, M. Woda, D. Lencer, J. Robertson, M. Wuttig, *Nat. Mater.* **2008**, 7, 653.
- [81] S. Gabardi, S. Caravati, G. C. Sossio, J. Behler, M. Bernasconi, *Phys. Rev. B* **2015**, 92, 54201.
- [82] J. Y. Raty, W. Zhang, J. Luckas, C. Chen, R. Mazzarello, C. Bichara, M. Wuttig, *Nat. Commun.* **2015**, 6, 7467.
- [83] W. Zhang, V. L. Deringer, R. Dronskowski, R. Mazzarello, E. Ma, M. Wuttig, *MRS Bull.* **2015**, 40, 856.
- [84] W. Zhang, A. Thiess, P. Zalden, R. Zeller, P. H. Dederichs, J.-Y. Raty, M. Wuttig, S. Blügel, R. Mazzarello, *Nat. Mater.* **2012**, 11, 952.
- [85] T. Siegrist, P. Jost, H. Volker, M. Woda, P. Merkelbach, C. Schlockermann, M. Wuttig, *Nat. Mater.* **2011**, 10, 202.
- [86] M. Salinga, E. Carria, A. Kaldenbach, M. Bornhöft, J. Benke, J. Mayer, M. Wuttig, *Nat. Commun.* **2013**, 4, 2371.
- [87] A. Sebastian, M. Le Gallo, D. Krebs, *Nat. Commun.* **2014**, 5, 4314.
- [88] X. Zhang, H. Xie, Z. Liu, C. Tan, Z. Luo, H. Li, J. Lin, L. Sun, W. Chen, Z. Xu, L. Xie, W. Huang, H. Zhang, *Angew. Chem., Int. Ed.* **2015**, 54, 3653.
- [89] J. Ouyang, C. W. Chu, C. R. Szmanda, L. Ma, Y. Yang, *Nat. Mater.* **2004**, 3, 918.
- [90] D. J. Seong, M. Jo, D. Lee, H. Hwang, *Electrochem. Solid-State Lett.* **2007**, 10, H168.
- [91] D. S. Shang, L. Shi, J. R. Sun, B. G. Shen, F. Zhuge, R. W. Li, Y. G. Zhao, *Appl. Phys. Lett.* **2010**, 96, 072103.
- [92] J. G. Simmons, R. R. Verderber, *Proc. R. Soc. London, Ser. A* **1967**, 301, 77.
- [93] S. Das, A. J. Pal, *Appl. Phys. Lett.* **2000**, 76, 1770.
- [94] H. S. Majumdar, A. Bandyopadhyay, A. Bolognesi, A. J. Pal, *J. Appl. Phys.* **2002**, 91, 2433.
- [95] C. Wu, F. Li, T. Guo, *Appl. Phys. Lett.* **2014**, 104, 183105.
- [96] Y. Wang, J. Yang, Z. Wang, J. Chen, Q. Yang, Z. Lv, Y. Zhou, Y. Zhai, Z. Li, S. T. Han, *Small* **2019**, 15, 1805431.
- [97] P. Cui, S. Seo, J. Lee, L. Wang, E. Lee, M. Min, H. Lee, *ACS Nano* **2011**, 5, 6826.

- [98] Y. Wang, Z. Lv, Q. Liao, H. Shan, J. Chen, Y. Zhou, L. Zhou, X. Chen, V. A. L. Roy, Z. Wang, Z. Xu, Y. Zeng, S. Han, *Adv. Mater.* **2018**, *30*, 1800327.
- [99] L. Hu, J. Yuan, Y. Ren, Y. Wang, J. Yang, Y. Zhou, Y. Zeng, S. Han, S. Ruan, *Adv. Mater.* **2018**, *30*, 1801232.
- [100] P. C. Ooi, J. Lin, T. W. Kim, F. Li, *Org. Electron.* **2016**, *38*, 379.
- [101] S. Paul, A. Kanwal, M. Chhowalla, *Nanotechnology* **2005**, *17*, 145.
- [102] Y. Ji, D. F. Zeigler, D. S. Lee, H. Choi, A. K.-Y. Jen, H. C. Ko, T.-W. Kim, *Nat. Commun.* **2013**, *4*, 2707.
- [103] H.-T. Lin, Z. Pei, Y.-J. Chan, *IEEE Electron Device Lett.* **2007**, *28*, 569.
- [104] H. Ling, M. Yi, M. Nagai, L. Xie, L. Wang, B. Hu, W. Huang, *Adv. Mater.* **2017**, *29*, 1701333.
- [105] G. Niu, P. Calka, M. Auf der Maur, F. Santoni, S. Guha, M. Fraschke, P. Hamoumou, B. Gautier, E. Perez, C. Walczyk, C. Wenger, A. Di Carlo, L. Alf, T. Schroeder, *Sci. Rep.* **2016**, *6*, 25757.
- [106] S. Song, B. Cho, T. W. Kim, Y. Ji, M. Jo, G. Wang, M. Choe, Y. H. Kahng, H. Hwang, T. Lee, *Adv. Mater.* **2010**, *22*, 5048.
- [107] S. Song, J. Jang, Y. Ji, S. Park, T.-W. Kim, Y. Song, M.-H. Yoon, H. C. Ko, G.-Y. Jung, T. Lee, *Org. Electron.* **2013**, *14*, 2087.
- [108] C. Diorio, P. Hasler, A. Minch, C. A. Mead, *IEEE Trans. Electron Devices* **1996**, *43*, 1972.
- [109] Y. Yu, Q. Ma, H. Ling, W. Li, R. Ju, L. Bian, N. Shi, Y. Qian, M. Yi, L. Xie, W. Huang, *Adv. Funct. Mater.* **2019**, *29*, 1904602.
- [110] H. Ling, D. A. Koutsouras, S. Kazemzadeh, Y. van de Burgt, F. Yan, P. Gkoupidenis, *Appl. Phys. Rev.* **2020**, *7*, 011307.
- [111] N. Wang, A. Yang, Y. Fu, Y. Li, F. Yan, *Acc. Chem. Res.* **2019**, *52*, 277.
- [112] Y. He, Y. Yang, S. Nie, R. Liu, Q. Wan, *J. Mater. Chem. C* **2018**, *6*, 5336.
- [113] H. Ling, N. Wang, A. Yang, Y. Liu, J. Song, F. Yan, *Adv. Mater. Technol.* **2019**, *4*, 1900471.
- [114] P. Gkoupidenis, D. A. Koutsouras, G. G. Malliaras, *Nat. Commun.* **2017**, *8*, 15448.
- [115] Y. He, S. Nie, R. Liu, S. Jiang, Y. Shi, Q. Wan, *Adv. Mater.* **2019**, *31*, 1900903.
- [116] K. Wang, H. Ling, Y. Bao, M. Yang, Y. Yang, M. Hussain, H. Wang, L. Zhang, L. Xie, M. Yi, *Adv. Mater.* **2018**, *30*, 1800595.
- [117] Y. Wang, J. Yang, W. Ye, D. She, J. Chen, Z. Lv, V. A. L. Roy, H. Li, K. Zhou, Q. Yang, *Adv. Electron. Mater.* **2020**, *6*, 1900765.
- [118] Y. Ren, J. Yang, L. Zhou, J. Mao, S. Zhang, Y. Zhou, S. Han, *Adv. Funct. Mater.* **2018**, *28*, 1805599.
- [119] W. Li, F. Guo, H. Ling, H. Liu, M. Yi, P. Zhang, W. Wang, L. Xie, W. Huang, *Small* **2018**, *14*, 1701437.
- [120] Y. Yu, L. Bian, J. Chen, Q. Ma, Y. Li, H. Ling, Q. Feng, L. Xie, M. Yi, W. Huang, *Adv. Sci.* **2018**, *5*, 1800747.
- [121] H. Ling, J. Lin, M. Yi, B. Liu, W. Li, Z. Lin, L. Xie, Y. Bao, F. Guo, W. Huang, *ACS Appl. Mater. Interfaces* **2016**, *8*, 18969.
- [122] D. T. Duong, Y. Tuchman, P. Chakhranont, P. Cavassin, R. Colucci, T. F. Jaramillo, A. Salleo, G. C. Faria, *Adv. Electron. Mater.* **2018**, *4*, 1800090.
- [123] Y. Van De Burgt, E. Lubberman, E. J. Fuller, S. T. Keene, G. C. Faria, S. Agarwal, M. J. Marinella, A. Alec Talin, A. Salleo, *Nat. Mater.* **2017**, *16*, 414.
- [124] C. Qian, J. Sun, L. Kong, G. Gou, J. Yang, J. He, Y. Gao, Q. Wan, *ACS Appl. Mater. Interfaces* **2016**, *8*, 26169.
- [125] Y. Van De Burgt, A. Melianas, S. T. Keene, G. Malliaras, A. Salleo, *Nat. Electron.* **2018**, *1*, 386.
- [126] W. Xu, S.-Y. Min, H. Hwang, T.-W. Lee, *Sci. Adv.* **2016**, *2*, e1501326.
- [127] Y. Kim, A. Chortos, W. Xu, Y. Liu, J. Y. Oh, S. Niu, J. Liu, R. Pfattner, Z. Bao, T. Lee, *Science* **2018**, *360*, 998.
- [128] Y. Lee, J. Y. Oh, W. Xu, O. Kim, T. R. Kim, J. Kang, Y. Kim, D. Son, J. B.-H. Tok, M. J. Park, *Sci. Adv.* **2018**, *4*, eaat7387.
- [129] H. Y. Choi, C. Wu, C. H. Bok, T. W. Kim, *NPG Asia Mater* **2017**, *9*, e413.
- [130] F. Alibart, S. Pleutin, D. Guérin, C. Novembre, S. Lenfant, K. Lmimouni, C. Gamrat, D. Vuillaume, *Adv. Funct. Mater.* **2010**, *20*, 330.
- [131] F. Yu, J. C. Cai, L. Q. Zhu, M. Sheikhi, Y. H. Zeng, W. Guo, Z. Y. Ren, H. Xiao, J. C. Ye, C. H. Lin, A. B. Wong, T. Wu, *ACS Appl. Mater. Interfaces* **2020**, *12*, 26258.
- [132] M.-K. Kim, J.-S. Lee, *Nano Lett.* **2019**, *19*, 2044.
- [133] S. Yu, *Proc. IEEE* **2018**, *106*, 260.
- [134] E. Yurchuk, J. Müller, J. Paul, T. Schlösser, D. Martin, R. Hoffmann, S. Müller, S. Slesazek, U. Schröder, R. Boschke, *IEEE Trans. Electron Devices* **2014**, *61*, 3699.
- [135] J. J. Yang, M. D. Pickett, X. Li, D. A. A. Ohlberg, D. R. Stewart, R. S. Williams, *Nat. Nanotechnol.* **2008**, *3*, 429.
- [136] D. B. Strukov, R. S. Williams, *Appl. Phys. A* **2009**, *94*, 515.
- [137] X. Guan, S. Yu, H.-S. P. Wong, *IEEE Electron Device Lett.* **2012**, *33*, 1405.
- [138] Z. Jiang, Y. Wu, S. Yu, L. Yang, K. Song, Z. Karim, H.-S. P. Wong, *IEEE Trans. Electron Devices* **2016**, *63*, 1884.
- [139] U. Russo, D. Ielmini, C. Cagli, A. L. Lacaita, *IEEE Trans. Electron Devices* **2009**, *56*, 186.
- [140] F. Nardi, S. Larentis, S. Balatti, D. C. Gilmer, D. Ielmini, *IEEE Trans. Electron Devices* **2012**, *59*, 2461.
- [141] Y. Zhang, X. Wang, Y. Li, E. G. Friedman, *IEEE Trans. Circuits Syst. II Express Briefs* **2016**, *64*, 767.
- [142] A. M. Stoneham, *Appl. Surf. Sci.* **1983**, *14*, 249.
- [143] X. Wang, Y. Chen, H. Xi, H. Li, D. Dimitrov, *IEEE Electron Device Lett.* **2009**, *30*, 294.
- [144] D. C. Ralph, Y.-T. Cui, L. Q. Liu, T. Moriyama, C. Wang, R. A. Buhrman, *Philos. Trans. R. Soc., A* **2011**, *369*, 3617.
- [145] L. Liu, C.-F. Pai, Y. Li, H. W. Tseng, D. C. Ralph, R. A. Buhrman, *Science* **2012**, *336*, 555.
- [146] G. Srinivasan, A. Sengupta, K. Roy, *Sci. Rep.* **2016**, *6*, 29545.
- [147] M. Sharad, D. Fan, K. Roy, *J. Appl. Phys.* **2013**, *114*, 234906.
- [148] Q. Cao, W. Lü, X. R. Wang, X. Guan, L. Wang, S. Yan, T. Wu, X. Wang, *ACS Appl. Mater. Interfaces* **2020**, *12*, 42449.
- [149] J. Cai, B. Fang, C. Wang, Z. Zeng, *Appl. Phys. Lett.* **2017**, *111*, 182410.
- [150] A. Chanthbouala, R. Matsumoto, J. Grollier, V. Cros, A. Anane, A. Fert, A. V. Khvalkovskiy, K. A. Zvezdin, K. Nishimura, Y. Nagamine, H. Maehara, K. Tsunekawa, A. Fukushima, S. Yuasa, *Nat. Phys.* **2011**, *7*, 626.
- [151] P. J. Metaxas, J. Sampaio, A. Chanthbouala, R. Matsumoto, A. Anane, A. Fert, K. A. Zvezdin, K. Yakushiji, H. Kubota, A. Fukushima, S. Yuasa, K. Nishimura, Y. Nagamine, H. Maehara, K. Tsunekawa, V. Cros, J. Grollier, *Sci. Rep.* **2013**, *3*, 1829.
- [152] Y. Shim, A. Sengupta, K. Roy, in *2016 53rd ACM/EDAC/IEEE Design Automation Conf. (DAC)*, IEEE, Piscataway, NJ, USA **2016**, <https://doi.org/10.1145/2897937.2898042>.
- [153] J. Y. Mao, L. Zhou, X. Zhu, Y. Zhou, S. T. Han, *Adv. Opt. Mater.* **2019**, *7*, 1900766.
- [154] H. J. Caulfield, S. Dolev, *Nat. Photonics* **2010**, *4*, 261.
- [155] A. Pirovano, K. Schuegraf, *Nat. Nanotechnol.* **2010**, *5*, 177.
- [156] E. Kuramochi, K. Nozaki, A. Shinya, K. Takeda, T. Sato, S. Matsuo, H. Taniyama, H. Sumikura, M. Notomi, *Nat. Photonics* **2014**, *8*, 474.
- [157] M. T. Hill, H. J. S. Dorren, T. De Vries, X. J. M. Leijtens, J. H. Den Besten, B. Smalbrugge, Y.-S. Oei, H. Binsma, G.-D. Khoe, M. K. Smit, *Nature* **2004**, *432*, 206.
- [158] S. Zimmermann, A. Wixforth, J. P. Kotthaus, W. Wegscheider, M. Bichler, *Science* **1999**, *283*, 1292.
- [159] T. Tanabe, M. Notomi, E. Kuramochi, A. Shinya, H. Taniyama, *Nat. Photonics* **2007**, *1*, 49.
- [160] L. Liu, R. Kumar, K. Huybrechts, T. Spuesens, G. Roelkens, E. J. Geluk, T. De Vries, P. Regreny, D. Van Thourhout, R. Baets, G. Morthier, *Nat. Photonics* **2010**, *4*, 182.

- [161] Y. Du, H. Pan, S. Wang, T. Wu, Y. P. Feng, J. Pan, A. T. S. Wee, *ACS Nano* **2012**, 6, 2517.
- [162] H. Y. Peng, Y. F. Li, W. N. Lin, Y. Z. Wang, X. Y. Gao, T. Wu, *Sci. Rep.* **2012**, 2, 442.
- [163] L. Chen, Z.-Y. He, T.-Y. Wang, Y.-W. Dai, H. Zhu, Q.-Q. Sun, D. W. Zhang, *Electronics* **2018**, 7, 80.
- [164] S. Yu, Y. Wu, R. Jeyasingh, D. Kuzum, H. S. P. Wong, *IEEE Trans. Electron Devices* **2011**, 58, 2729.
- [165] Z. Q. Wang, H. Y. Xu, X. H. Li, H. Yu, Y. C. Liu, X. J. Zhu, *Adv. Funct. Mater.* **2012**, 22, 2759.
- [166] R. Jiang, P. Ma, Z. Han, X. Du, *Sci. Rep.* **2017**, 7, 9354.
- [167] C. Chen, C. Song, J. Yang, F. Zeng, F. Pan, *Appl. Phys. Lett.* **2012**, 100, 253509.
- [168] J. Woo, D. Lee, Y. Koo, H. Hwang, *Microelectron. Eng.* **2017**, 182, 42.
- [169] C. Wang, W. He, Y. Tong, R. Zhao, *Sci. Rep.* **2016**, 6, 22970.
- [170] M. Hansen, M. Ziegler, L. Kolberg, R. Soni, S. Dirkmann, T. Mussenbrock, H. Kohlstedt, *Sci. Rep.* **2015**, 5, 13753.
- [171] M. D. Pickett, G. Medeiros-ribeiro, R. S. Williams, *Nat. Mater.* **2012**, 12, 114.
- [172] Z. Wang, M. Yin, T. Zhang, Y. Cai, Y. Wang, Y. Yang, R. Huang, *Nanoscale* **2016**, 8, 14015.
- [173] S. Kim, C. Du, P. Sheridan, W. Ma, S. Choi, W. D. Lu, *Nano Lett.* **2015**, 15, 2203.
- [174] X. Zhang, W. Wang, Q. Liu, X. Zhao, J. Wei, R. Cao, Z. Yao, X. Zhu, F. Zhang, H. Lv, *IEEE Electron Device Lett.* **2017**, 39, 308.
- [175] J. Lin, Annadi, S. Sonde, C. Chen, L. Stan, K. V. L. V. Achari, S. Ramanathan, S. Guha, in *2016 IEEE Int. Electron Devices Meeting (IEDM)*, IEEE, Piscataway, NJ, USA **2016**, pp. 34–35, <https://doi.org/10.1109/IEDM.2016.7838541>.
- [176] W. Yi, K. K. Tsang, S. K. Lam, X. Bai, J. A. Crowell, E. A. Flores, *Nat. Commun.* **2018**, 9, 4661.
- [177] Y. Ji, Y. Yang, S.-K. Lee, G. Ruan, T.-W. Kim, H. Fei, S.-H. Lee, D.-Y. Kim, J. Yoon, J. M. Tour, *ACS Nano* **2016**, 10, 7598.
- [178] Z. Wang, T. Zeng, Y. Ren, Y. Lin, H. Xu, X. Zhao, Y. Liu, D. Ielmini, *Nat. Commun.* **2020**, 11, 1510.
- [179] H. Huang, R. Yang, Z. Tan, H. He, W. Zhou, J. Xiong, X. Guo, *Adv. Mater.* **2019**, 31, 1803849.
- [180] C. Liu, H. Chen, S. Wang, Q. Liu, Y. G. Jiang, D. W. Zhang, M. Liu, P. Zhou, *Nat. Nanotechnol.* **2020**, 15, 545.
- [181] S. Wang, D. W. Zhang, P. Zhou, *Sci. Bull.* **2019**, 64, 1056.
- [182] A. A. Bessonov, M. N. Kirikova, D. I. Petukhov, M. Allen, T. Ryhänen, M. J. A. Bailey, *Nat. Mater.* **2015**, 14, 199.
- [183] R. Ge, X. Wu, M. Kim, J. Shi, S. Sonde, L. Tao, Y. Zhang, J. C. Lee, D. Akinwande, *Nano Lett.* **2018**, 18, 434.
- [184] M. Kim, R. Ge, X. Wu, X. Lan, J. Tice, J. C. Lee, D. Akinwande, *Nat. Commun.* **2018**, 9, 2524.
- [185] M. Wang, S. Cai, C. Pan, C. Wang, X. Lian, Y. Zhuo, K. Xu, T. Cao, X. Pan, B. Wang, S.-J. Liang, J. J. Yang, P. Wang, F. Miao, *Nat. Electron.* **2018**, 1, 130.
- [186] R. Xu, H. Jang, M.-H. Lee, D. Amanov, Y. Cho, H. Kim, S. Park, H.-J. Shin, D. Ham, *Nano Lett.* **2019**, 19, 2411.
- [187] J. Kang, V. K. Sangwan, J. D. Wood, M. C. Hersam, *Acc. Chem. Res.* **2017**, 50, 943.
- [188] C. Tan, Z. Liu, W. Huang, H. Zhang, *Chem. Soc. Rev.* **2015**, 44, 2615.
- [189] Z. Zhou, D. Yu, X. Ma, C. Zheng, H. Cheng, C. Zheng, in *2017 12th IEEE Conf. on Industrial Electronics and Applications (ICIEA)*, IEEE, Piscataway, NJ, USA **2017**, pp. 813–817, <https://doi.org/10.1109/ICIEA.2017.8282951>.
- [190] V. K. Sangwan, D. Jariwala, I. S. Kim, K.-S. Chen, T. J. Marks, L. J. Lauhon, M. C. Hersam, *Nat. Nanotechnol.* **2015**, 10, 403.
- [191] V. K. Sangwan, H. S. Lee, H. Bergeron, I. Balla, M. E. Beck, K. S. Chen, M. C. Hersam, *Nature* **2018**, 554, 500.
- [192] M. C. Sangwan, V. K. Lee, H.-S. Hersam, in *2017 IEEE Int. Electron Devices Meeting (IEDM)*, IEEE, Piscataway, NJ, USA **2017**, <https://doi.org/10.1109/IEDM.2017.8268330>.
- [193] N. K. Upadhyay, H. Jiang, Z. Wang, S. Asapu, Q. Xia, J. Joshua Yang, *Adv. Mater. Technol.* **2019**, 4, 1800589.
- [194] J. Guo, L. Wang, Y. Liu, Z. Zhao, E. Zhu, Z. Lin, P. Wang, C. Jia, S. Yang, S. J. Lee, W. Huang, Y. Huang, X. Duan, *Matter* **2020**, 2, 965.
- [195] L. Wang, W. Liao, S. L. Wong, Z. G. Yu, S. Li, Y. Lim, X. Feng, W. C. Tan, X. Huang, L. Chen, L. Liu, J. Chen, X. Gong, C. Zhu, *Adv. Funct. Mater.* **2019**, 29, 1901106.
- [196] X. Zhu, D. Li, X. Liang, W. D. Lu, *Nat. Mater.* **2019**, 18, 141.
- [197] L. Q. Zhu, C. J. Wan, L. Q. Guo, Y. Shi, Q. Wan, *Nat. Commun.* **2014**, 5, 3158.
- [198] Y. Yang, B. Chen, W. D. Lu, *Adv. Mater.* **2015**, 27, 7720.
- [199] L. Sun, Y. Zhang, G. Hwang, J. Jiang, D. Kim, Y. A. Eshete, R. Zhao, H. Yang, *Nano Lett.* **2018**, 18, 3229.
- [200] S. Das, A. Dodda, S. Das, *Nat. Commun.* **2019**, 10, 3450.
- [201] H. Tian, W. Mi, X.-F. Wang, H. Zhao, Q.-Y. Xie, C. Li, Y.-X. Li, Y. Yang, T.-L. Ren, *Nano Lett.* **2015**, 15, 8013.
- [202] H. Tian, W. Mi, H. Zhao, M. A. Mohammad, Y. Yang, P.-W. Chiu, T.-L. Ren, *Nanoscale* **2017**, 9, 9275.
- [203] Y. Yang, J. Wen, L. Guo, X. Wan, P. Du, P. Feng, Y. Shi, Q. Wan, *ACS Appl. Mater. Interfaces* **2016**, 8, 30281.
- [204] C. J. Wan, L. Q. Zhu, Y. H. Liu, P. Feng, Z. P. Liu, H. L. Cao, P. Xiao, Y. Shi, Q. Wan, *Adv. Mater.* **2016**, 28, 3557.
- [205] Y.-C. Chen, S.-T. Hu, C.-Y. Lin, B. Fowler, H.-C. Huang, C.-C. Lin, S. Kim, Y.-F. Chang, J. C. Lee, *Nanoscale* **2018**, 10, 15608.
- [206] J. Lee, C. Du, K. Sun, E. Kioupakis, W. D. Lu, *ACS Nano* **2016**, 10, 3571.
- [207] C. J. Wan, Y. H. Liu, P. Feng, W. Wang, L. Q. Zhu, Z. P. Liu, Y. Shi, Q. Wan, *Adv. Mater.* **2016**, 28, 5878.
- [208] M. T. Sharbati, Y. Du, J. Torres, N. D. Ardolino, M. Yun, F. Xiong, *Adv. Mater.* **2018**, 30, 1802353.
- [209] S. Lee, J. Sohn, Z. Jiang, H.-Y. Chen, H.-S. Philip Wong, *Nat. Commun.* **2015**, 6, 8407.
- [210] H. Tian, Q. Guo, Y. Xie, H. Zhao, C. Li, J. J. Cha, F. Xia, H. Wang, *Adv. Mater.* **2016**, 28, 4991.
- [211] H. Zhao, Z. Dong, H. Tian, D. DiMarzi, M. G. Han, L. Zhang, X. Yan, F. Liu, L. Shen, S. J. Han, S. Cronin, W. Wu, J. Tice, J. Guo, H. Wang, *Adv. Mater.* **2017**, 29, 1703232.
- [212] C. Pan, Y. Ji, N. Xiao, F. Hui, K. Tang, Y. Guo, X. Xie, F. M. Puglisi, L. Larcher, E. Miranda, L. Jiang, Y. Shi, I. Valov, P. C. McIntyre, R. Waser, M. Lanza, *Adv. Funct. Mater.* **2017**, 27, 1604811.
- [213] M. Suri, O. Bichler, Q. Hubert, L. Perniola, V. Sousa, C. Jahan, D. Guillaume, C. Gamrat, B. DeSalvo, *Solid-State Electron.* **2013**, 79, 227.
- [214] S. Ambrogio, P. Narayanan, H. Tsai, R. M. Shelby, I. Boybat, C. di Nolfo, S. Sidler, M. Giordano, M. Bodini, N. C. P. Farinha, B. Killeen, C. Cheng, Y. Jaoudi, G. W. Burr, *Nature* **2018**, 558, 60.
- [215] G. W. Burr, R. M. Shelby, S. Sidler, C. di Nolfo, J. Jang, I. Boybat, R. S. Shenoy, P. Narayanan, K. Virwani, E. U. Giacometti, B. N. Kurdi, H. Hwang, *IEEE Trans. Electron Devices* **2015**, 62, 3498.
- [216] I. Boybat, M. Le Gallo, S. R. Nandakumar, T. Moraitis, T. Parnell, T. Tuma, B. Rajendran, Y. Leblebici, A. Sebastian, E. Eleftheriou, *Nat. Commun.* **2018**, 9, 2514.
- [217] T. Tuma, A. Pantazi, M. Le Gallo, A. Sebastian, E. Eleftheriou, *Nat. Nanotechnol.* **2016**, 11, 693.
- [218] D. Wang, Y. Dai, J. Xu, L. Chen, Q. Sun, P. Zhou, P. Wang, S. Ding, D. W. Zhang, *IEEE Electron Device Lett.* **2016**, 37, 878.
- [219] L. Zhou, J. Y. Mao, Y. Ren, J. Q. Yang, S. R. Zhang, Y. Zhou, Q. Liao, Y. J. Zeng, H. Shan, Z. Xu, J. Fu, Y. Wang, X. Chen, Z. Lv, S. T. Han, V. A. L. Roy, *Small* **2018**, 14, 1800288.
- [220] J. Shi, S. D. Ha, Y. Zhou, F. Schoofs, S. Ramanathan, *Nat. Commun.* **2013**, 4, 2676.
- [221] T. Shi, R. Yang, X. Guo, *Solid State Ionics* **2016**, 296, 114.
- [222] H. Nili, S. Walia, A. E. Kandjani, R. Ramanathan, P. Gutruf, T. Ahmed, S. Balendhran, V. Bansal, D. B. Strukov, O. Kavehei, M. Bhaskaran, S. Sriram, *Adv. Funct. Mater.* **2015**, 25, 3172.

- [223] M. Moors, K. K. Adepalli, Q. Lu, A. Wedig, C. Bäumer, K. Skaja, B. Arndt, H. L. Tuller, R. Dittmann, R. Waser, B. Yildiz, I. Valov, *ACS Nano* **2016**, *10*, 1481.
- [224] S. Saighi, C. G. Mayr, T. Serrano-Gotarredona, H. Schmidt, G. Lecerf, J. Tomas, J. Grollier, S. Boyn, A. F. Vincent, D. Querlioz, S. La Barbera, F. Alibart, D. Vuillaume, O. Bichler, C. Gamrat, B. Linares-Barranco, *Front. Neurosci.* **2015**, *9*, 51.
- [225] C. Mayr, P. Staerke, J. Partzsch, R. Schueffny, L. Cederstroem, Y. Shuai, N. Du, H. Schmidt, *Adv. Neural Inf. Process. Syst.* **2012**, *3*, 1700.
- [226] Y. Lee, T. W. Lee, *Acc. Chem. Res.* **2019**, *52*, 964.
- [227] B. Yang, Y. Lu, D. Jiang, Z. Li, Y. Zeng, S. Zhang, Y. Ye, Z. Liu, Q. Ou, Y. Wang, S. Dai, Y. Yi, J. Huang, *Adv. Mater.* **2020**, *32*, 2001227.
- [228] M. P. Klinger, A. Fischer, F. Kaschura, J. Widmer, B. Kheradmand-Boroujeni, F. Ellinger, K. Leo, *Sci. Rep.* **2017**, *7*, 44713.
- [229] J. Lenz, F. delGiudice, F. R. Geisenhof, F. Winterer, R. T. Weitz, *Nat. Nanotechnol.* **2019**, *14*, 579.
- [230] S. Goswami, A. J. Matula, S. P. Rath, S. Hedström, S. Saha, M. Annamalai, D. Sengupta, A. Patra, S. Ghosh, H. Jani, S. Sarkar, M. R. Motapothula, C. A. Nijhuis, J. Martin, S. Goswami, V. S. Batista, T. Venkatesan, *Nat. Mater.* **2017**, *16*, 1216.
- [231] G. Liu, C. Wang, W. Zhang, L. Pan, C. Zhang, X. Yang, F. Fan, Y. Chen, R. W. Li, *Adv. Electron. Mater.* **2016**, *2*, 1500298.
- [232] S. D. Pyle, R. Zand, S. Sheikhaal, R. F. Demara, *IEEE J. Explor. Solid-State Comput. Devices Circuits* **2019**, *5*, 43.
- [233] V. Quang Diep, B. Sutton, B. Behin-Aein, S. Datta, *Appl. Phys. Lett.* **2014**, *104*, 222405.
- [234] M. Sharad, C. Augustine, G. Panagopoulos, K. Roy, *IEEE Trans. Nanotechnol.* **2012**, *11*, 843.
- [235] M. Sharad, C. Augustine, K. Roy, in *2012 Int. Electron Devices Meeting*, IEEE, Piscataway, NJ, USA **2012**, <https://doi.org/10.1109/IEDM.2012.6479026>.
- [236] D. I. Suh, J. P. Kil, Y. Choi, G. Y. Bae, W. Park, *IEEE Trans. Magn.* **2015**, *51*, 4401304.
- [237] A. Sengupta, K. Roy, *Phys. Rev. Appl.* **2016**, *5*, 019903.
- [238] S. Zhang, S. Luo, N. Xu, Q. Zou, M. Song, J. Yun, Q. Luo, Z. Guo, R. Li, W. Tian, X. Li, H. Zhou, H. Chen, Y. Zhang, X. Yang, W. Jiang, K. Shen, J. Hong, Z. Yuan, L. Xi, K. Xia, S. Salahuddin, B. Dieny, L. You, *Adv. Electron. Mater.* **2019**, *5*, 1800782.
- [239] P. Krzysteczko, J. Münchenberger, M. Schäfers, G. Reiss, A. Thomas, *Adv. Mater.* **2012**, *24*, 762.
- [240] Y. Cao, A. Rushforth, Y. Sheng, H. Zheng, K. Wang, *Adv. Funct. Mater.* **2019**, *29*, 1808104.
- [241] A. Sengupta, P. Panda, P. Wijesinghe, Y. Kim, K. Roy, *Sci. Rep.* **2016**, *6*, 30039.
- [242] N. Hassan, X. Hu, L. Jiang-Wei, W. H. Brigner, O. G. Akinola, F. Garcia-Sanchez, M. Pasquale, C. H. Bennett, J. A. C. Incorvia, J. S. Friedman, *J. Appl. Phys.* **2018**, *124*, 152127.
- [243] A. Agrawal, K. Roy, *IEEE Trans. Magn.* **2019**, *55*, 1.
- [244] W. H. Brigner, N. Hassan, L. Jiang-Wei, X. Hu, D. Saha, C. H. Bennett, M. J. Marinella, J. A. C. Incorvia, F. Garcia-Sanchez, J. S. Friedman, *IEEE Trans. Electron Devices* **2019**, *66*, 4970.
- [245] Y. Zhang, J. Li, N. Ma, Z. Meng, G. Sui, *Composites, Part B* **2019**, *177*, 107432.
- [246] S. Li, W. Kang, Y. Huang, X. Zhang, Y. Zhou, W. Zhao, *Nanotechnology* **2017**, *28*, 31LT01.
- [247] S. Luo, N. Xu, Z. Guo, Y. Zhang, J. Hong, L. You, *IEEE Electron Device Lett.* **2019**, *40*, 635.
- [248] M. L. Schneider, C. A. Donnelly, S. E. Russek, B. Baek, M. R. Pufall, P. F. Hopkins, P. D. Dresselhaus, S. P. Benz, W. H. Rippard, *Sci. Adv.* **2018**, *4*, e1701329.
- [249] R. Mishra, D. Kumar, H. Yang, *Phys. Rev. Appl.* **2019**, *11*, 54065.
- [250] S. Seo, S. H. Jo, S. Kim, J. Shim, S. Oh, J. H. Kim, K. Heo, J. W. Choi, C. Choi, S. Oh, D. Kuzum, H. S. P. Wong, J. H. Park, *Nat. Commun.* **2018**, *9*, 5106.
- [251] S. Wang, C. Chen, Z. Yu, Y. He, X. Chen, Q. Wan, Y. Shi, D. W. Zhang, H. Zhou, X. Wang, P. Zhou, *Adv. Mater.* **2019**, *31*, 1806227.
- [252] D.-C. Hu, R. Yang, L. Jiang, X. Guo, *ACS Appl. Mater. Interfaces* **2018**, *10*, 6463.
- [253] B. Gholipour, P. Bastock, C. Craig, K. Khan, D. Hewak, C. Soci, *Adv. Opt. Mater.* **2015**, *3*, 635.
- [254] S. Gao, G. Liu, H. Yang, C. Hu, Q. Chen, G. Gong, W. Xue, X. Yi, J. Shang, R.-W. Li, *ACS Nano* **2019**, *13*, 2634.
- [255] M. Kumar, S. Abbas, J. Kim, *ACS Appl. Mater. Interfaces* **2018**, *10*, 34370.
- [256] F. Zhou, Z. Zhou, J. Chen, T. H. Choy, J. Wang, N. Zhang, Z. Lin, S. Yu, J. Kang, H. S. P. Wong, Y. Chai, *Nat. Nanotechnol.* **2019**, *14*, 776.
- [257] D. Xiang, T. Liu, J. Xu, J. Y. Tan, Z. Hu, B. Lei, Y. Zheng, J. Wu, A. H. C. Neto, L. Liu, W. Chen, *Nat. Commun.* **2018**, *9*, 2966.
- [258] S. Dai, Y. Zhao, Y. Wang, J. Zhang, L. Fang, S. Jin, Y. Shao, J. Huang, *Adv. Funct. Mater.* **2019**, *29*, 1903700.
- [259] M. Hu, Y. Chen, J. J. Yang, Y. Wang, H. H. Li, *IEEE Trans. Comput. Des. Integr. Circuits Syst.* **2016**, *36*, 1353.
- [260] J. Bill, R. Legenstein, *Front. Neurosci.* **2014**, *8*, 412.
- [261] W. Ma, L. Chen, C. Du, W. D. Lu, *Appl. Phys. Lett.* **2015**, *107*, 193101.
- [262] T. Werner, E. Vianello, O. Bichler, D. Garbin, D. Cattaert, B. Yvert, B. De Salvo, L. Perniola, *Front. Neurosci.* **2016**, *10*, 474.
- [263] M. A. Zidan, Y. Jeong, W. D. Lu, *IEEE Trans. Nanotechnol.* **2017**, *16*, 721.
- [264] X. Zhang, Y. Zhuo, Q. Luo, Z. Wu, R. Midya, Z. Wang, W. Song, R. Wang, N. K. Upadhyay, Y. Fang, F. Kiani, M. Rao, Y. Yang, Q. Xia, Q. Liu, M. Liu, J. J. Yang, *Nat. Commun.* **2020**, *11*, 51.
- [265] P. Yao, H. Wu, B. Gao, J. Tang, Q. Zhang, W. Zhang, J. J. Yang, H. Qian, *Nature* **2020**, *577*, 641.
- [266] D. S. Jeong, *J. Appl. Phys.* **2018**, *124*, 152002.
- [267] X. Zhang, A. Huang, Q. Hu, Z. Xiao, P. K. Chu, *Phys. Status Solidi* **2018**, *215*, 1700875.
- [268] Q. Xia, J. J. Yang, *Nat. Mater.* **2019**, *18*, 309.
- [269] F. M. Bayat, M. Prezioso, B. Chakrabarti, H. Nili, I. Kataeva, D. Strukov, *Nat. Commun.* **2018**, *9*, 2331.
- [270] S. Choi, S. H. Tan, Z. Li, Y. Kim, C. Choi, P. Y. Chen, H. Yeon, S. Yu, J. Kim, *Nat. Mater.* **2018**, *17*, 335.
- [271] Z. Wang, S. Joshi, S. Savel, W. Song, R. Midya, Y. Li, M. Rao, P. Yan, S. Asapu, Y. Zhuo, H. Jiang, P. Lin, C. Li, J. H. Yoon, N. K. Upadhyay, J. Zhang, M. Hu, J. P. Strachan, M. Barnell, Q. Wu, H. Wu, R. S. Williams, Q. Xia, J. J. Yang, *Nat. Electron.* **2018**, *1*, 137.
- [272] C. Li, D. Belkin, Y. Li, P. Yan, M. Hu, N. Ge, H. Jiang, E. Montgomery, P. Lin, Z. Wang, W. Song, J. P. Strachan, M. Barnell, Q. Wu, R. S. Williams, J. J. Yang, Q. Xia, *Nat. Commun.* **2018**, *9*, 2385.
- [273] S. Chen, M. R. Mahmoodi, Y. Shi, C. Mahata, B. Yuan, X. Liang, C. Wen, F. Hui, D. Akinwande, D. B. Strukov, M. Lanza, *Nat. Electron.* **2020**, *3*, 638.
- [274] X. Li, J. Tang, Q. Zhang, B. Gao, J. J. Yang, S. Song, W. Wu, W. Zhang, P. Yao, N. Deng, L. Deng, Y. Xie, H. Qian, H. Wu, *Nat. Nanotechnol.* **2020**, *15*, 776.
- [275] M. A. Zidan, J. P. Strachan, W. D. Lu, *Nat. Electron.* **2018**, *1*, 22.
- [276] H. Wang, Q. Zhao, Z. Ni, Q. Li, H. Liu, Y. Yang, L. Wang, Y. Ran, Y. Guo, W. Hu, Y. Liu, *Adv. Mater.* **2018**, *30*, 1803961.
- [277] H. E. Lee, J. H. Park, T. J. Kim, D. Im, J. H. Shin, D. H. Kim, B. Mohammad, I. S. Kang, K. J. Lee, *Adv. Funct. Mater.* **2018**, *28*, 1801690.
- [278] C. Wan, P. Cai, M. Wang, Y. Qian, W. Huang, X. Chen, *Adv. Mater.* **2020**, *32*, 1902434.
- [279] G. Zhang, D. Guo, F. Wu, J. Ma, *Neurocomputing* **2020**, *379*, 296.
- [280] L. Yin, R. Zheng, W. Ke, Q. He, Y. Zhang, J. Li, B. Wang, Z. Mi, Y. Long, M. J. Rasch, *Nat. Commun.* **2018**, *9*, 4890.
- [281] D. Kuzum, S. Yu, H. S. Philip Wong, *Nanotechnology* **2013**, *24*, 382001.
- [282] S. Raoux, *Annu. Rev. Mater. Res.* **2009**, *39*, 25.
- [283] A. R. Mellnik, J. S. Lee, A. Richardella, J. L. Grab, P. J. Mintun, M. H. Fischer, A. Vaezi, A. Manchon, E. A. Kim, N. Samarth, D. C. Ralph, *Nature* **2014**, *511*, 449.
- [284] T. P. L. Pedersen, J. Kalb, W. K. Njoroge, D. Wamwangi, M. Wuttig, F. Spaepen, *Appl. Phys. Lett.* **2001**, *79*, 3597.

- [285] B. Chen, Y. Lu, B. Gao, Y. H. Fu, F. F. Zhang, P. Huang, Y. S. Chen, L. F. Liu, X. Y. Liu, J. F. Kang, Y. Y. Wang, Z. Fang, H. Y. Yu, X. Li, X. P. Wang, N. Singh, G. Q. Lo, D. L. Kwong, in *2011 IEEE Int. Electron Devices Meeting*, IEEE, Piscataway, NJ, USA **2011**, <https://doi.org/10.1109/IEDM.2011.6131539>.
- [286] K. Moon, M. Kwak, J. Park, D. Lee, H. Hwang, *IEEE Electron Device Lett.* **2017**, *38*, 1023.
- [287] E. J. Fuller, F. El Gabaly, F. Léonard, S. Agarwal, S. J. Plimpton, R. B. Jacobs-Gedrim, C. D. James, M. J. Marinella, A. A. Talin, *Adv. Mater.* **2017**, *29*, 1604310.
- [288] S. Chandrasekaran, F. M. Simanjuntak, R. Saminathan, D. Panda, T.-Y. Tseng, *Nanotechnology* **2019**, *30*, 445205.
- [289] W. Wu, H. Wu, B. Gao, P. Yao, X. Zhang, X. Peng, S. Yu, H. Qian, in *2018 IEEE Symp. on VLSI Technology*, IEEE, Piscataway, NJ, USA **2018**, pp. 103–104, <https://doi.org/10.1109/VLSIT.2018.8510690>.
- [290] P.-Y. Chen, B. Lin, I.-T. Wang, T.-H. Hou, J. Ye, S. Vrudhula, J. Seo, Y. Cao, S. Yu, in *2015 IEEE/ACM Int. Conf. on Computer-Aided Design (ICCAD)*, IEEE, Piscataway, NJ, USA **2015**, pp. 194–199, <https://doi.org/10.1109/ICCAD.2015.7372570>.
- [291] A. V. Khvalkovskiy, D. Apalkov, S. Watts, R. Chepulsckii, R. S. Beach, A. Ong, X. Tang, A. Driskill-Smith, W. H. Butler, P. B. Visscher, D. Lottis, E. Chen, V. Nikitin, M. Krounbi, *J. Phys. D: Appl. Phys.* **2013**, *46*, 074001.
- [292] G. Chen, S. Ivanov, S. Urazhdin, *Appl. Phys. Lett.* **2020**, *117*, 103501.
- [293] T. Shibata, T. Shinohara, T. Ashida, M. Ohta, K. Ito, S. Yamada, Y. Terasaki, T. Sasaki, *Appl. Phys. Express* **2020**, *13*, 043004.
- [294] J. Hawkins, S. Ahmad, *Front. Neural Circuits* **2016**, *10*, 23.
- [295] L. Piroux, J. M. George, J. F. Despres, C. Leroy, E. Ferain, R. Legras, K. Ounadjela, A. Fert, *Appl. Phys. Lett.* **1994**, *65*, 2484.
- [296] D. Zhang, L. Zeng, K. Cao, M. Wang, S. Peng, Y. Zhang, Y. Zhang, J. O. Klein, Y. Wang, W. Zhao, *IEEE Trans. Biomed. Circuits Syst.* **2016**, *10*, 828.
- [297] A. H. All, X. Zeng, D. B. L. Teh, Z. Yi, A. Prasad, T. Ishizuka, N. Thakor, Y. Hiromu, X. Liu, *Adv. Mater.* **2019**, *31*, 1803474.



Hongyu Bian earned her B.E. degree (2009) in physics from Northeast Normal University, P. R. China. She received her Ph.D. degree in condensed matter physics (2017) at Northeast Normal University, P. R. China. She is currently a postdoctoral fellow in the group of Prof. Xiaogang Liu at the National University of Singapore. Her current research interests focus on the design and synthesis of lanthanide-doped materials for emerging applications.



Yi Yiing Goh graduated from the National University of Singapore with a B.Sc. in chemistry in 2018. He is currently pursuing his Ph.D. in NUS Graduate School of Integrative Sciences and Engineering under the supervision of Prof. Liu Xiaogang. His current research interest lies in the rational design of lanthanide-doped nanomaterials as biomarkers to probe biological processes in vivo, especially in deep-lying tissues.



Yuxia Liu was born in Hubei province, China. She received her Bachelor's degree in biomedical engineering from Xi'an Jiaotong University in 2014, and she earned her Ph.D. degree in biomedical engineering from Tsinghua University in 2020. She is currently a postdoctoral fellow in the group of Prof. Xiaogang Liu at the National University of Singapore. Her current research interests focus on exploiting nanotechnology tools to modulate membrane-related biological processes, understand neuronal behaviors, and develop therapeutic strategies.



Haifeng Ling received his Ph.D. degree from Nanjing University of Posts and Telecommunications in 2017. He then worked at The Hong Kong Polytechnic University as a postdoctoral fellow during 2017–2019. He joined the Institute of Advanced Materials (IAM) at NUPT in 2019. His research interests focus on organic flexible electronics, nonvolatile memory, and artificial synapses.



Linghai Xie received his B.S. degree in applied chemistry from Northeast Normal University, China. He received his M.S. degree in industrial catalysis from Shantou University and completed his Ph.D. at Fudan University. He then joined Nanjing University of Post and Telecommunications in 2006. Currently, he is a full professor and director of the Center for Molecular Systems & Organic Devices at the Institute of Advanced Materials. His research encompasses organic nanochemistry, wide-bandgap materials, film computing & organic intelligence, and artificial intelligence & robotic chemistry.



Xiaogang Liu received his B.E. degree in chemical engineering from Beijing Technology and Business University, China. He received his M.S. degree in chemistry from East Carolina University and completed his Ph.D. at Northwestern University. He then carried out postdoctoral work at MIT for two years before joining the National University of Singapore in 2006. Currently, he sits as an associate editor for Nanoscale. His research encompasses areas including nano-structured catalysis, optical nanomaterials, optogenetic neuromodulation, and X-ray imaging.